Intermolecular Coulombic decay following ionization of noble gas dimers and of biochemically relevant hydrogen bonded systems

Ph. D. Thesis

Spas Stoychev

2011

INAUGURAL DISSERTATION

zur

Erlangung der Doktorwürde

der

Naturwissenschaftlich-Mathematischen

Gesamtfakultät

der

Ruprecht–Karls–Universität

Heidelberg

vorgelegt von

Chemie Master Spas Dimitrov Stoychev

aus Sofia (Bulgarien)

Tag der mündlichen Prüfung: 11. 07. 2011

Intermolecular Coulombic decay following ionization of noble gas dimers and of biochemically relevant hydrogen bonded systems

Gutachter: Prof. Dr. Lorenz S. Cederbaum
Prof. Dr. Jochen Schirmer

To My Muse

Acknowledgements

First and foremost, I would like to express my utmost gratitude to my supervisor Prof. Lorenz Cederbaum whose guidance of my research activities, as well as kind-hearted attitude to me I will never forget. Our discussions have always been an inspiration that has stimulated my work, as far as Prof. Cederbaum has always pointed to me the right direction in which my, sometimes, flustered thoughts should go.

I would like to thank Dr. Alexander Kuleff for the enormous amount of time and efforts invested in my education during the last six years and his positive thinking that has constantly encouraged me. I owe my deepest gratitude to Prof. Jochen Schirmer for introducing me to the theoretical methods which I have extensively used throughout my investigations. His Friday lectures were a real treasure in the "realm" of quantum chemistry. I would also like to thank Prof. Horst Köppel and Prof. Markus Pernpointner for my first steps in the group theory, as well as Prof. Philipp Demekhin for the everyday enlightening discussions and for sharing his relentless drive for scientific research. I highly appreciate the exchange of ideas and the help in the preparation of the thesis from my friends and colleagues Dr. Kirill Gokhberg, Sören Kopelke, Dr. Anthony Dutoi, Dr. Victor Bezchastnov, and Dr. Oriol Vendrell. I thank Dr. Michael Brill and the other members of the "Doppelkopf community" for the warm welcome into the group extracurricular activities and Annette Braun for being always willing to help me with the everyday formalities accompanying my stay at the university. I am grateful to Dr. Yasen Velkov, Dr. Imke Müller, Dr. Nikolai Kryzhevoi, Dr. Evgeniy Gromov, Dr. Vitali Averbukh, Ying-Chih Chiang, and Dr. Premysl Kolorenč for showing me the computational techniques required to survive in the small zoo of computer programs available in our group. I thank Dr. Frank Otto, Bernd Schubert, and Victor Vysotskiy who had voluntarily taken the heavy burden of administrating our computer system and have spared "cheetah" and "jane" in the years I needed them.

And now I want to thank those without whom I would have never come to Heidelberg University: my master thesis supervisor Prof. Alia Tadjer, as well as to Prof. Anela Ivanova who showed me the way in the quantum chemical world at Sofia University and insisted on me to give a lecture every time I was flying home that turned out to be of great help while writing my thesis; my high school chemistry teacher Mrs. Stoeva for perfecting my basics of chemistry; the financial support of the Deutscher Akademischer Austausch Dienst.

I thank my father, mother, and sister (all of them chemists) who have surely induced my curiosity in the field of science and have always supported me in pursuing a carrier as a researcher. Last but not least, I want to thank my beautiful wife and daughter for the inspiration that I find in them every day. I am also grateful to my wife for the patience and understanding towards my passion for scientific work she has always had.

Abstract

The present work contains the results of our theoretical studies of Intermolecular Coulombic decay (ICD) following ionization of noble gas dimers and of biochemically relevant hydrogen bonded systems. We have investigated the ICD following Auger decay of the weakly bound Ne_2, Ar_2, and NeAr. It was shown that despite their seeming simplicity the noble gas clusters are lavish in interesting physical phenomena and provide the opportunity for studying various kinds of ultrafast and fast interatomic processes, such as: direct ICD, exchange ICD, electron transfer mediated decay (ETMD), processes of photon emission, and relaxation by coupling to the nuclear motion. Our results have largely expanded the qualitative and quantitative understanding of this type of cascade decay processes. A better interpretation of experimentally observed phenomena was achieved with our numerical data which were also used to computed ICD electron spectra within the framework of the time-dependent theory of wave packet propagation.

The ICD following inner-valence ionization was studied for the hydrogen bonded $H_2O\cdots H_2O$, $H_2O\cdots HCHO$, $H_2O\cdots H_2CNH$, $H_2O\cdots NH_3$, $NH_3\cdots H_2O$, $H_2O\cdots H_2S$, and $H_2S\cdots H_2O$ (p-donor $\cdots$ p-acceptor). This set of small hydrogen bonded systems contains seven types of hydrogen bonding which are typical for biochemistry and thus its investigation provides insight into the processes that can take place in living tissues. In particular, an estimate of the ICD in biosystems interacting with water (their usual medium) is made. This decay mode is expected to be a source of low-energy electrons proven to be of extreme genotoxic nature. The study of $H_2O\cdots H_2O$ also includes the first quantitative description of the ICD of doubly ionized states created via Auger decay.

For the purpose of our study we have used high-precision *ab initio* methods in optimizing the geometries and computing the ground state energies, as well as the single-, double-, and triple-ionization spectra of the studied species. The energy range of the emitted ICD electrons, as well as the kinetic energy of the dissociating ions produced by ICD is also reported. Potential energy curves of the different electronic states involved in the investigated processes were computed and analyzed where it was needed.

Kurzfassung

Diese Arbeit umfasst theoretische Untersuchungen des Interatomic Coulombic Decay (ICD) nach Ionisierung in Edelgasdimeren und bio-chemisch relevanten wasserstoffgebundenen Systemen. Darüber hinaus wird der ICD nach Auger Zerfällen in Ne_2, Ar_2, und NeAr studiert. In früheren Arbeiten wurde gezeigt, dass - trotz ihrer Einfachheit - Edelgasdimere reich sind an interessanten physikalischen Phänomenen wie z.B. direct ICD, exchange ICD, electron transfer mediated decay (ETMD), Photonemission und Relaxation aufgrund von Kernbewegung. Die Ergebnisse dieser Arbeit haben das Vertändnis des ICD nach Auger Zerfällen vertieft und Interpretationen experimenteller Ergebnisse ermöglicht.

Der ICD wird in dieser Arbeit in den folgenden wasserstoffgebundenen Systemen untersucht: $H_2O\cdots H_2O$, $H_2O\cdots HCHO$, $H_2O\cdots H_2CNH$, $H_2O\cdots NH_3$, $NH_3\cdots H_2O$, $H_2O\cdots H_2S$, and $H_2S\cdots H_2O$ (p-donor $\cdots$ p-acceptor). Diese Auswahl an Systemen umfasst sieben Typen der Wasserstoffbindung die für die Biochemie relevant sind und somit Einsichten in Prozesse, die in lebenden Organismen stattfinden können bzw. könnten, ermöglichen. Desweiteren wurden qualitative Studien über den ICD in solchen Systemen in Wasser durchgeführt. Die Ergebnisse deuten darauf hin, dass der ICD in solchen Systemen langsame Elektronen freisetzt, welche die menschlichen Gene beschädigen können. Die Studie über $H_2O\cdots H_2O$ enthält die erste Beschreibung von ICD doppelionisierter Zustände, die nach Auger Zerfällen enstehen können.

Die Untersuchungen, die die Berechungen von optimalen Geometrien, Grundzustandsenergien, Ionisierungs-, Doppelionisierungs- und Dreifachionisierungsenergien umfassen, wurde mit hochpräzisen *ab initio* Methoden durchgeführt. Die kinetischen Energiebereiche der resultierenden ICD-Elektronen und Molekül-Fragmente werden ebenfalls angegeben. Wo es nötig war, wurden Potentialflächen bestimmt und analysiert.

Contents

Chapter 1

Introduction

Creating a core vacancy in atoms or molecules produces a cation with energy above its double or even multiple ionization threshold [1–3]. As a result, an electron from a higher energy level may fall into the vacancy and the energy thus released can be transferred to another electron, which is then ejected from the system. This fundamental process was discovered in the early 1920's by Lise Meitner and independently by Pierre Auger and is known as Auger decay [4]. The secondary emitted, or Auger, electron has a specific energy depending on the system being ionized, thus giving rise to a characteristic spectrum. An important feature of the Auger decay is that it is typically an intraatomic process, only weakly influenced by the environment of the emitting atom [5]. The Auger decay is also ultrafast taking place in the femto- and even attosecond time domain [6].

In contrast, creating an inner-valence vacancy in isolated atoms or molecules will usually not lead to a relaxation process accompanied by secondary electron emission, since the energy of the cation will be below the double ionization threshold. Such states will relax by photon emission or in the case of molecules also by coupling to the nuclear motion. Here, however, the medium plays a critical role. If the ionized system is embedded in an environment or has neighbors like in a cluster, another relaxation mechanism can prevail. After inner-valence ionization of a particular subunit of the cluster (atom or molecule), the inner-valence vacancy may be refilled by an outer-valence electron of the same subunit and the energy gained in this process can be transferred to another cluster subunit, which uses it to emit an outer-valence electron. The final state is thus characterized by two outer-valence vacancies, each on a different counterparts. This electronic decay process was predicted theoretically in the late 1990's and named *interatomic* (*intermolecular*) *Coulombic decay* (ICD) [7]. Most importantly, the ICD has been anticipated to be extremely efficient in comparison with the processes of photon emission and relax-

ation via nuclear dynamics with which it competes. Indeed, the predicted ICD lifetimes typically vary in the interval of 1 to 100 femtoseconds [8, 9], while the just mentioned relaxation modes are typically orders of magnitude slower. Therefore, if an inner-valence ionized atom or molecule cannot autoionize, but has weakly bound neighbors it is a prime candidate for ICD.

The ICD phenomenon has been intensively studied, both theoretically and experimentally. In the pioneering work on ICD [7] the existence of the novel relaxation mechanism of singly and doubly ionized electronic states was illustrated in hydrogen fluoride and water trimers, respectively. It was stressed that the ICD is of a very general nature and should apply to a large variety of weakly bound systems. The study of ICD of hydrogen fluoride and water containing clusters was later extended [8, 10, 11]. It was shown that standard quantum chemistry procedures augmented by complex absorbing potentials can be used to compute the lifetimes of the inner-valence vacancy states of the HF cluster into account. The numerical results that were obtained suggested that the ICD would happen on a femtosecond timescale [8]. An explicit example of ICD in mixed hydrogen bonded cluster $HF(H_2O)_2$ followed [10]. There, the new decay process was investigated along with a quantitative measure and characterization of the hole localization pattern of the cationic states. The dense line bundles in the inner-valence region of the ionization spectrum of the system which mimic the continuous decay distributions were analyzed in detail. The resulting intermolecular character of the lowest in energy doubly ionized states confirmed the proposed intermolecular Coulombic mechanism for the electronic decay which leads to dicationic states with two vacancies located on neighboring monomer units. The ionization of an atom X in an endohedral fullerene complex $X@C_n$ can also lead to ICD [12]. This interatomic processes occur due to the correlation between the atomic and the fullerene electrons and do not take place in the free species X. Considering $Ne@C_{60}$ as an example, the rates of the ICD were calculated and shown that the process is ultrafast with a lifetime of less than 2 fs. Moreover, it was suggested that interatomic decay in an endohedral fullerene does not necessarily lead to the destruction of the complex. It was also reported that tertiary electron emission may occur via a combined cascade of electron transfer mediated decay and ICD. The study of microsolvation of F^- in water by means of computed ionization and double ionization spectra of $(H_2O)_{1-3}F^-$ indicated that ICD can be initiated by single ionization of systems containing anions [13], as well.

The ICD initiated by inner-valence ionization in small water clusters was investigated in Ref. [11]. For this purpose, the valence ionization and double ionization spectra of the

water molecule, of the water dimer, and the cyclic water clusters $(H_2O)_3$ and $(H_2O)_4$ were calculated. This study paid a particular attention to the analysis of the development of the spectra with increasing cluster size and gave a crude estimate for the kinetic energy spectrum of the ICD electrons.

Very recently, the first successful experimental measuremets of ICD in water clusters took place [14,15]. The new for the transition from gas to liquid phase of water phenomena was reported in Ref. [14]. There, the ultrafast transfer of energy across the hydrogen bridge in $(H_2O)_2$ was directly observed. It was shown that ICD is faster than the proton transfer in small water clusters and leads to dissociation of the water dimer into two H_2O^+ ions. The observed ICD channel appeared to be a source of electrons which are known to damage biological matter. In a related experimental work [15], the production of low-energy electrons in amorphous medium-sized water clusters, which simulate water molecules in an aqueous environment was studied. There, a unrecognized extra source of low-energy electrons produced by a non-local autoionization process was assigned to ICD. The unequivocal signature of this process was observed in coincidence measurements of low-energy electrons and photoelectrons generated from inner-valence states with vacuum-ultraviolet light. These results also suggested that ICD could have implications for our understanding of ionization damage in living tissues.

In a series of publications, the ICD in noble gas clusters was thoroughly investigated making use of the relative simplicity of the interatomic compared to the intermolecular ICD. A theoretical description within the framework of Wigner-Weisskopf theory was developed and an approximate but illuminative expression for the electronic decay width of an inner-valence hole state was derived. It was applied to investigate the effect of cluster size on the ICD process [9]. A pronounced size effect was also found in the concrete example of neon clusters. The decay lifetime decreases in a monotonic fashion from hundred femtoseconds in Ne_2 down to less than ten femtoseconds in Ne_{13}. The electron dynamics of the ICD in real time and space were investigated using a wave packet propagation method that allows to trace fully ab-initio the electron dynamics of the process. The evolution of the electronic cloud during the ICD in NeAr following Ne2s ionization was computed and analyzed [16]. The investigated process that takes place on a femtosecond time scale, turned out to have a surprisingly strong response already in the attosecond regime. Thus, it was proposed to visualize the ICD by means of advanced laser pump-probe techniques that could be used to study the fundamental question of the energy transfer from one atom to another.

The discovery of the ICD revealed a whole zoo of related phenomena. Here we will

briefly sketch only those which are directly discussed in the present study and refer the interested reader to Refs. [17–19] for a detailed discussion of other interatomic decay mechanisms. A few years ago it was predicted theoretically that creating a single vacancy in the inner-valence shell of an atom embedded in an environment is not the only possibility to initiate ICD. Excited Auger final states that cannot decay non-radiatively in an isolated system can relax, when the system is embedded in an environment (e.g., in a cluster), by electronic emission from a neighboring subunit. In other words, ICD can be the final step of a cascade decay initiated by core ionization [20]. In a series of experimental works, the occurrence of ICD from Auger final states in different rare gas clusters was subsequently demonstrated [21–24].

Important for the present work is the interatomic (intermolecular) decay process where an electron transfer between the system subunits appears as a mediator of the decay. This has been termed *electron-transfer mediated decay* (ETMD) [25]. In this process, an inner-valence vacancy is refilled by an outer-valence electron of a neighboring atom or molecule, from which in addition a secondary (ETMD) electron is emitted. Therefore, in contrast to ICD, after ETMD the system ends up with two vacancies on a site different from the one initially ionized. The theoretical study of ETMD was reported in Ref. [25], where heteroclusters built up of monomer units of largely different energies were investigated. The lifetime of the inner-valence Ne($2s^{-1}$)Ar vacancy had been estimated and partitioned according to the contributions of the two decay channels based on a perturbation-theoretical description of the decay process. As a result, the lifetime of the inner-valence resonance state was estimated to be of the order of 10s of fs, the specific value strongly depending on the internuclear separation of the monomers. The ICD process was shown to be by far the dominant decay channel at distances corresponding to the equilibrium geometry of the dimer. With decreasing internuclear separation the ratio of the ETMD and ICD decay widths quickly increases over several orders of magnitude. It was also shown that even in loosely bound van der Waals clusters the orbital overlap is a crucial factor for the interatomic electronic decay [26]. Even at the equilibrium bond length of a cluster, the overlap effect can bring about a significant enhancement of the decay rate. Inner-valence ionization of species containing positive and negative microsolvated ions is another type of systems in which ICD and ETMD are feasible. As proposed in Ref. [17], the ionization in the energy range between 35 eV and 75 eV of aqueous Li^+ microsolvation clusters may initialize several different electronic decay processes. The Li^+ ionization probes the efficiency of the ETMD processes. It was estimated that the ETMD lifetimes are in the range of 20 to 100 fs for clusters with one to more water monomers.

Another possibility for a process of electron transfer is the one in which an outer-valence electron from a site neighboring the one initially ionized fills the inner-valence vacancy and an outer-valence electron from the initially ionized subsystem is emitted. In the following we will address to this process as 'exchange' ICD (eICD). Since both ETMD and eICD involve electron transfer, they are typically orders of magnitude slower than the discussed above ICD characterized by a transfer of a virtual photon and usually referred as 'direct' ICD (dICD). Only at short separations between the system subunits they are expected to give a non-negligible contribution to the total decay rate, due to the enhanced overlap between the wavefunctions, but still much smaller than the direct ICD rate [25,26]. However, there are situations where the direct ICD channel is forbidden and ETMD and/or exchange ICD appear as the only possible electronic decay modes [27].

Van der Waals clusters were also the first species in which the ICD was experimentally observed. The electron spectra of photoexcited Ne clusters showed a signal at low kinetic energies that is neither present in the Ne monomer nor at photon energies below the inner-valence $2s$ threshold [28]. These findings were the fist strong evidence for the existence of interatomic Coulombic decays. The experimental observation of ICD in $2s$ ionized neon dimers was reported in Ref. [29]. There, the process is unambiguously identified by detecting the energy of two Ne^+ fragments and the ICD electron in coincidence, yielding a clean, background free experimental spectral distribution of the ICD electrons. A quantitative determination of $2s$ vacancy lifetimes in surface and bulk atoms of free Ne clusters has also been made [30]. While for free atoms the 2s inner-valence hole has a ps lifetime, it reduces to 6 fs for cluster bulk atoms and 30 fs for cluster surface atoms. This lifetime estimate was obtained from the high-resolution photoelectron spectra of Ne clusters. The shortening of the lifetime is attributed to the coordination dependent ICD, which is extremely sensitive to internuclear distances.

The decay of excited states via resonant ICD accompanied by a release of Ne ion and a neutral excited Ne fragment had also been observed [31].

The generality of the ICD and the related to it phenomena urges for the increase of the scope of system where it is investigated. Thus, a better understanding of this fascinating phenomenon will be achieved and new important features of well known species will be discovered. Experimental results that review the presence of ICD following an Auger decay in noble gas clusters [21–24] also inquire better understanding and interpretation. The possibility for that type of cascade decay was proposed in Ref. [20] considering the energies of specific states of Ne and Ar only. The broader picture which includes all of the relevant decay modes had to be portrayed in a greater detail. The thourough

study of these processes is essential for the correct perseption of the phenomena that are initiated by a core ionization of atoms and molecules. Being very fast, the ICD is of great importance for multiply ionized and excited species that are always present after an Auger decay for example. The sheer number of electronic states created by the relaxation of the core ionized systems is another obstacle that has to be challenged in the theoretical, as well experimental studies of cascade decay processes. Therefore, the first attempts for the qualitative evaluation of the ultra fast interatomic cascade decay is being made in Chapter 3 of the present work with the help of potential energy curves (PECs). This approach allows us to establish the global picture by identifying the decay mechanisms that can take place, as well as the interatomic separations at which a specific relaxation mode is operative. That happens to be of great importance when studying processes following an Auger decay that populates a multitude of different electronic states in a broad energy range. The obtained in this fashion results are also successfully used to guide the experimental efforts and make the analysis of the measured data feasible. The PECs can also be used in a more advances calculations that include the nuclear dynamics of the systems.

The proposed ICD of singly and doubly ionized states of the water dimer in Refs. [11] and [7], respectively also needed further investigation. Although, being the most important first step, these theoretical works contain only a qualitative description of the studied phenomena. Thus, in analogy to the just mentioned noble gas systems a study accounting for the distance dependent effects in $(H_2O)_2$ was essential. Therefore, our efforts (see Chapter 3) are put in the better understanding of the ICD following inner-valence, as well as core ionization of the water dimer. For this purpose we will be using PECs and estimates of the energy of the emitted e^-_{ICD}. Considering the penetrating ability of the very short waves needed to make the initial for this process states, our results are of great relevance for large scale species present in living organisms that are usually submerged in water. Another aspect of our work is the study of ICD following the inner-valence ionization of small hydrogen bonded systems that represent relevant for the biochemistry hydrogen bonds. A particular attention to the hydrogen bonded $H_2O\cdots HCHO$, $H_2O\cdots H_2CNH$, $H_2O\cdots NH_3$, $NH_3\cdots H_2O$, $H_2O\cdots H_2S$, and $H_2S\cdots H_2O$ (p-donor $\cdots$ p-acceptor) is being paid in Chapter 4. These small system contain the most common types of hydrogen bonding in biochemistry. Since their electronic spectra can be used to qualitatively predict the abundance of ICD in large macromolecules we will try to determine which intermolecular electronic decay modes are allowed and estimate the energy range and the shape of the spectra of the emitted electrons. Thus, the real impact

of the ICD and the related phenomena on the living matter will be depicted for the first time.

Chapter 2

Theory and computational methods

2.1 Theoretical backgrounds

The qualitative description of the ICD and the related to it phenomena can be successfully accomplished with the help of the energies of the initial and final states that are involved in them. Since the investigated in the present work species are singly, doubly, and triply ionized we shall mainly be using their ionization potentials. Proper methods for computation of these quantities were one of the first to be developed in quantum chemistry due to the fundamental nature of the problem. Additional effort in finding a better description of the ionization processes and ionized systems with the help of new theoretical approaches, as well as computational techniques is still being put. In what follows we shall make a short overview of the Hartree-Fock (HF) method, which gives them most simplified description of the electronic wave functions of the interesting for us species and happens to be the basis of all of the other methods which we have used. We shall consider the Koopmans theorem and its consequences on the computation of the ionization potentials and the ΔSCF method which allows to obtain a meaningful result in the study of ionized systems. Special attention will be paid to the Green's functions based methods which contain information about the ionization potentials of an N-electron system and allow their direct calculation. These methods also provide a systematic framework for improving the IPs obtained within the HF approximation by means of schemes like the *algebraic diagrammatic construction (ADC)*, for example. A detailed list of the computational techniques implemented in our study is given in the next section.

2.1.1 The Hartree-Fock approximation

The Hartree-Fock (HF) approximation, which is equivalent to the molecular orbital approximation, is central to chemistry [32]. This is a single determinant quantum theory in which a set of spin orbitals χ_a form:

$$|\Phi_0\rangle = |\chi_1\chi_2\cdots\chi_a\chi_b\cdots\chi_N\rangle \tag{2.1}$$

that is the best possible approximation of the ground state of the N-electron system in the field of M point charges described by the electronic Hamiltonian H:

$$H = -\sum_i^N \frac{1}{2}\nabla_i^2 - \sum_i^N\sum_A^M \frac{Z_A}{r_{iA}} + \sum_i^N\sum_{j>i}^N \frac{1}{r_{ij}} \tag{2.2}$$

and the solution of the Schrödinger equation involving the electronic Hamiltonian is an electronic wave function Φ_0 that describes the motion of the electrons and explicitly depends on the electronic coordinates, but depends parametrically on the nuclear ones:

$$H\Phi_0 = E\Phi_0. \tag{2.3}$$

The use of separate electronic Hamiltonian is a good approximation in which one consides that the electrons in a molecule are moving in the field of fixed nuclei and is also known as the Born-Oppenheimer approximation.

According to the variational principle, the optimal spin orbitals are those which minimize the energy:

$$E_0 = \langle\Phi_0|H|\Phi_0\rangle = \sum_a \langle a|h|a\rangle + \frac{1}{2}\sum_{ab}\langle ab||ab\rangle. \tag{2.4}$$

Thus, by systematically varying the spin orbital χ_a constraining them only to remain orthonormal,

$$\langle\chi_a|\chi_b\rangle = \delta_{ab} \tag{2.5}$$

the minimum energy can be determined. The equation for the "best" spin orbitals is also known as the Hartree-Fock integro-differential equation:

$$h(1)\chi_1 + \sum_{b\neq a}\left[\int dx_2|\chi_b(2)|^2 r_{12}^{-1}\right]\chi_a(1) - \sum_{b\neq a}\left[\int dx_2\chi_b(2)^*\chi_a(2)r_{12}^{-1}\right]\chi_b(1) = \varepsilon_a\chi_a(1) \tag{2.6}$$

where

$$h(1) = -\frac{1}{2}\nabla_1^2 - \sum_A \frac{Z_A}{r_{1A}} \tag{2.7}$$

comprises the kinetic and the potential energy for the attraction to the nuclei, of a single electron chosen to be electron (1), while the energy of the spin orbital $\chi_a(1)$ equals ε_a.

The two terms involving sums over b are those that in the single determinant HF theory represent electron-electron interactions. Without these terms,

$$h(1)\chi_a(1) = \varepsilon_a\chi_a(1) \tag{2.8}$$

would simply be the one-electron Schrödinger equation for the spin orbital states of a single electron in the field of the nuclei. The first of the two-electron terms is the *Coulomb* term, while the second one is the *exchange* term.

The Coulomb term has a simple interpretation. In an exact theory, the Coulomb interaction is represented by the two-electron operator r_{12}^{-1}. In the HF approximation (see Eq. 2.6), electron one in χ_a experiences a one-electron Coulomb potential:

$$v_a^{coul} = \sum_{b\neq a} \int dx_2 |\chi_b(2)|^2 r_{12}^{-1}. \tag{2.9}$$

Thus, if electron 2 occupies χ_b, the *two-electron potential* r_{12}^{-1} felt by electron 1 and associated with the instantaneous position of electron 2 is replaced by a *one-electron potential* obtained by averaging the interaction r_{12}^{-1} of electron 1 and electron 2, over all space and spin coordinates x_2 of electron 2, weighted by the probability $dx_2|\chi_b(2)|^2$ that electron 2 occupies the volume element dx_2 at x_2. By summing over all $b \neq a$, one obtains the total average potential acting on the electron in χ_a, arising form the $N-1$ electrons in the other spin orbitals. Associated with this interpretation it is convenient to define a *Coulomb operator*:

$$J_b(1) = \int dx_2 |\chi_b(2)|^2 r_{12}^{-1} \tag{2.10}$$

which represents the average local potential at x_1 arising from an electron in χ_b. Thus, operating on the orbital χ_a, the Coulomb operator will have the effect:

$$J_b(1)\chi_a(1) = \left[\int dx_2 \chi_b(2)^* r_{12}^{-1} \chi_b(2)\right] \chi_a(1) \tag{2.11}$$

Analogously an *exchange operator* $K_b(1)$ can be defined by its effect when operating on $\chi_a(1)$ as:

$$K_b(1)\chi_a(1) = \left[\int dx_2 \chi_b(2)^* r_{12}^{-1} \chi_a(2)\right] \chi_b(1) \tag{2.12}$$

The exchange term arises from the antisymmetric nature of the single determinant. It does not have a simple classical interpretation like the Coulomb one.

The HF equation can be written as the eigenvalue equation using the two operators:

$$\left[h(1) + \sum_{b \neq a} J_b(1) - \sum_{b \neq a} K_b(1)\right] \chi_a(1) = \varepsilon_a \chi_a(1) \tag{2.13}$$

Operating with $K_b(1)$ on $\chi_a(1)$ involves an "exchange" of electron 1 and electron 2 to the right of r_{12}^{-1}. Therefore, unlike the *local* Coulomb operator, the exchange operator is said to be *non-local* operator, since there does not exist a simple potential $K_b(x_1)$ uniquely defined at a local point in space x_1. The result operating with $K_b(x_1)$ on $\chi_a(x_1)$ depends on the value of $\chi_a(x_1)$ throughout all space, not just at x_1. One could not, for example draw a contour plots of the exchange potential as one can for the Coulomb potential. For an electron in χ_a the expectation values of the Coulomb and exchange potentials J_b and K_b are just the Coulomb and exchange integrals:

$$\langle \chi_a(1) | J_b(1) | \chi_a(1) \rangle = \int dx_1 dx_2 \chi_a^*(1) \chi_a(1) r_{12}^{-1} \chi_b^*(2) \chi_b(2) = [aa|bb] = \langle ab|ab \rangle \tag{2.14}$$

$$\langle \chi_a(1) | K_b(1) | \chi_a(1) \rangle = \int dx_1 dx_2 \chi_a^*(1) \chi_b(1) r_{12}^{-1} \chi_b^*(2) \chi_a(2) = [ab|ab] = \langle aa|bb \rangle. \tag{2.15}$$

The operator in the square brackets of the HF equation (Eq. 2.13), as written above, appears to be different for every spin orbit χ_a on which it operates due to the restricted summation over $b \neq a$. However, inspecting the terms for $J_b(1)$ and $K_b(1)$ it is obvious that:

$$[J_a(1) - K_a(1)] \chi_a(1) = 0. \tag{2.16}$$

It is, thus, possible to add this term to Eq. 2.13, eliminate the restriction on the summation, and define the *Fock operator* f by:

$$f(1) = h(1) + \sum_b J_b(1) - K_b(1), \tag{2.17}$$

so that the HF equations become:

$$f|\chi_a\rangle = \varepsilon_a \chi_a. \tag{2.18}$$

This is the usual form of the HF equation. The Fock operator $f(1)$ is the sum of a *core-Hamiltonian operator* $h(1)$ and an effective one-electron potential called the *Hartree-Fock potential* $V^{HF}(1)$:

$$V^{HF}(1) = \sum_b J_b(1) - K_b(1), \tag{2.19}$$

thus we could also write:

$$f(1) = h(1) + V^{HF}(1). \tag{2.20}$$

The HF equation (Eq. 2.18) is an eigenvalue equation with the spin orbitals as eigenfunctions and the energy of the spin orbitals as eigenvalues. The exact solution to this integro-differential equation corresponds to the "exact" HF spin orbitals. In practice it is only possible to solve this equation exactly (i.e., as integro-differential equation) for atoms. Instead, one normally introduces a set of basis functions for expansion of the spin orbitals and solves a set of matrix equations. Only as the basis set approaches completeness, i.e. as one approaches the HF limit, will the spin orbitals approach the exact HF spin-orbitals.

It is convenient to write the HF potential in the general and more compact form:

$$V_{pq}^{HF} = \sum_i V_{pi[qi]}. \tag{2.21}$$

Here, the definition $V_{pq[rs]} := V_{pqrs} - V_{pqsr}$ is being used, while $V_{pq[rs]}$ consists of a direct and an exchange interaction term, depending on the electron-electron Coulomb element:

$$V_{pq[rs]} = \int dx_1 dx_2 \chi_p^*(1)\chi_r(1) r_{12}^{-1} \chi_q^*(2)\chi_s(2) = \langle pq|rs\rangle. \tag{2.22}$$

Thus, the general element of the Fock operator in analogy with (Eq. 2.20) has the form:

$$\langle \chi_p | f | \chi_q \rangle = \langle p|h|q\rangle + V_{pq}^{HF}. \tag{2.23}$$

2.1.2 The Koopmans' theorem and the ΔSCF method

The Koopmans' theorem states that if a system is described by a N-electron HF determinant $|^N\Phi_0\rangle$ with occupied and virtual orbital energies ε_a and ε_r, then the ionization potential to produce $(N-1)$-electron single determinant $|^{N-1}\Phi_a\rangle$ with identical spin orbitals, obtained by removing an electron form spin orbital χ_a, and the electron affinity to produce an $(N+1)$-electron single determinant $|^{N+1}\Phi_r\rangle$ with identical spin orbitals, obtained by adding an electron to spin orbital χ_r, are just $-\varepsilon_a$ and $-\varepsilon_r$, respectively.

Thus, it is possible to calculate approximate ionization potentials (IPs) and electron affinities (EAs) based on the HF result for the neutral system. However, this "frozen orbital" approximation assumes that the spin orbitals in the $(N \pm 1)$-electron states, i.e. the positive and negative ions of the $|^N\Phi_0\rangle$ neutral species are identical with those of the N-electron state. This approximation neglects relaxation of the spin orbitals in the

$(N \pm 1)$-electron state or that the spin orbitals of $|^N\Phi_0\rangle$ are not the optimum ones for $|^{N-1}\Phi_a\rangle$ or $|^{N+1}\Phi^r\rangle$.

Optimizing the spin orbitals of the $(N \pm 1)$-electron single determinants by performing a separate HF calculation on these states would lower the energies. Therefore, the neglect of relaxation in Koopmans' theorem calculations tends to produce too positive ionization potentials and too negative electron affinities. The use of a single determinant wave function also leads to the neglect of the *correlation effects*, which one could include going beyond the HF approximation. In particular, correction energies are larger for systems with higher number of electrons. In fact, the energy difference $\Delta E^{SCF} = E^{SCF}_{ground} - E^{SCF}_{ion}$ computed using post HF methods that treat the correlation effect and improve to a good extent the computational result of the system in its ground state E^{SCF}_{ground} and the electronic state of interest E^{SCF}_{ion}, gives a meaningful and accurate result for IPs and EAs. This type of calculations are also called ΔSCF *method* and are widely used. However, they allow the computation of only one electronic state at a time and do not directly contain information about the intensity of the referred spectral line. In order to obtain the entire ionization spectrum of a system, one needs to invest in a significant computational effort and solve the problem of obtaining the energies of the higher lying electronic sates. These limitations of standard ab-initio approaches can be overcome with the direct computation of the needed quantities with the help of Green's functions based methods.

2.1.3 The Green's function

The methods of Green's functions and propagators has been widely used to study quantum properties of several- and many-particle systems. These functions have attracted much attention in numerous fields of research, because of their close proximity to experimental observations and their amenableness to elegant theories and approximation schemes [33]. The Green's function is defined as the N-electron ground state average of a time-ordered product of an annihilation and a creation operators, a_k and $a^\dagger_l$,

$$G_{kl}(t,t') = -i\langle^N\Psi_0|T\{a_k(t)a^\dagger_l(t')\}|^N\Psi_0\rangle \tag{2.24}$$

where T is the Wick time-ordering operator. The creation and annihilation operators obey the usual relations

$$a_k(t) = e^{iHt}c_k e^{-iHt}, c_k = a_k(0) \tag{2.25}$$

$$[c_k, c^\dagger_l]_+ = \delta_{kl}, [c_k, c_l]_+ = [c^\dagger_k, c^\dagger_l]_+ = 0. \tag{2.26}$$

Here, the full Hamiltonian (H) is time independent, therefore and G_{kl} depends only on $t - t'$ and its Fourier transform is easily performed,

$$\begin{aligned} G_{kl}(\omega) &= \int_{-\infty}^{\infty} G_{kl}(t-t')e^{i\omega(t-t')}d(t-t') \\ &= \sum_s \frac{\langle {}^N\Psi_0|c_l^\dagger|{}^{N-1}\Psi_s\rangle\langle {}^{N-1}\Psi_s|c_k|{}^N\Psi_0\rangle}{\omega + IP_s - i\eta} + \sum_r \frac{\langle {}^N\Psi_0|c_k|{}^{N+1}\Psi_r\rangle\langle {}^{N+1}\Psi_r|c_l^\dagger|{}^N\Psi_0\rangle}{\omega + EA_r - i\eta} \end{aligned} \tag{2.27}$$

where $IP_s = E_s^{N-1} - E_0^N$ and $EA_r = E_0^N - E_r^{N+1}$.

The first sum of $\underline{\underline{G}}(\omega)$ has poles at the IPs of the system, with $|{}^N\Psi_0\rangle$ being its ground state and is referred as *advanced* component of the Green's function. The second sum has poles at the EAs of the same system and is referred as *retarded* component of the Green's function.

Multiple ionized states can be analogously described by Green's functions which are also called propagators. The particle-particle (pp) propagator corresponds to the doubly ionized system [34] that can be created by Auger decay and has the form:

$$\begin{aligned} G^{pp}_{rs,r's'}(\omega) = &- \sum_{m\in(N-2)} \frac{\langle {}^N\Psi_0|c_r^\dagger c_s^\dagger|{}^{N-2}\Psi_m\rangle\langle {}^{N-2}\Psi_m|c_{r'}c_{s'}|{}^N\Psi_0\rangle}{\omega + E_m^{N-2} - E_0^N - i\eta} \\ &+ \sum_{m\in(N+2)} \frac{\langle {}^N\Psi_0|c_r c_s|{}^{N+2}\Psi_m\rangle\langle {}^{N+2}\Psi_m|c_{r'}^\dagger c_{s'}^\dagger|{}^N\Psi_0\rangle}{\omega + E_0^N - E_m^{N+2} + i\eta} \end{aligned} \tag{2.28}$$

while the the three-particle (ppp) propagator corresponds to the triply ionized system [35], typical for the final states of ICD following Auger, is written as:

$$\begin{aligned} G^{ppp}_{prs,p'r's'}(\omega) = &- \sum_{m\in(N-3)} \frac{\langle {}^N\Psi_0|c_p^\dagger c_r^\dagger c_s^\dagger|{}^{N-3}\Psi_m\rangle\langle {}^{N-3}\Psi_m|c_{p'}c_{r'}c_{s'}|{}^N\Psi_0\rangle}{\omega + E_m^{N-3} - E_0^N - i\eta} \\ &+ \sum_{m\in(N+3)} \frac{\langle {}^N\Psi_0|c_p c_r c_s|{}^{N+3}\Psi_m\rangle\langle {}^{N+3}\Psi_m|c_{p'}^\dagger c_{r'}^\dagger c_{s'}^\dagger|{}^N\Psi_0\rangle}{\omega + E_0^N - E_m^{N+3} + i\eta}. \end{aligned} \tag{2.29}$$

For the sake of clarity we will consider in the following only the one-body Green's function, noting that the extention of the formalism to the pp and ppp propagators is cumbersome, but straightforward. For further readings see Ref. [36] and the references therein. The Hamiltonian of the one-body Green's function, can be decomposed into two parts,

$$H = H_0 + H_I, \tag{2.30}$$

the so-called free Green's function G^0 can be defined in the time domain in complete

analogy to G, but with the unperturbed one-particle (not including the two particle Coulomb and exchange interactions, as well as any correlation effects) Hamiltonian H_0:

$$G^0_{kl}(t) = -i\langle {}^N\Psi_0|T\{a_k(t)a^\dagger_l(t')\}|{}^N\Psi_0\rangle \tag{2.31}$$

where $a_k(t) = e^{iH_0t}c_ke^{-iH_0t}$ and $|{}^N\Psi_0\rangle$ is the ground-state.

For the special case where we choose H_0 to be the HF operator, the Fourier transform of the free Green's function ($\underline{\underline{G}}^0(\omega)$) has poles at the values of ω that are equal to the orbital energies of a system with one electron, just like those predicted by the Koopmans' theorem. Thus, $G^0(t)$ can be regarded as an approximation to the *exact* $\underline{\underline{G}}(\omega)$ which has poles at the exact energy differences between the the N and $(N \pm 1)$-particle systems. If we could obtain $\underline{\underline{G}}(\omega)$, or at least a better approximation to it than $\underline{\underline{G}}^0(\omega)$, then we would be able to improve upon Koopmans' theorem IP's and EA's while retaining the one-particle picture associated with the HF theory. This can be accomplished by introducing an energy dependent effective potential as proposed F. Dyson and given the name *self-energy*. Moreover, it was shown that the exact $\underline{\underline{G}}(\omega)$ obeys the integral equation (called the *Dyson equation*):

$$\underline{\underline{G}}(\omega) = \underline{\underline{G}}^0(\omega) + \underline{\underline{G}}^0(\omega)\underline{\underline{\Sigma}}(\omega)\underline{\underline{G}}(\omega) \tag{2.32}$$

where $\underline{\underline{\Sigma(\omega)}}$ is the representation of the exact self energy in the basis of HF spin orbitals. Finally, various terms in the perturbation expansion of $\underline{\underline{\Sigma(\omega)}}$ can be generated,

$$\underline{\underline{\Sigma}}(\omega) = \underline{\underline{\Sigma}}^{(2)}(\omega) + \underline{\underline{\Sigma}}^{(3)}(\omega) + ... \tag{2.33}$$

The terms written above can be determined considering that the self-energy consists of a static part $\Sigma(\infty)$ not depending on ω and a dynamic part depending on ω:

$$\underline{\underline{\Sigma}}(\omega) = \underline{\underline{\Sigma}}(\infty) + \underline{\underline{M}}(\omega), \tag{2.34}$$

where the static part can be evaluated once the dynamic self-energy ($\underline{\underline{M}}(\omega)$) is known.

2.1.4 The ADC(n) scheme

An elegant way to derive approximations with increasing accuracy of the ω-dependent self-energy part $\underline{\underline{M}}(\omega)$ is the so-called *algebraic diagrammatic construction* (ADC). The general concept and the usefullness of the ADC scheme for the one-particle Green's function can be found in Ref. [37]. As the Green's function $\underline{\underline{G}}(\omega)$, can be partitioned into a part related to the electron affinity $\underline{\underline{M}}(\omega)^I$ and a part related to the ionization of the system $\underline{\underline{M}}(\omega)^{II}$, we shall discuss only $\underline{\underline{M}}(\omega)^I$ corresponding to the $(N+1)$-particle system noting that the treatment of the quantity $\underline{\underline{M}}(\omega)^{II}$ corresponding $(N-1)$ is essentially identical. The exact self-energy parts of $\underline{\underline{M}}(\omega)^I$ and $\underline{\underline{M}}(\omega)^{II}$ can be obtained by the simple algebraic equation

$$M_{pq}(\omega) = \underline{U}_p^\dagger(\omega\underline{\underline{1}} - \underline{\underline{K}} - \underline{\underline{C}})^{-1}\underline{U}_q \tag{2.35}$$

where $\underline{U}_p$ is a constant (ω-independent) vector of "modified coupling amplitudes" for the orbital p and $\underline{\underline{K}}$ and $\underline{\underline{C}}$ are constat Hermitian matrices, the latter being referred to as the "modified interaction matrix". These quantities are defined with respect to the space of physical $(N \pm 1)$-particle excitations excluding the 1h and 1p configurations. More specifically, the configuration space for the $(N+1)$-particle case $\underline{\underline{M}}^I(\omega)$ is given by the 2p-1h, 3p-2h,..., excitations, while the $(N-1)$-particle case $\underline{\underline{M}}^{II}(\omega)$ requires the 2h-1p, 3h-2p,..., excitations.

Both the (column) vectors $\underline{U}_p$ and the matrix $\underline{\underline{C}}$ are subject to perturbation expansions

$$\underline{U}_p = \underline{U}_p^{(1)} + \underline{U}_p^{(2)} + ..., \tag{2.36}$$

$$\underline{\underline{C}} = \underline{\underline{C}}^{(1)} + \underline{\underline{C}}^{(2)} + ..., \tag{2.37}$$

each series starting with a first-order contribution $\underline{U}_p^{(1)}$ and $\underline{\underline{C}}^{(1)}$, respectively. The matrix $\underline{\underline{K}}$ is given as a diagonal matrix of zeroth-order (HF) excitation energies, e.g.,

$$\begin{aligned} K_{jkl,jkl} &= -\epsilon_j + \epsilon_a + \epsilon_b, n_j\overline{n}_a\overline{n}_b = 1 \\ K_{ijklm,ijklm} &= -\epsilon_i - \epsilon_j + \epsilon_a + \epsilon_b + \epsilon_c, n_in_j\overline{n}_a\overline{n}_b\overline{n}_c = 1 \end{aligned} \tag{2.38}$$

for the 2p-1h and the 3h-2p space, respectively. n and $\overline{n}$ are the occupation number of occupied and virtual orbitals, respectively. Here and in the following the subscripts $a, b, c, ...$, refer to virtual orbitals, $i, j, k, ...$, refer to occupied orbitals, while the subscripts, $p, q, r, ...$, are general indices.

A set of symmetric approximations $\underline{\underline{M}}(\omega; n)$ with $n = 2, 3, ...$, for $\underline{\underline{M}}(\omega)^{I,II}$ is obtained

by requiring that the form

$$M_{pq}(\omega;n) = \underline{U}_p(n)^\dagger(\omega\underline{\underline{1}} - \underline{\underline{K}} - \underline{\underline{C}}(n))^{-1}\underline{U}_q(n) \tag{2.39}$$

is exact up to nth order of perturbation theory, that is,

$$M_{pq}(\omega;n) = \sum_{\nu=2}^{n} M_{pq}^{(\nu)}(\omega) + O(n+1), \tag{2.40}$$

here $M_{pq}^{(\nu)}(\omega)$ denotes the νth-order contribution for the self-energy parts $\underline{\underline{M}}(\omega)^{I,II}$ in the diagrammatic perturbation expansion.

A characteristic (and not always desirable) feature of the Dyson methods is that in these approaches, the $(N \pm 1)$-particle parts of the one-particle Green's function are interconnected. Thus, the resulting equations are defined with respect to configurational spaces comprising both $(N+1)$- and $(N-1)$-electron configurations. In order to overcome this problem an alternative ADC approximation for the electron propagator which does not employ the Dyson equation had been proposed [38]. The essential conceptual and computational simplification in this non-Dyson ADC(n) scheme is achieved by the fact that the $(N+1)$- and $(N-1)$-electron problems are no longer coupled and can be treated separately. The corresponding equations are thus defined with respect of much smaller configurational spaces. The non-Dyson ADC(n) scheme scales as k^5 with respect to the number of orbitals k and can be considered as e useful alternative to the Dyson ADC(n) in large-scale calculations.

The non-Dyson ADC approximation schemes are obtained by applying the ADC procedure separately to each of the $(N-1)$- and $(N+1)$-particle parts of the electron propagator $\underline{\underline{G}}(\omega)$:

$$\underline{\underline{G}}(\omega) = \underline{\underline{G}}^-(\omega) + \underline{\underline{G}}^+(\omega). \tag{2.41}$$

The non-diagonal representation of the Green's function that represents the ionization potentials can be written in a general form:

$$\underline{\underline{G}}^-(\omega) = \underline{f}^\dagger(\omega\underline{\underline{1}} - \underline{\underline{K}} - \underline{\underline{C}})^{-1}\underline{f} \tag{2.42}$$

where the "effective interaction" matrix $\underline{\underline{K}}+\underline{\underline{C}}$ is defined as a representation of the shifted Hamiltonian $H - E_0$ in terms of the so-called "intermediate states" $|^{N-1}\tilde{\Psi}_J\rangle$,

$$(\underline{\underline{K}} + \underline{\underline{C}})_{IJ} = -\langle^{N-1}\tilde{\Psi}_I|H - E_0|^{N-1}\tilde{\Psi}_J\rangle \tag{2.43}$$

and the "effective transition moments" are defined as

$$f_{I,q} = \langle {}^{N-1}\tilde{\Psi}_I | c_q | {}^N\Psi_0 \rangle. \tag{2.44}$$

In Eqs. 2.42-2.44 $|{}^N\Psi_0\rangle$ and E_0 denote the exact N-electron ground state and the ground-state energy, respectively, and H is the Hamiltonian of the system; $c_q(c_q^\dagger)$ denote destruction (creation) operators associated with HF orbital q. The intermediate states $|{}^{N-1}\tilde{\Psi}_J\rangle$ are generated by a specific orthonormalization procedure form the correlated $(N-1)$-electron states

$$|{}^{\#}\Psi_J\rangle = \tilde{C}_J | {}^N\Psi_0 \rangle \tag{2.45}$$

where $\tilde{C}_J$ denote the class of excitation operators generating one-hole, two-hole-one-particle,..., configurations:

$$\{\tilde{C}_J\} = \{c_k, c_a^\dagger c_k c_l, c_a^\dagger c_b^\dagger c_k c_l c_m, ...; a < b < ...; k < l < m < ...\}. \tag{2.46}$$

The intermediate states $|{}^{N-1}\tilde{\Psi}_J\rangle$ are related to the exact states $|{}^{N-1}\Psi_m\rangle$ via a transformation:

$$|{}^{N-1}\Psi_m\rangle = \sum_J Y_{Jm} |{}^{N-1}\tilde{\Psi}_J\rangle. \tag{2.47}$$

The part of the Green's function that describes the ionization potentials takes on a diagonal form in the basis of exact states $|{}^{N-1}\Psi_m\rangle$. This is the so-called spectral representation, in which the physical content of the electron propagator is explicit:

$$\underline{\underline{G}}^-(\omega) = \underline{x}_p^\dagger (\omega \underline{\underline{1}} - \underline{\underline{\Omega}})^{-1} \underline{x}_q. \tag{2.48}$$

Here $\underline{\underline{\Omega}}$ denotes the diagonal matrix of (negative) vertical ionization energies,

$$\Omega_{mm} = -(E_m^{(N-1)} - E_0^N) \tag{2.49}$$

and the vectors $\underline{x}$ denote spectroscopic amplitudes, related to spectral intensities,

$$x_{mq} = \langle {}^{N-1}\Psi_m | c_q | {}^N\Psi_0 \rangle. \tag{2.50}$$

The simplest form of the (relative) photoelectron spectral intensity P_m can be evaluated according to

$$P_m = \sum_q |x_{m,q}|^2. \tag{2.51}$$

The transformation of $\underline{\underline{G}}^{-}(\omega)$ from the ADC representation, Eq. 2.42, to the spectral representation Eq. 2.48 is equivalent to the solution of the Hermitian eigenvalue problem for the matrix $\underline{\underline{K}} + \underline{\underline{C}}$,

$$(\underline{\underline{K}} + \underline{\underline{C}})\underline{\underline{Y}} = \underline{\underline{Y}}\ \underline{\underline{\Omega}}, \underline{\underline{Y}}^{\dagger}\underline{\underline{Y}} = \underline{\underline{1}} \tag{2.52}$$

where $\underline{\underline{Y}}$ denotes the matrix of eigenvectors. The eigenvectors of $\underline{\underline{Y}}$ form the transformation matrix relating the intermediate states and the exact states,

$$Y_{Jm} = \langle {}^{N-1}\Psi_J | c_q | {}^{N-1}\Psi_m \rangle. \tag{2.53}$$

The spectroscopic amplitudes $\underline{x}$ can be obtained from the effective transition moments $\underline{f}$ according to

$$\underline{x}_p = \underline{\underline{Y}}^{\dagger}\underline{f}_p \tag{2.54}$$

The non-Dyson approximation scheme for $\underline{\underline{G}}^{-}(\omega)$ Eq. 2.42 are obtained by truncating the expansion manifold Eq. 2.47 and by employing consistent perturbation expansions for the matrix elements of the effective interaction and transition moments:

$$\underline{\underline{K}} + \underline{\underline{C}} = \underline{\underline{K}}^{(0)} + \underline{\underline{C}}^{(1)} + \underline{\underline{C}}^{(2)} + ..., \tag{2.55}$$

$$\underline{f} = \underline{f}^{(0)} + \underline{f}^{(1)} + \underline{f}^{(2)} + ... \tag{2.56}$$

The explicit expressions for the elements of $\underline{\underline{K}} + \underline{\underline{C}}$ and $\underline{f}$ can be delivered using the Rayleigh-Schrödinger perturbation theory for $|{}^{N}\Psi_0\rangle$ and E_0, or by the ADC procedure operating with the diagrammatic perturbation expansion for $\underline{\underline{G}}^{-}(\omega)$.

The explicit configuration space of the ADC(n) secular equations for $n = 2$ and 3 is spanned by the one-hole and two-hole-one-particle excitations and grows in each even order n by one excitation class. This property of the explicit ADC configuration spaces has been referred to as compactness. Finally, the ADC method is size-consistent (size-extensive) which means that for a system of separate fragments the results do not depend on whether the method is applied to the whole system or to each of the fragments separately.

2.1.5 The ICD rate

At this point an important aspect of ICD has to be addressed. Here, we shall only discuss the process initiated by inner-valence ionization and stress again that the description of electronic states that can be created by an Auger decay, discussed in the introduc-

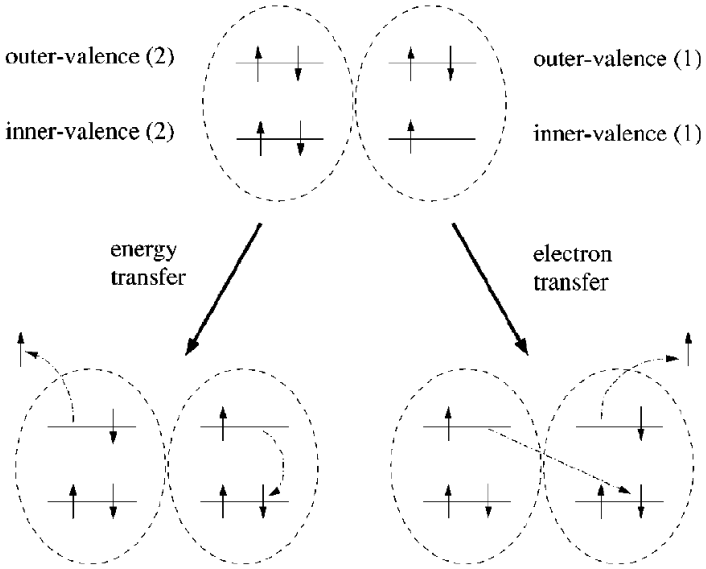

Figure 2.1: Two different physical mechanisms can be identified in the theoretical description of electronic decay processes in weakly bound clusters. The mechanisms are associated with the direct and the exchange term, respectively, of the coupling matrix element $V_{ov_1,ov_2[iv,k]} = V_{ov_1,ov_2,iv,k} - V_{ov_1,ov_2,k,iv}$ in Eq. 17 of Ref. [9] from which the figure is taken. ICD of inner-valence holes is best understood in terms of energy transfer between the involved monomers ($V_{ov_1,ov_2,iv,k}$). Electron transfer ($V_{ov_1,ov_2,k,iv}$) is only of minor importance. Please note that both possible decay mechanisms are purely intermolecular the two dashed ovals symbolize two neighboring monomers. A similar decomposition of direct and exchange terms appears in the description of ICD of doubly ionized states that can be created by an Auger decay. For further details see the text and Refs. [9].

tion, is analogous. An approximate but illuminative expression for the ICD rate can be obtained using the Wigner-Weisskopf method based on time-dependent perturbation theory (see, e.g. [39]). Within this first order theory, the ICD rate is proportional to $|V_{ov_1,ov_2,iv,k} - V_{ov_1,ov_2,k,iv}|^2$, where V_{ijkl} is the two-electron Coulomb matrix element which can be calculated on the HF level. The subscripts ov_1 and ov_2 correspond to the two outer-valence electrons, iv stands for the initial inner-valence vacancy, and k for the continuum electron [9]. Thus, the decay rate is proportional to the modulus square of the difference between the direct and the corresponding exchange Coulomb matrix elements. For the Auger decay rate we have a similar expression where the direct and exchange matrix elements arise from the indistinguishability of the electrons involved in the decay. In the case of ICD, where the participating electrons are located on different subsystems, these two terms describe actually different physical phenomena. If we take ov_1 to label the electron (hole) residing on the same site as iv, the first, or the direct, term describes the

process in which an outer-valence electron from the initially ionized subsystem fills the inner-valence vacancy and an outer-valence electron from the other subsystem is emitted. The second, or the exchange, term describes the process of electron transfer, i.e. where an outer-valence electron from a site neighboring the one initially ionized fills the inner-valence vacancy and an outer-valence electron from the initially ionized subsystem is emitted, see also Fig. 2.1. These two processes are referred as 'direct' and 'exchange' ICD, respectively. A similar decomposition of direct and exchange terms appears in the description of ICD of doubly ionized states.

A more accurate calculation of ICD rates of interatomic and intermolecular nonradiative decay processes occurring due to electronic correlation of resonances can be achieved with the help of the two theoretical approaches which we will now mention. The first of them relies on the introduction of complex absorbing potential into the (N - 1)-electron Hamiltonian - represented using a variety of ab initio techniques, such as, configuration interaction or algebraic diagrammatic construction, as it was shown in Refs. [40] and [41], respectively. Within the second approach, ADC based methods for the description of the boundlike and the continuumlike components of the wave function of the decaying state are implemented and a normalization of the continuum (final state) wave function using the Stieltjes imaging technique is employed [42]. This methodology was also extended to describe the interatomic decay of excited doubly ionized states of clusters in Ref. [43].

2.2 Computational details

In the course of our study, we have used a large variety of computational methods, schemes and approaches. Therefore, a detailed description of these techniques, as well as of some of the notations used in the figures discussed below is given in the current subsection.

2.2.1 Neon dimer

The various decay processes in the neon dimer can be investigated using the potential energy curves (PECs) of the different electronic states involved in them. This amounts to calculating and analyzing the PECs of the ground state of Ne_2, the singly ionized state $Ne^+(1s^{-1})$-Ne, as well as those for the different doubly and triply ionized states, Ne_2^{++} and Ne_2^{3+}. The PEC for the ground state of the weakly bound system Ne_2 was computed via the coupled cluster singles and doubles and perturbative triples (CCSD(T)) method using the d-aug-cc-pV5Z basis [44]; an additional d-aug-cc-pV5Z basis set was put in the middle of the bond and the basis set superposition error was counterpoise corrected. The calculations were carried out with the MOLPRO package [45]. The energies of the relevant cationic, dicationic, and tricationic states were computed within the framework of the Green's function approach using the algebraic diagrammatic construction (ADC) scheme [33, 37], discussed above, as well as in the literature [34, 37, 46–48]. As already mentioned, the ADC(n) implements infinite partial summations of perturbative terms of the appropriate Green's function, which are exact up to the n-th order of perturbation theory. Important features of this approach is its compactness and size-consistency. The core-ionization energies ($Ne^+(1s^{-1})$-Ne) were calculated via the ADC(4) scheme [37, 49] for the one-particle Green's function using the d-aug-cc-pVTZ basis set. The ADC(2) scheme for the particle-particle propagator [34, 50] and the three-particle propagator [35] were used to compute the dicationic and tricationic states, respectively (in both cases the aug-cc-pVQZ basis set was utilized). These energies were then added to those of the ground state of the neutral to obtain the PECs for the singly, doubly and triply ionized Ne_2. In all calculations the spin-orbit effects were neglected.

In order to obtain the correct absolute energy scale, the computed PECs were shifted to match at large internuclear distances the spectroscopic data of the separated atoms. Where it was relevant, the spectroscopic data were averaged over the total angular momentum. Thus, for $Ne^+(1s^{-1})$-Ne the calculated ionization energy at 10.0 Å is set equal to that of $Ne^+(1s^{-1})$ taken from Ref. [51]. The double and triply ionization energies leading to the one-site states (i.e., states where both vacancies are located on the same

Ne atom) calculated at 10.0 Å are set to those for the corresponding atomic states in the NIST database [3]. The PECs for the two-site states of Ne_2^{++}, correlating with two singly ionized Ne atoms, are adjusted by setting their values at 10.0 Å to the sum of the NIST energies for the corresponding Ne^+ states plus the Coulomb repulsion between two elementary charges at that distance. A similar adjustment (accounting for the Coulomb repulsion) is made for the two-site states of Ne_2^{3+}, which correlate with a doubly and a singly ionized Ne atoms. We have to mention that the ADC procedures for various kinds of ionization processes are accurate through a given order of perturbation theory, i.e. one expects different accuracy for singly, doubly, and triply ionized states. However, for the kind of systems discussed here the error depends very weakly on the internuclear distance and can be well eliminated by the just described asymptotic adjustment of the corresponding PECs to the spectroscopic data. The energies of the relevant electronic states of the Ne atomic ions used to calibrate the energy scale, along with the available atomic Auger rates are presented in Table 3.1.

As a result of our calculations, a large number of PECs has been produced. A few remarks about those selected for presentation and the way they are depicted in our figures should be made. The potential energy curves form groups corresponding essentially to specific electronic configurations. Usually, at small internuclear distances the curves within a given group are spread within an energy band, while at large internuclear distances they merge into a single curve. To avoid overburdening the figures, we show only the curves that define the upper and the lower limit of the band for each group. Furthermore, only one line is plotted to represent nearly degenerate curves.

In order to better distinguish the different dicationic PECs in the figures 3.3 to 3.5, the following types and colors of the lines are chosen: green color is used for the PECs of states with two holes in the $2s$ level, orange for states with one hole in the $2s$ level and one hole in the $2p$ level, and blue for states with two holes in the $2p$ level. Solid lines are used to represent singlet states and dashed lines are used for the Ne_2^{++} triplets. Thus, a solid blue line stands for a singlet state with two holes in the $2p$ levels, an orange dashed line for a triplet state with holes in $2s$ and $2p$ levels, and so on. The tricationic states $Ne^{3+}(2p^{-3})$-Ne, $Ne^{++}(2p^{-2})$-$Ne^+(2p^{-1})$, and $Ne^{++}(2p^{-2})$-$Ne^+(2s^{-1})$ are plotted as solid black lines, while those of $Ne^{++}(2s^{-1}2p^{-1})$-$Ne^+(2p^{-1})$ as dashed-dotted black lines.

2.2.2 Argon dimer

To gain insight into the decay processes in the argon dimer we have again studied the different electronic states as a function of interatomic separation. This amounts to calcu-

lating PECs for the ground state of Ar_2, for the singly ionized state $Ar^+(2p^{-1})$-Ar, as well as those for the different doubly and triply ionized states, Ar_2^{++} and Ar_2^{3+}. The PEC of the ground state of the weakly bound system Ar_2 was computed via the CCSD(T) method using the aug-cc-pV6Z basis set [44], the basis set superposition error was counterpoise corrected. The calculations were carried out with the MOLPRO package [45]. The energies of the relevant cationic, dicationic, and tricationic states were determined within the framework of the Green's function approach using the (ADC) scheme. The core-ionization energies ($Ar^+(2p^{-1})$-Ar) were calculated through ADC(4) scheme [37, 49] for the one-particle Green's function using the aug-cc-pVTZ basis set. The ADC(2) scheme for the particle-particle propagator [34, 50] and the three-particle propagator [35] were used to compute the dicationic and tricationic states, respectively (in both cases aug-cc-pVQZ basis sets were utilized). These energies were then added to those of the ground state of the neutral to obtain the PECs for the singly, doubly and triply ionized Ar_2. In all calculations the spin-orbit effects were neglected.

In order to obtain the correct absolute energy scale, the resulting potential curves were shifted to match at large internuclear distances the spectroscopic data of the separated atoms. Where it was relevant, the spectroscopic data were averaged over the total angular momentum. Thus, for $Ar^+(2p^{-1})$-Ar the corresponding calculated ionization energy at 9.0 Å is set equal to that of $Ar^+(2p^{-1})$ taken from Ref. [1]. The double ionization energies for the one-site states calculated at 9.0 Å are set to those for the corresponding atomic states in the NIST database [3]. The PECs for the two-site doubly ionized argon dimer are adjusted by setting their values at 9.0 Å to the sum of the NIST energies for the corresponding Ar^+ states and the Coulomb repulsion between two elementary charges at that distance. A similar adjustment (accounting for the Coulomb repulsion) is made for the two-site states of Ar_2^{3+}.

The electronic states of the Ar atom relevant for the Auger decay and ICD, and their energies which have been used to determine the absolute energy scale of the PECs, are presented in Table 3.4.

A few remarks about the PECs that have been selected for presentation and the way they are depicted in figures 3.10 to 3.12 should be made. As a result of our calculations, a large number of PECs has been produced. These curves form groups corresponding essentially to specific electronic configurations. In order to better distinguish the different dicationic PECs, the following types and colors of the lines are chosen: green color is used for the PECs of states with two holes in the $3s$ level, orange for states with one hole in the $3s$ level and one hole in the $3p$ level (and their satellites), and blue for states with

two holes in the $3p$ level (and their satellites). Solid lines are used to represent bound Ar^{++}-Ar singlet states, dashed lines are used for Ar^{++}-Ar triplets, dashed-dotted lines for the repulsive curves of Ar^{+}-Ar^{+} singlets, and dotted lines for Ar^{+}-Ar^{+} triplets. Thus, a blue dotted line stands for a triplet two-site (unbound) state with two holes in the $3p$ levels, an orange dashed line for a triplet one-site (bound) state with holes in $3s$ and $3p$ levels, and so on. The final tricationic states, Ar^{++}-Ar^{+}, are plotted as solid black lines.

2.2.3 Neon Argon

In the study of the NeAr and its electronic decay we have also used PECs of different electronic states. The ground state of the weakly bound system was computed via the CCSD(T) method, the aug-cc-pV6Z basis set [44] was implemented for the Ar atom and d-aug-cc-pV5Z basis set was used for the Ne atom, as well as a bond function in the middle of the interatomic distance. The basis set superposition error was counterpoise corrected, while calculations were carried out with the MOLPRO package [45]. The energies of the relevant cationic, dicationic, and tricationic states were determined within the framework of the Green's function approach using the (ADC) scheme. The core-ionization energies of $Ne^{+}(2s^{-1})$-Ar were calculated through ADC(4) scheme [37, 49] for the one-particle Green's function using the aug-cc-cVTZ basis set. The ADC(2) scheme for the particle-particle propagator [34, 50] and the three-particle propagator [35] were used to compute the dicationic and tricationic states, respectively (in both cases aug-cc-pVQZ basis sets were utilized). In analogy with the mentioned above Ne_2 and Ar_2, the ionization energies were added to those of the ground state of the neutral to obtain the PECs for the singly, doubly and triply ionized system. In all calculations the spin-orbit effects were neglected.

The resulting potential curves were shifted to match at 10.0 Å the spectroscopic data of the separated atoms [3, 51] in order to obtain the correct absolute energy scale. These PECs were than used to compute the ICD electron spectra of the decaying states within the framework of the time-dependent theory of wave packet propagation.

2.2.4 Small biochemically relevant hydrogen bonded systems

The ionization spectra used in our study are computed in the following manner: the ground state geometries of the hydrogen bonded systems are optimized with the second-order Møller-Plesset (MP2) method, using the aug-cc-pVTZ basis set for sulfur and d-aug-cc-pVTZ basis sets for all other atoms. The calculations were performed with the MOLPRO quantum chemistry package [45]. All of the structures have C_s symmetry and

in all but one of them the proton donor and the proton acceptor molecules lie in perpendicular planes. The exception is $H_2O\cdots H_2CNH$ where all of the atoms are semiplanar.

The optimized geometries are utilized in the computations of the cationic and dicationic spectra in the relevant for our investigation range from 0 to 40 eV. The ionization potentials are computed within the framework of the Green's function approach using the so-called algebraic diagrammatic construction (ADC) scheme [33, 37], discussed in detail in the literature [34, 37, 46–48, 50]. ADC(n) implements infinite partial summations of perturbative terms of the appropriate Green's function, which are exact up to the n-th order of perturbation theory. Important features of this approach is its compactness and size-consistency. The single ionization spectra that include the energies of inner-valence-ionization are calculated via the non-Dyson ADC(3) scheme [38] for the one-particle Green's function. The ADC(2) scheme for the particle-particle propagator [34, 50] is used to compute the dicationic spectra and the analysis of the localization of the charges on the two subunits of the system is carried out employing the technique described in Ref. [52]. In all the ADC calculations the aug-cc-pVDZ basis set is used for S and the d-aug-cc-pVDZ basis sets for the other atoms.

Each vertical line in the computed spectra corresponds to a cationic state of the system. The position of the line is given by the corresponding ionization energy (or ionization potential), while the hight represents the spectral intensity (related to the ionization cross section [36]). The spectra shown are computed for fixed nuclear geometry (that of the equilibrium state) and thus reflect only the electronic degrees of freedom. That is why the spectra consist of discrete lines. The nuclear degrees of freedom do, of course, influence the ionization spectra introducing a vibrational broadening of the spectral lines reflecting the bonding character of each particular electron with respect to the various normal coordinates of the system. Computing ionization spectra taking into account the vibrational structure is not an easy task, especially for polyatomic systems. However, a fairly good approximation can be obtained by convoluting each line of the spectrum with a Gaussian function with appropriate width to account for the vibrational broadening.

In order to make our discussions easier to follow we resort in the text to a notation that differs from that used in group theory, while the usual C_s symmetry state assignmets are given in the tables supplementing the text. Depending on the system, the outer-valence shell molecular orbitals (MOs) are mainly composed of the atomic $2p$ orbitals of the respective carbon, nitrogen,or oxygen atoms, and of the atomic $3p$ orbitals in the case of sulfur. Consequently, we refer to them as $3p$ orbitals of S, $2p$ orbitals of O, etc.

and to their ionized states as $3p^{-1}$ state of S, $2p^{-1}$ state of N, etc. Similarly, the inner-valence MOs are referred to as $2s$ orbitals of C, N, and O and $3s$ orbitals of S, and the corresponding ionized states are denoted as $2s^{-1}$ and $3s^{-1}$.

2.2.5 Water dimer

The PECs and ionization spectra used in our study of water dimer were computed in the following manner. The ground state geometry of the hydrogen bonded cluster was optimized with the MP2 method for each of the oxygen-oxygen (O-O) separations studied. More precisely, the two O-atoms were frozen at several distances ranging from 2.10 to 10 Å and all the other bonds and angles were allowed to relax. These optimized structures were then used to calculate the potential energy curve of $(H_2O)_2$ employing CCSD(T) approach. The basis set superposition error was counterpoise corrected and d-aug-cc-pVTZ basis sets with an additional hydrogen-type bond function in the middle of the O-O distance were used for both the MP2 and CCSD(T) computations. The above calculations were performed with the MOLPRO package [45].

The optimized geometries of the ground state were also utilized in the computation of those cationic and dicationic spectra of the dimer relevant to our investigation. These spectra were computed within the framework of the Green's function approach using ADC scheme. The inner-valence-ionization energies of $(H_2O)_2$ were calculated via the ADC(3) scheme for the one-particle Green's function using the non-Dyson approach [38]. The ADC(2) scheme for the particle-particle propagator [34, 50] was used to compute the dicationic spectra of $(H_2O)_2$ and H_2O. In both ADC(3) and ADC(2) calculations d-aug-cc-pVDZ basis sets were employed. These energies were then added to those of the ground state of the neutral to obtain the PECs for the singly and doubly ionized system.

The geometry of the lowest in energy $H_2O^+H_2O^+$ state was also optimized at constant O-O distances in order to obtain the energy of the system containing two relaxed water cations. Here, third order multireference Rayleigh-Schrödinger perturbation theory (RS3) calculation was performed with the MOLPRO package [53] using d-aug-cc-pVQZ basis sets. The same level of precision was used to determine the energy of the ground state of H_2O^{3+}.

The computed PECs were shifted to match at large intermolecular distances the spectroscopic data of the separated molecules in order to obtain the correct absolute energy scale. For this purpose, the states calculated with the ADC(n) at 1000 Å and those calculated with RS3 at 100 Å are set equal to the corresponding experimental values from Ref. [54, 55] for the reported molecules. For the two-site dicationic states the Coulomb

repulsion of two point charges at these distances were taken into account.

As already mentioned, the ADC procedures for the various kinds of ionization processes are accurate through a given order of perturbation theory, i.e. one expects different accuracy for singly and doubly ionized states, as well as a different accuracy for those obtained by the RS3 method. However, we would like to stress again that for the kind of systems discussed here, the error depends rather weakly on the intermolecular distance and can be well eliminated by the just described asymptotic adjustments of the corresponding PECs to the molecular spectroscopic data. The ionization spectra reported contain the *ab-initio* data as obtained from the calculations. The energies of the relevant singly and doubly ionized electronic states used to calibrate the energy scale are presented in Table 4.1 and Table 4.2, respectively. Note that in the experimental [55] and theoretical [56,57] studies on the Auger decay of H_2O only nine maxima in the electron spectrum have been observed. Those correspond to sixteen electronic configurations that are populated after the core ionization of water and that are present in our ADC(2) computation and in Ref. [58], as well. We have adopted the peak numbering of Refs. [55–57], see the last column of Table 4.2 and have only additionally assigned as peak 3.1 (P3.1) the experimental energy of $H_2O^{++}(2a_1^{-1}3a_1^{-1}\ ^1A_1)$.

We need to clarify the notation which we will be using. The four valence molecular orbitals (MOs) of H_2O in C_{2V} symmetry are denoted as $1b_1$, $3a_1$, $1b_2$, and $2a_1$. The first three represent the outer valence shell of the molecule and are formed with participation of the $2p$ orbitals of oxygen, thus for brevity we will sometimes refer to these outer-valence orbitals as $2p$ type MOs, to their singly ionized states as $2p^{-1}$, and to their doubly ionized states as $2p^{-2}$. The main contribution to the $2a_1$ MO comes from the $2s$ orbital of oxygen and we will refer to it as the $2s$ type MO, to its singly ionized states as $2s^{-1}$, and to its doubly ionized states as $2s^{-2}$. If we have a dicationic state with a hole in $2a_1$ and a hole in either $1b_1$, $3a_1$, or $1b_2$ we will refer to it as $2s^{-1}2p^{-1}$. For $(H_2O)_2$, the eight valence orbitals ordered in increasing energy at the equilibrium geometry of the dimer are in C_s symmetry: $2a''$, $8a'$, $7a'$, $6a'$, $5a'$, $1a''$, $4a'$, and $3a'$. Each of these can be related to either the proton donor ($H_2O_{d.}$) or the proton acceptor ($H_2O_{a.}$) water molecule in the dimer. According to their asymptotic behavior, these orbitals can be divided into four pairs where each pair merges to a MO of H_2O: $2a''$ and $8a'$ to $1b_1$, $7a'$ and $6a'$ to $3a_1$, $5a'$ and $1a''$ to $1b_2$, and $4a'$ and $3a'$ to $2a_1$, see Table 4.1. In this way we have assigned the states of the dimer to the experimental data of the water molecule and adjusted asymptotically the corresponding PECs as discussed above.

Chapter 3

Relaxation processes following Auger decay in noble gas clusters

3.1 Neon dimer

The neon dimer happens to be especially suitable for investigating different aspects of the ICD and related decay processes. It contains two atoms with ten electrons and when separated the system has two closed shell subunits. The interesting for us decay states are described by the main lines in the single, double, and triple ionization spectrum. Those spectral lines exhibit high intensities, are easy to distinguish and interpret. Thus, we shall begin our study of the ICD following Auger decay in noble gas clusters with Ne_2 and shall later continue the discussion with the phenomena characteristic for Ar_2 and NeAr.

Important feature of this cascade decay is that the electronic states that undergo ICD have already been doubly ionized. Thus, at the end of the interatomic process a singly and a doubly ionized particles are created. This means that both the 'direct' and 'exchange' ICD, as well as the ETMD will be followed by a Coulombic explosion which will tear apart the weak bond between the two subunits of the system. The two step relaxation mode of Ne_2 was unambiguously identified experimentally with the help of electron-ion-ion coincidence spectroscopy [24], that proved the theoretical prediction of Ref. [20].

3.1.1 Direct ICD following Auger

The KLL Auger decay in atomic Ne populates several dicationic states [59] (see Table 3.1). In the dimer, all of them can further decay by interatomic processes. We will first investigate in more detail the cascade process of direct ICD following KLL Auger, as far as

it is the fastest and can be successfully described neglecting the nuclear dynamics in the dimer. The other processes are then treated systematically as a function of total energy of the states involved in them in the next sections. As will appear more clearly later on, the direct ICD channel is open only from the $Ne^{++}(2s^{-1}2p^{-1}\ ^1P)$-Ne state, taking about 17% of the population of all KLL Auger final states. The PECs of the different electronic states involved in this process are presented in Fig. 3.1. The curve of the ground state of the weakly bound neon dimer is shown in panel (a) of the figure. It is characterized by a very shallow minimum at 3.10 Å, in good agreement with other computations [60–63] and experimental results [64] reported in the literature.

The two-site states shown in the figure can, in principle, be directly formed by the Auger decay. However, the distance between the two argon atoms in the ground state of the dimer is large and this makes the probability of participation of both atoms in the Auger process practically negligible. In fact, weakly bound van der Waals clusters are good examples for *self-imaging* Auger, a decay process that takes place on one center only and serves to detect a specific atom.

Table 3.1: States and energies of the neon atomic ions relevant for the Auger decay and ICD. All data are taken from NIST [3] database, except for the number indicated by * (from Ref. [51]). The spectroscopic data is averaged over the total angular momentum. The relative intensities of the KLL Auger transition are taken from ref. [59].

Charge	Electronic state	Energy [eV]	Intensity of KLL in %
Ne^{3+}	$2p^{-3}\ ^2P$	133.69	-
	$2p^{-3}\ ^2D$	131.07	-
	$2p^{-3}\ ^4S$	125.95	-
Ne^{++}	$2s^{-2}\ ^1S$	121.89	6.2
	$2s^{-1}2p^{-1}\ ^1P$	98.42	16.8
	$2s^{-1}2p^{-1}\ ^3P$	87.89	6.8
	$2p^{-2}\ ^1S$	69.44	8.5
	$2p^{-2}\ ^1D$	65.73	61.7
	$2p^{-2}\ ^3P$	62.57	-
Ne^{+}	$1s^{-1}\ ^2S$	870.27*	-
	$2s^{-1}\ ^2S$	48.48	-
	$2p^{-1}\ ^2P$	21.60	-

In Fig. 3.1(c) the PEC of the system after the initial core ionization, i.e. of $Ne^{+}(1s^{-1})$-Ne, is depicted. Two states arise for this configuration – $^2\Sigma_g^+$ and $^2\Sigma_u^+$, which are practically degenerate and have minimum at 2.30 Å. Due to polarization effects, the PEC

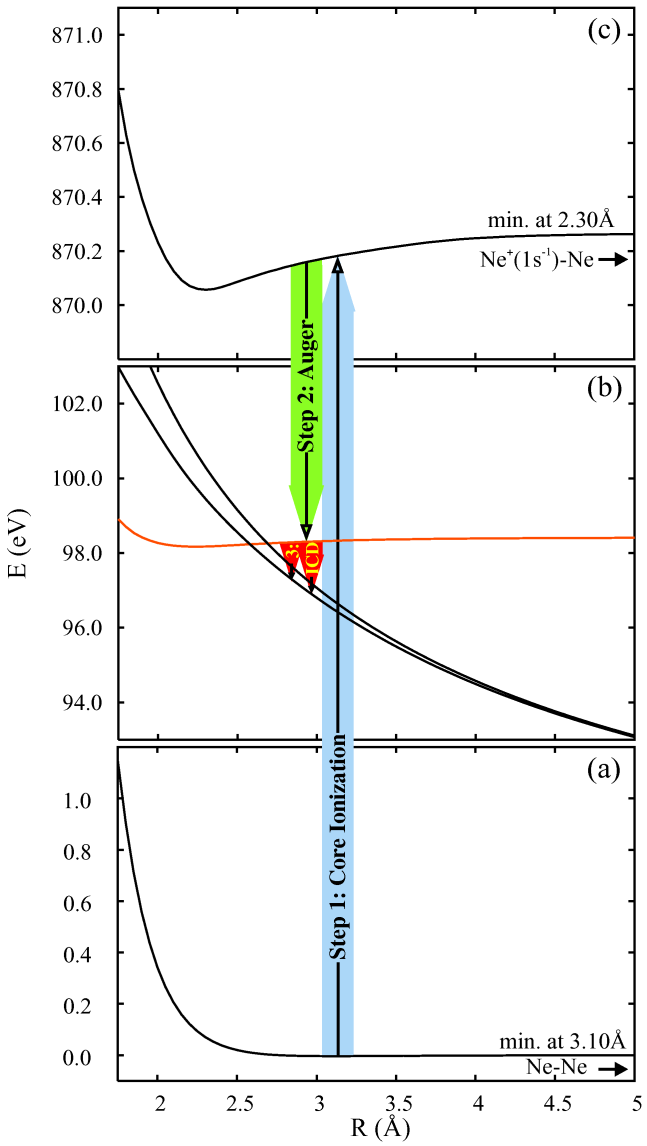

Figure 3.1: Computed potential energy curves (PECs) of the states of Ne_2 involved in the Auger decay following $1s$ ionization and in the subsequent direct Interatomic Coulombic Decay (ICD) process. (a) Neutral ground state; (b) Dicationic one-site state undergoing ICD (orange curve) and final triply ionized states (black curves); (c) Singly ionized $1s^{-1}$ state. Note that the energy scale in (b) differs from that in (a) and (c). The vertical arrows indicate the steps of the decay cascade: Step 1 (blue background): core ($1s$) ionization; Step 2 (green background): Auger decay; Step 3 (red background): ICD. For further details see the text.

exhibits a deeper well compared to that of the ground state of the neutral dimer. The bound $Ne^{++}(2s^{-1}2p^{-1}\ ^1P)$-Ne state (orange curve) together with the repulsive triply ionized Ne^{++}-Ne^+ states (black curves), which are the final states of the direct ICD process are shown in Fig. 3.1(b). To the best of our knowledge, the PECs for these ionic states of Ne_2 have not been previously.

The three consecutive steps describing the cascade process of direct ICD following KLL Auger are shown in Fig. 3.1. Arrows are used to schematically represent the transitions between the PECs of the states involved. The first step, represented by a black arrow on a blue background, is the core ionization of the system, whereby a $1s$ vacancy in one of

the neon atoms is created:

$$\text{Ne-Ne} \xrightarrow{h\nu} \text{Ne}^{+}(1s^{-1}\ {}^{2}S)\text{-Ne} + e^{-}_{photo}.$$

The resulting highly excited ionic state undergoes Auger decay, i.e. the $1s$ hole is filled by a $2s$ electron and a secondary Auger electron is emitted from the $2p$ shell of the same neon atom. This second step is illustrated by the black arrow on a green background in 3.1 and can be written as:

$$\text{Ne}^{+}(1s^{-1}\ {}^{2}S)\text{-Ne} \longrightarrow \text{Ne}^{++}(2s^{-1}2p^{-1}\ {}^{1}P)\text{-Ne} + e^{-}_{Auger}.$$

In the third step, this one-site dicationic state undergoes ICD. The vacancy in the $2s$ level is filled by an electron from the same neon and the energy released is transferred to the neighboring atom which uses it to emit one of its $2p$ electrons. These transitions are represented by a set of black arrows on a red background in Fig. 3.1(b), and lead to the final repulsive $\text{Ne}^{++}(2p^{-2}\ {}^{1}D)$-$\text{Ne}^{+}(2p^{-1})$ curves. After the direct ICD process a Coulomb explosion will take place as a result of the repulsion between the positive charges in the two centers of the dimer. This can be written as:

$$\text{Ne}^{++}(2s^{-1}2p^{-1}\ {}^{1}P)\text{-Ne} \longrightarrow \text{Ne}^{++}(2p^{-2}\ {}^{1}D) + \text{Ne}^{+}(2p^{-1}\ {}^{2}P) + e^{-}_{ICD},$$

with the energy balance:

$$E_{Ne^{++}(2s^{-1}2p^{-1}\ {}^{1}P)-Ne} = E_{Ne^{++}(2p^{-2}\ {}^{1}D)} + E_{Ne^{+}(2p^{-1}\ {}^{2}P)} + E_{e^{-}_{ICD}} + \text{KER}.$$

The final kinetic energy of the two neon ions is equal to the Coulomb repulsion of a single and a double point charge separated by the initial distance between the two neon atoms. This is a consequence of the timescale of the KLL Auger decay, which in the case of the neon atom is about 2.5 fs [6], thus being much faster than the nuclear motion in the dimer. The subsequent ICD is also expected to be fast - the total lifetime of the process was calculated to be 80 fs [20]. Hence, the internuclear distance will not change much during the cascade process and will stay approximately the same as in the ground state of Ne_2, namely around 3.10 Å. This amounts to a kinetic energy release (KER) of 9.3 eV, while the energy of the emitted ICD electron will then be around 1.7 eV.

The impact of nuclear dynamics accompanying the dICD of Ne_2 is discussed in detail in Ref. [65]. There, the PECs of $\text{Ne}^{+}(1s^{-1})$-Ne, $\text{Ne}^{++}(2s^{-1}2p^{-1}\ {}^{1}P)$-Ne, and $\text{Ne}^{++}(2p^{-2}\ {}^{1}D)$-$\text{Ne}^{+}$ shown in Figs. 3.1 are used and the total and partial ICD electron spectra are

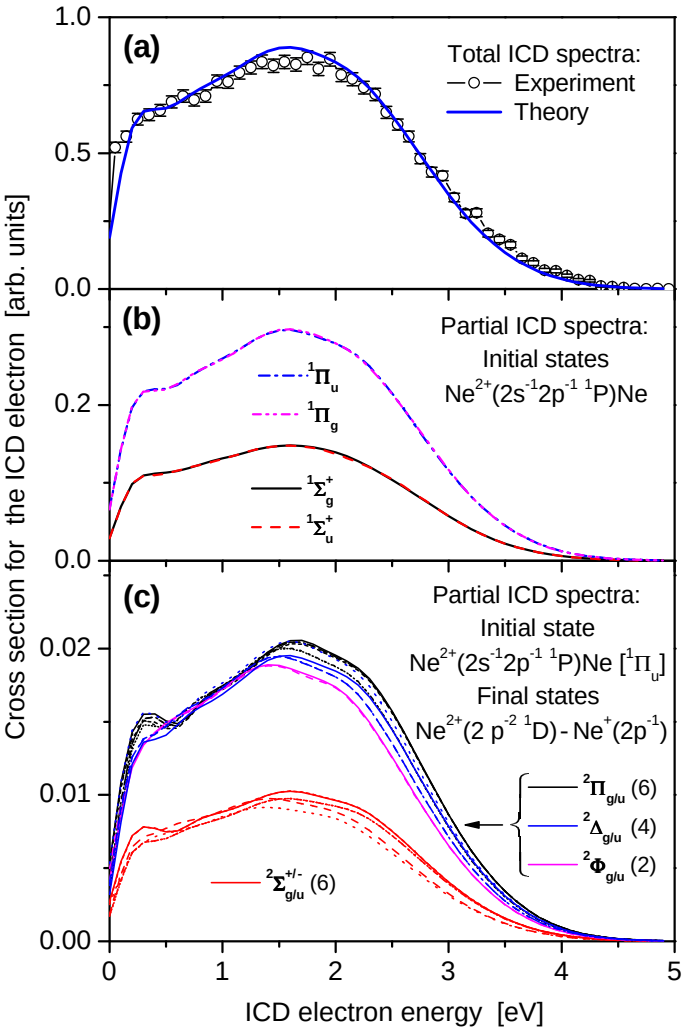

Figure 3.2: (a) Comparison of the computed [65] and measured [66] ICD electron spectra. The area of the computed cross section was set equal to that of the measured one. (b) Computed partial electron spectra of the decay of the $^1\Sigma^+_{g,u}$ and $^1\Pi_{g,u}$ initial $Ne^{++}(2s^{-1}2p^{-1}\,{}^1P)$-Ne states. (c) Computed partial spectra of the decay of $Ne^{++}(2s^{-1}2p^{-1}\,{}^1P)$-Ne $[^1\Pi_u]$ initial state into the selective manifold of $Ne^{++}(2p^{-2}\,{}^1D)$-Ne^+ final doublet states. For further details see Ref. [65] from which the figure is taken.

computed within the framework of the time-dependent theory of wave packet propagation (see Fig. 3.2). The computations were carried out using the partial ICD transition rates that had been chosen to be equal for different ICD channels and approximated by the analytical R^{-6} behavior valid at asymptotical interatomic distances R. It was shown that the partial electron spectra computed for different $Ne^{++}(2s^{-1}2p^{-1}\,{}^1P)$-Ne initial states undergoing ICD have a very similar shape. The partial spectra associated with different $Ne^{++}(2p^{-2}\,{}^1D)$-Ne^+ final states of the ICD illustrated a remarkable dependence on the corresponding crossing point between the PECs of the initial and the final ICD states. The computed total ICD electron spectrum is in a very good agreement with the recent measurements [66]. Its maximum is at the position predicted using the PECs of the initial and final states only, see also Table 3.3. The asymmetry in the shape of the total ICD spectrum including the shoulder on its low electron energy side, as well as the shift of its maximum to lower energies compared to the vertical electronic transition are shown to

be clear fingerprints of the nuclear dynamics accompanying the electronic decay.

3.1.2 Other interatomic processes following KLL Auger decay in neon dimer

As was mentioned in the previous section the decay of $Ne^+(1s^{-1})$-Ne populates with different probability several dicationic states. The core ionization energy is 870.273 eV [51], much larger than the energy of dimers having two holes in $2s$ and $2p$ levels and their excited states. This means that relaxation channels resulting in both (one-site) Ne^{++}-Ne and Ne^{3+}-Ne, and (two-site) Ne^+-Ne^+ and Ne^{++}-Ne^+ are open. However, $Ne^+(1s^{-1})$-Ne is a typical core ionized state and the nature of the Auger decay will favor the creation of one-site dicationic states (Ne^{++}-Ne). These one-site states can relax and reach states lower in energy through photon emission, processes involving nuclear dynamics, or an interatomic decay, such as ICD and ETMD. In what follows we will discuss the possible decay channels of the Ne^{++}-Ne states and the three lowest in energy Ne^{3+}-Ne states.

Energy range 45 to 72 eV

We begin our analysis with the electronic states of doubly ionized Ne_2 lowest in energy. These are the states having two holes in the $2p$ level and their PECs are displayed in Fig. 3.3. One clearly distinguishes two types of blue curves – attractive ones for the $Ne^{++}(2p^{-2})$-Ne one-site bound states and repulsive ones for the $Ne^+(2p^{-1})$-$Ne^+(2p^{-1})$ two-site states.

The group of two-site states correlates at infinite separation with two Ne^+ ions in their ground state ^{2}P $2p^{-1}$. Only the potential curves with $^1\Sigma_g^+$ and $^3\Sigma_u^+$ character are shown in the figure which correspond to the lower and the upper limit of the energy band of that group. These states, as mentioned above, are essentially not populated by Auger decay.

Higher in energy lie the PECs of the $Ne^{++}(2p^{-2})$-Ne states which are clearly divided in three groups. They correlate at large distances with a neutral Ne atom and three different states of $Ne^{++}(2p^{-2})$. The lowest-lying group (dashed triplet curves) comprises a $^3\Sigma_u^-$ and a $^3\Pi_u$ states and correlates with Ne^{++} in its ^{3}P state. Higher in energy lie two groups of singlet states, the lower one going to $Ne^{++}(2p^{-2}\ ^1\mathrm{D})$ and the higher one going to $Ne^{++}(2p^{-2}\ ^1\mathrm{S})$. For both ^{1}D and ^{1}S states, potential curves of $^1\Sigma_u^+$ and $^1\Sigma_g^+$ character are shown in the figure. Due to the charge-induced dipole interaction, all of the PECs for $Ne^{++}(2p^{-2})$-Ne are characterized by deeper wells than that of the ground state of Ne_2 and their minima are shifted to shorter internuclear distances (between 2.15 and 2.30 Å),

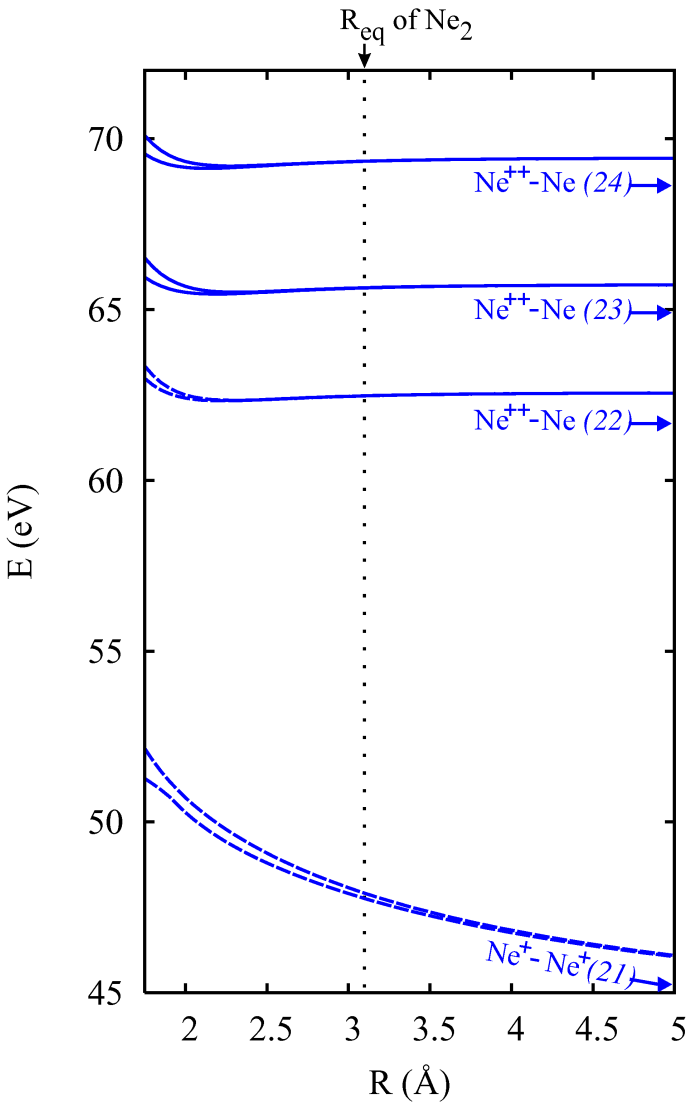

Figure 3.3: Computed potential energy curves of the doubly ionized neon dimer in the energy range 45 - 72 eV. The equilibrium internuclear distance of the neutral Ne_2 (3.10 Å) is marked by a vertical dotted line. The blue curves denote states of $2p^{-2}$. For further details see Table 3.2 and the text.

for details see Table 3.2. Considering the atomic Auger rates given in Table 3.1, we may conclude that the middle group of $Ne^{++}(2p^{-2})$-Ne states are those by far most populated by the KLL Auger transition in Ne_2, while the Auger transition to the triplet states is negligible.

Because the lowest in energy tricationic state is much higher in energy, ICD or other decay processes leading to the emission of an electron are not possible. The only conceivable relaxation pathway of these Ne^{++}-Ne states then is to Ne^{+}-Ne^{+}, i.e. the formation of two-site dications via radiative transition. Thus, we anticipate that the lowest-lying Ne^{+}-Ne^{+} states can only be populated by a radiative decay of the bound one-site states – $Ne^{++}(2p^{-2}\ {}^1D)$-Ne and $Ne^{++}(2p^{-2}\ {}^1S)$-Ne. Radiative transition from $Ne^{++}(2p^{-2}\ {}^3P)$-Ne is in principle also possible but, as was already mentioned, the probability that such state

Table 3.2: The computed ionized states of Ne_2 depicted in Figs. 3.1-3.5, ordered by decreasing energy at 1.75 Å. The energies are relative to the Ne_2 ground state at asymptotic distance.

Characterization by dissociation products	State	Equilibrium distance [Å]	Energy at 1.75 Å [eV]	Numbering in Figs. 3.3-3.5
$Ne^+(1s^{-1}\ ^2S)$-Ne	$^2\Sigma_g^+$	2.30	870.80	–[1]
$Ne^{++}(2s^{-1}2p^{-1}\ ^1P)$-$Ne^+(2p^{-1}\ ^2P)$	$^2\Sigma_u^+$	-	136.76	46
$Ne^{3+}(2p^{-3}\ ^2P)$-Ne	$^2\Sigma_u^+$	2.15	134.56	48
$Ne^{++}(2p^{-2}\ ^1S)$-$Ne^+(2s^{-1}\ ^2S)$	$^2\Sigma_u^+$	-	133.94	45
$Ne^{++}(2p^{-2}\ ^1S)$-$Ne^+(2s^{-1}\ ^2S)$	$^2\Sigma_g^+$	-	133.47	45
$Ne^{++}(2s^{-1}2p^{-1}\ ^1P)$-$Ne^+(2p^{-1}\ ^2P)$	$^2\Sigma_u^-$	-	131.98	46
$Ne^{++}(2p^{-2}\ ^1D)$-$Ne^+(2s^{-1}\ ^2S)$	$^2\Sigma_g^+$	-	131.34	43
$Ne^{3+}(2p^{-3}\ ^2D)$-Ne	$^2\Sigma_u^-$	2.10	131.18	48
$Ne^{++}(2p^{-2}\ ^1D)$-$Ne^+(2s^{-1}\ ^2S)$	$^2\Delta_g$	-	129.89	43
$Ne^{3+}(2p^{-3}\ ^4S)$-Ne	$^4\Sigma_g^-$	2.20	127.67	47
$Ne^{++}(2p^{-2}\ ^3P)$-$Ne^+(2s^{-1}\ ^2S)$	$^2\Pi_u$	-	127.44	42
$Ne^{++}(2p^{-2}\ ^3P)$-$Ne^+(2s^{-1}\ ^2S)$	$^2\Sigma_u^-$	-	127.27	42
$Ne^{++}(2s^{-1}2p^{-1}\ ^3P)$-$Ne^+(2p^{-1}\ ^2P)$	$^2\Pi_u$	-	126.47	41
$Ne^{++}(2s^{-1}2p^{-1}\ ^3P)$-$Ne^+(2p^{-1}\ ^2P)$	$^2\Pi_u$	-	125.10	41
$Ne^{++}(2s^{-2}\ ^1S)$-Ne	$^1\Sigma_g^+$	2.30	122.41	44
$Ne^{++}(2s^{-2}\ ^1S)$-Ne	$^1\Sigma_u^+$	2.15	122.28	44
$Ne^{++}(2p^{-2}\ ^1S)$-$Ne^+(2p^{-1}\ ^2P)$	$^2\Sigma_u^+$	-	108.90	35
$Ne^{++}(2p^{-2}\ ^1S)$-$Ne^+(2p^{-1}\ ^2P)$	$^2\Sigma_g^+$	-	107.38	35
$Ne^+(2s^{-1}\ ^2S)$-$Ne^+(2s^{-1}\ ^2S)$	$^1\Sigma_g^+$	-	106.18	37
$Ne^+(2s^{-1}\ ^2S)$-$Ne^+(2s^{-1}\ ^2S)$	$^3\Sigma_u^+$	-	106.01	37
$Ne^{++}(2p^{-2}\ ^1D)$-$Ne^+(2p^{-1}\ ^2P)$	$^2\Sigma_u^+$	-	105.29	34
$Ne^{++}(2p^{-2}\ ^1D)$-$Ne^+(2p^{-1}\ ^2P)$	$^2\Sigma_g^+$	-	102.98	34
$Ne^{++}(2p^{-2}\ ^3P)$-$Ne^+(2p^{-1}\ ^2P)$	$^2\Sigma_u^-$	-	101.17	33
$Ne^{++}(2p^{-2}\ ^3P)$-$Ne^+(2p^{-1}\ ^2P)$	$^2\Delta_u$	-	99.05	33
$Ne^{++}(2s^{-1}2p^{-1}\ ^1P)$-Ne	$^1\Pi_u$	2.25	98.91	36
$Ne^{++}(2s^{-1}2p^{-1}\ ^3P)$-Ne	$^3\Sigma_u^+$	2.25	88.28	32
$Ne^+(2s^{-1}\ ^2S)$-$Ne^+(2p^{-1}\ ^2P)$	$^1\Sigma_g^+$	-	79.18	31
$Ne^+(2s^{-1}\ ^2S)$-$Ne^+(2p^{-1}\ ^2P)$	$^3\Sigma_g^+$	-	78.09	31
$Ne^{++}(2p^{-2}\ ^1S)$-Ne	$^1\Sigma_g^+$	2.30	70.09	24
$Ne^{++}(2p^{-2}\ ^1S)$-Ne	$^1\Sigma_u^+$	2.15	69.55	24
$Ne^{++}(2p^{-2}\ ^1D)$-Ne	$^1\Sigma_g^+$	2.30	66.51	23
$Ne^{++}(2p^{-2}\ ^1D)$-Ne	$^1\Sigma_u^+$	2.20	65.94	23
$Ne^{++}(2p^{-2}\ ^3P)$-Ne	$^3\Pi_u$	2.30	63.34	22
$Ne^{++}(2p^{-2}\ ^3P)$-Ne	$^3\Sigma_u^-$	2.25	62.98	22
$Ne^+(2p^{-1}\ ^2P)$-$Ne^+(2p^{-1}\ ^2P)$	$^3\Sigma_u^+$	-	52.15	21
$Ne^+(2p^{-1}\ ^2P)$-$Ne^+(2p^{-1}\ ^2P)$	$^1\Sigma_g^+$	-	51.27	21

[1]See Fig. 1c.

is formed by KLL Auger decay is extremely small. The radiative charge transfer (CT) process in question and its energy balance are written in a compact form as:

$$\mathrm{Ne}^{++}(2p^{-2})\text{-Ne} \longrightarrow \mathrm{Ne}^{+}(2p^{-1}) + \mathrm{Ne}^{+}(2p^{-1}) + \text{photon},$$
$$E_{Ne^{++}(2p^{-2})-Ne} \longrightarrow 2E_{Ne^{+}(2p^{-1})} + h\nu + \mathrm{KER},$$

where $h\nu$ is the energy of the emitted photon. The radiative process is comparatively slow, thus the nuclei will have time to relax before the system starts to disintegrate by CT and the ensuing Coulomb explosion. Therefore, the transitions to the two-site states are expected to take place close to the minima of the PECs of the one-site $\mathrm{Ne}^{++}(2p^{-2}$ (^{1}D, ^{1}S))-Ne, i.e. around $R \sim 2.15$ - 2.30 Å. Using Coulomb law, the kinetic energy of the two Ne^{+} ions in the final state is expected to be 6.7 - 6.3 eV. It should be mentioned that this radiative charge transfer was observed in the argon dimer [67], where it appeared as a follow-up process of the $\mathrm{L_{2,3}M_1M_{2,3}}$ Auger decay.

Energy range 72 to 140 eV

The PECs of the electronic states lying in the energy regions 70-110 eV and 110-140 eV are depicted in Fig. 3.4 and Fig. 3.5, respectively. Let us first concentrate on the curves of Fig. 3.4. We see here two dicationic one-site states (bound orange curves) with minima at 2.25 Å. The lower lying one is a $^3\Sigma_u^+$ state and correlates at asymptotic distance with $\mathrm{Ne}^{++}(2s^{-1}2p^{-1}\ ^3\mathrm{P})$-Ne. Higher in energy is a $^1\Pi_u$ state which correlates with $\mathrm{Ne}^{++}(2s^{-1}2p^{-1}\ ^1\mathrm{P})$-Ne.

Repulsive curves of three types of electronic states are shown in Fig. 3.4. The pair of orange ones, in the lower part of the figure, corresponds to $\mathrm{Ne}^{+}(2s^{-1})$-$\mathrm{Ne}^{+}(2p^{-1})$ $^3\Sigma_g^+$ and $^1\Sigma_g^+$ states. The three pairs of black curves represent tricationic states. The lowest one (comprising $^2\Delta_u$ and $^2\Sigma_u^-$) correlates asymptotically to $\mathrm{Ne}^{++}(2p^{-2}\ ^3\mathrm{P})$-$\mathrm{Ne}^{+}(2p^{-1}\ ^2\mathrm{P})$, the middle one ($^2\Sigma_g^+$ and $^2\Sigma_u^+$) to $\mathrm{Ne}^{++}(2p^{-2}\ ^1\mathrm{D})$-$\mathrm{Ne}^{+}(2p^{-1}\ ^2\mathrm{P})$, and the upper one ($^2\Sigma_g^+$ and $^2\Sigma_u^+$) to $\mathrm{Ne}^{++}(2p^{-2}\ ^1\mathrm{S})$-$\mathrm{Ne}^{+}(2p^{-1}\ ^2\mathrm{P})$. Finally, the topmost, nearly degenerate green curves represent $^3\Sigma_u^+$ and $^1\Sigma_g^+$ states of $\mathrm{Ne}^{+}(2s^{-1})$-$\mathrm{Ne}^{+}(2s^{-1})$ character, respectively.

Let us now discuss the possible transitions between the states depicted in Fig. 3.4. The Auger decay will populate the one-site dicationic states depicted as orange attractive curves. At $R = 3.1$ Å, where the maximum of the wave packet is expected to be located after the Auger transition, the upper singlet state, $\mathrm{Ne}^{++}(2s^{-1}2p^{-1}\ ^1\mathrm{P})$-Ne, lies above two groups of tricationic states and thus can relax to them via ICD. The middle group of tricationic states, of $\mathrm{Ne}^{++}(2p^{-2}\ ^1\mathrm{D})$-$\mathrm{Ne}^{+}(2p^{-1}\ ^2\mathrm{P})$ character, can be populated by the

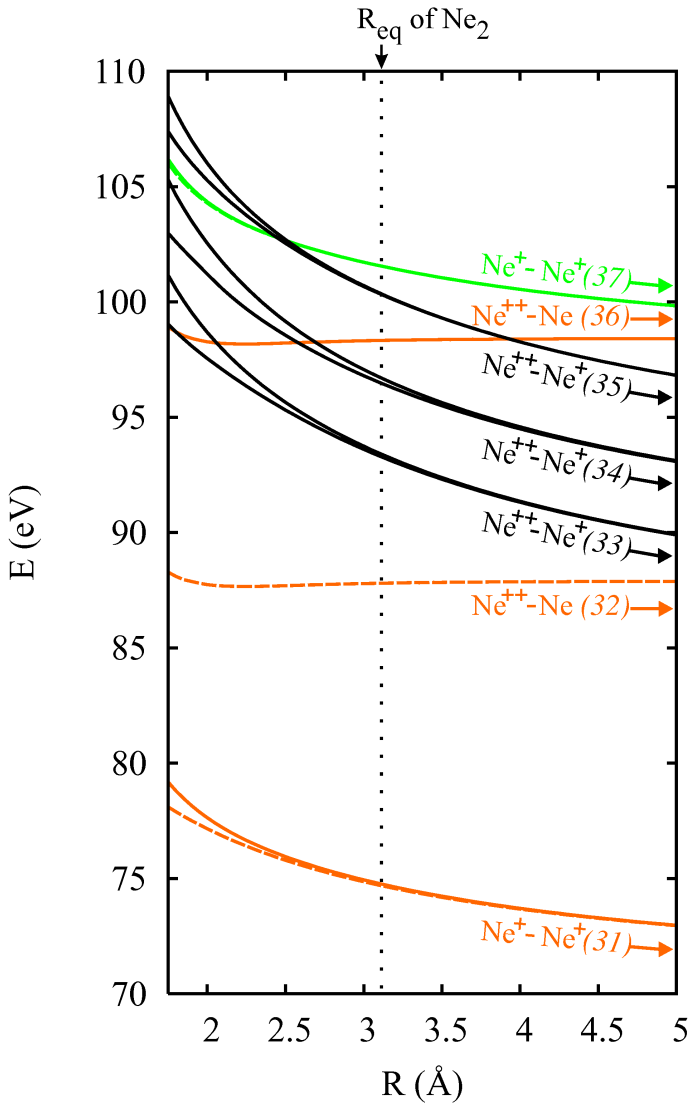

Figure 3.4: Computed potential energy curves of the doubly and triply ionized neon dimer in the energy range 70 - 110 eV. The equilibrium internuclear distance of the neutral Ne_2 (3.10 Å) is marked by a vertical dotted line. The orange and green curves denote states of $2s^{-1}2p^{-1}$ and $2s^{-2}$ character, respectively. The black curves are of the triply ionized states $Ne^{++}(2p^{-2})$-$Ne^{+}(2p^{-1})$. For further details see Table 3.2 and the text.

direct ICD mechanism already discussed in Sec. 3.1.1.

The lower lying group of triply ionized states, $Ne^{++}(2p^{-2}\ ^3P)$-$Ne^{+}(2p^{-1}\ ^2P)$, is not accessible by direct ICD, because the doubly ionized neon in the final state has triplet multiplicity that cannot be produced by the relaxation of $Ne^{++}(2s^{-1}2p^{-1}\ ^1P)$ without a spin-flip of the $2p$ electron. If one neglects spin-orbit coupling, this spin-flip ICD process is strictly forbidden. Although within jj coupling scheme this process is allowed, a rough estimation of the rates of the possible processes based on the experimentally reported spin-orbit splitting of the corresponding states [3] shows that the rate of the spin-flip ICD is several orders of magnitude smaller than those of the competing exchange ICD and ETMD.

Thus, one can safely assume that only exchange ICD or ETMD can take place here

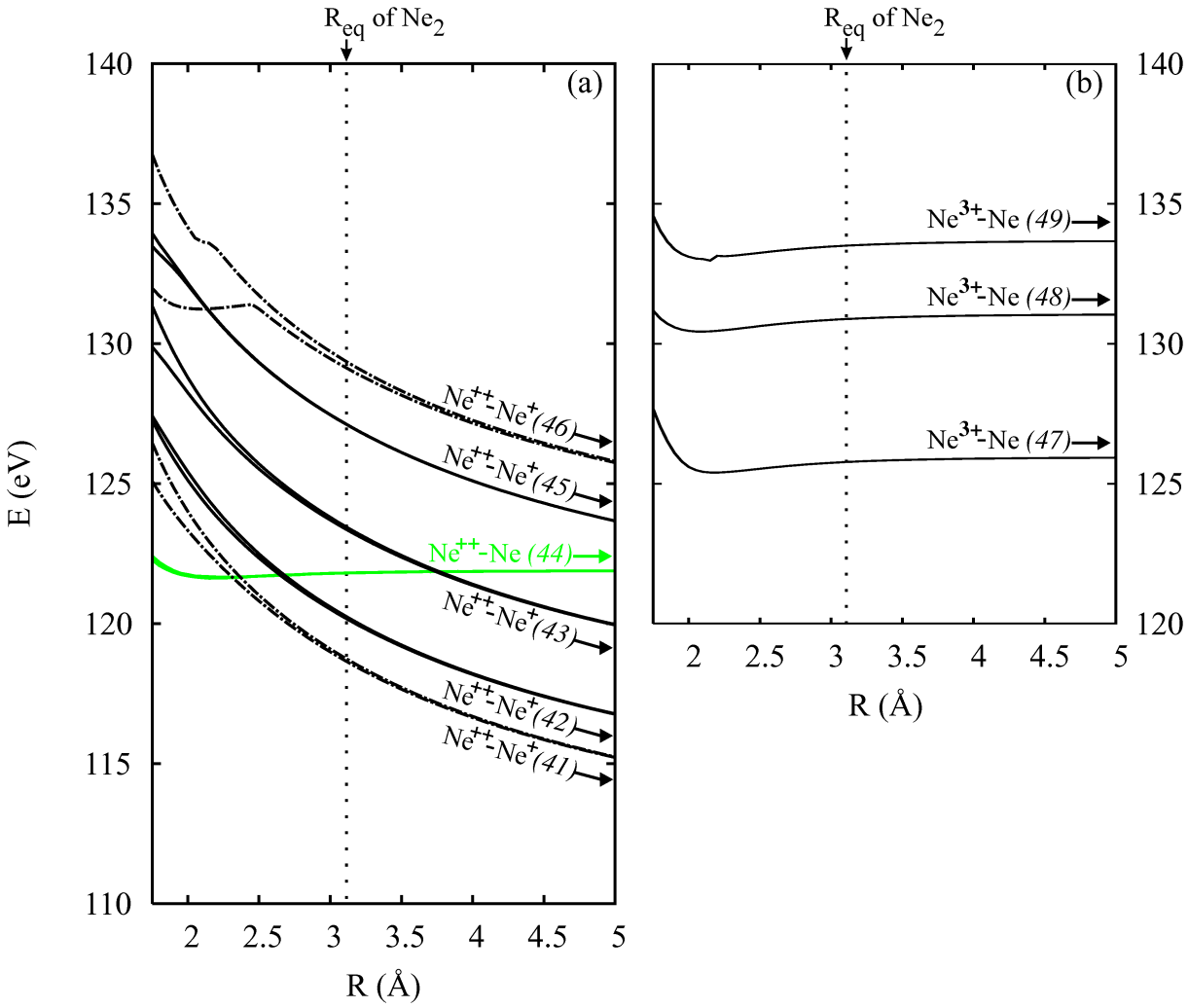

Figure 3.5: Computed potential energy curves of the doubly and triply ionized neon dimer in the energy range 110 - 140 eV. The equilibrium internuclear distance of the neutral Ne_2 (3.10 Å) is marked by a vertical dotted line. In panel (a), the green curves denote states of $2s^{-2}$ character. The dashed-dotted and solid black curves denote the two-site triply ionized states $Ne^{++}(2s^{-1}2p^{-1})$-$Ne^{+}(2p^{-1})$ and $Ne^{++}(2p^{-2})$-$Ne^{+}(2s^{-1})$, respectively. In panel (b), the solid black curves represent the triply ionized one-site states $Ne^{3+}(2p^{-3})$-Ne. For further details see Table 3.2 and the text.

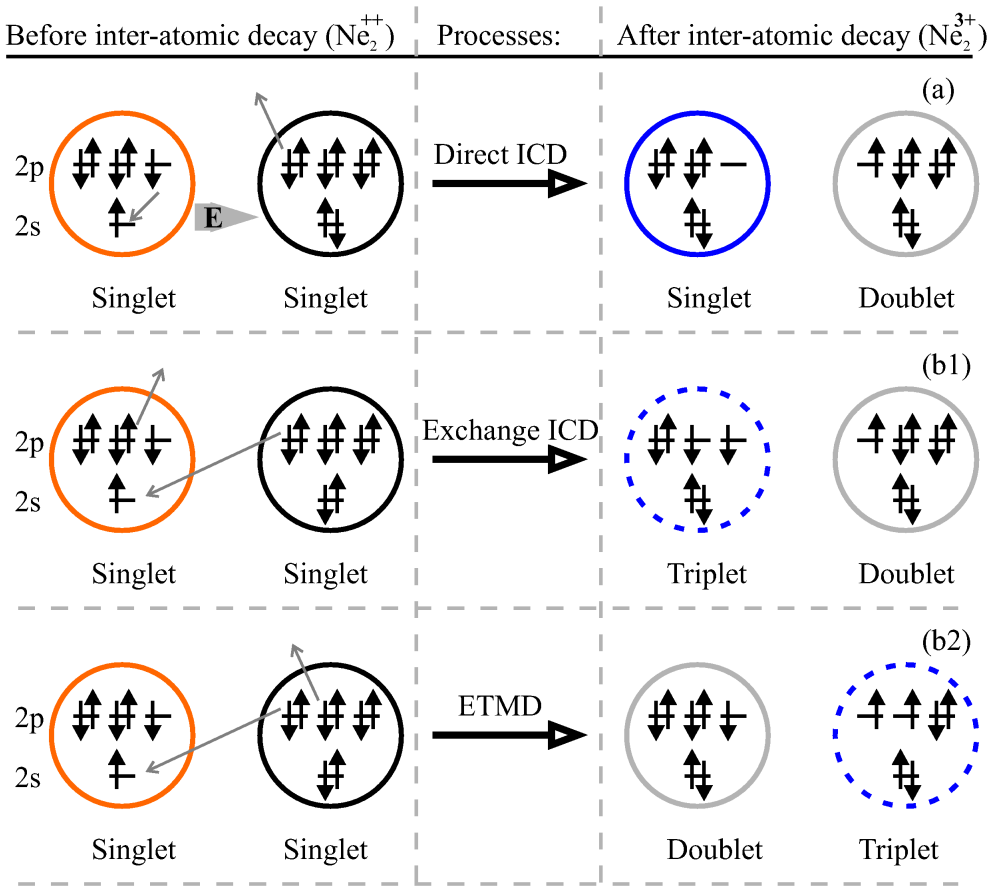

Figure 3.6: Schematic representation of the interatomic decay processes relevant for $Ne^{++}(2s^{-1}2p^{-1}\ ^1P)$-Ne. For further details see Table 3.3 and the text.

(see the schematic representation of the processes in Fig. 3.6). In the exchange ICD the $2s$ hole in the $Ne^{++}(2s^{-1}2p^{-1}\ ^1P)$ is filled by a $2p$ electron of the neutral neighbor and another $2p$ electron is ejected in the continuum from the initially doubly ionized neon, see Fig. 3.6(b1). In the ETMD process both $2p$ electrons – the one which fills the $2s$ hole in $Ne^{++}(2s^{-1}2p^{-1}\ ^1P)$ and the one ejected from the system – originate from the initially neutral neon, see Fig. 3.6(b2). Due to the symmetry of the system, the products of the exchange ICD and of the ETMD are the same, i.e. $Ne^{++}(2p^{-2}\ ^3P)$ and $Ne^{+}(2p^{-1}\ ^2P)$. Thus, in this case the two processes cannot be distinguished by the final products and identical equations will describe them:

$$\begin{aligned} Ne^{++}(2s^{-1}2p^{-1}\ ^1P) - Ne &\longrightarrow Ne^{++}(2p^{-2}\ ^3P) + Ne^{+}(2p^{-1}\ ^2P) + e^-_{eICD} \\ &\longrightarrow Ne^{+}(2p^{-1}\ ^2P) + Ne^{++}(2p^{-2}\ ^3P) + e^-_{ETMD}, \end{aligned}$$

$$E_{Ne^{++}(2s^{-1}2p^{-1}\ ^1P)-Ne} = E_{Ne^{++}(2p^{-2}\ ^3P)} + E_{Ne^{+}(2p^{-1}\ ^2P)} + E_{e^-_{eICD/ETMD}} + \text{KER}.$$

The energies of the emitted electrons are obtained by the difference between the energies of the doubly and triply ionized states involved. Their values at $R = 3.10$ Å are summarized in Table 3.3 along with the electronic configurations of the dimers undergoing the interatomic decay, the type of process they are involved in, and their final states. In the case of exchange ICD or ETMD, the emitted electrons are expected to have energies of about 5.0 eV if the decay takes place close to the equilibrium distance of the neutral species. However, the exchange ICD and ETMD are enhanced at shorter internuclear distances [25]. Therefore, more electrons will be emitted with lower energy and correspondingly higher KER of the back-to-back exploding ions. Examining the points of curve crossing of $Ne^{++}(2s^{-1}2p^{-1}\ ^1P)$-Ne and the Ne^{++}-Ne^{+} states we can in fact estimate the maximal KER. In Fig. 3.4, the curves of final states of the exchange ICD (or ETMD) cross the $Ne^{++}(2s^{-1}2p^{-1}\ ^1P)$-Ne PEC at distances shorter than 2.13 Å. This corresponds to a maximal KER of at least 13.5 eV. For the direct ICD process, the crossing occurs instead between 2.58 and 2.68 Å, which corresponds to a KER of 10.8 to 11.2 eV.

The highest lying group of triply ionized states in Fig. 3.4, $Ne^{++}(2p^{-2}\ ^1S)$-$Ne^{+}(2p^{-1}\ ^2P)$, crosses the dicationic $Ne^{++}(2s^{-1}2p^{-1}\ ^1P)$-Ne curve at $R \approx 3.8$ Å. Although the wave packet is expected to be quite broad, only a small fraction of its tail will spread beyond the point of curve crossing and decay to $Ne^{++}(2p^{-2}\ ^1S)$-$Ne^{+}(2p^{-1}\ ^2P)$ by ICD. Thus, although possible, we expect that this process will have a negligible rate.

The lower lying triplet one-site dicationic state, which is only weakly populated by Auger decay, is energetically below the triple ionization threshold, therefore cannot relax by ICD. However, this state can relax by photon emission to some of the two-site dicationic states, like $Ne^{+}(2s^{-1})$-$Ne^{+}(2p^{-1})$ or $Ne^{+}(2p^{-1})$-$Ne^{+}(2p^{-1})$, in a radiative CT process as discussed in the previous subsection.

Another important issue concerning the PECs in this region is that they interact noteably with states of the Rydberg series converging to the triply ionized neon dimer. This series consists of the superposition of the $2p^{-1}nl$ series on one neon and the $2p^{-2}nl$ series on the other one, forming a quasicontinuum of PECs covering the whole energy region below the highest black curve in Fig. 3.4. None of these states is shown in the figure, because they have very low intensity in the computed ionization spectra, and this does not allow the construction of reliable PECs from our data. However, we expect that, due to nonadiabatic coupling in the vicinity of the curve crossings between $Ne^{++}(2s^{-1}2p^{-1})$-Ne and the Rydberg $Ne^{+}(2p^{-2}nl)$-$Ne^{+}(2p^{-1}\ ^2P)$ states, a charge transfer can take place. Indeed, such charge transfer pathway involving nuclear dynamics was observed in Ar_2 as

Table 3.3: Electronic states of Ne_2^{++} which undergo interatomic decay to two-site Ne_2^{3+} states. Given are the type of the process, the expected energy (E) at which the kinetic energy distribution of the emitted electron is maximal (in eV), as well as the maximal KER of the back-to-back exploding ions (in eV).

	Type of process		E of the emitted electron [eV]		Maximal KER [eV]	
Before decay → After decay ↓	$Ne^{++}(2s^{-1}2p^{-1}\,{}^1P)$-Ne	$Ne^{++}(2s^{-2}\,{}^1S)$-Ne	$Ne^{++}(2s^{-1}2p^{-1}\,{}^1P)$-Ne	$Ne^{++}(2s^{-2}\,{}^1S)$-Ne	$Ne^{++}(2s^{-1}2p^{-1}\,{}^1P)$-Ne	$Ne^{++}(2s^{-2}\,{}^1S)$-Ne
$Ne^{++}(2p^{-2}\,{}^3P)$-$Ne^{+}(2p^{-1}\,{}^2P)$	Exchange ICD / ETMD	–[1]	< 5.0	–[1]	13.5 – 15.8	–[1]
$Ne^{++}(2p^{-2}\,{}^1D)$-$Ne^{+}(2p^{-1}\,{}^2P)$	Direct ICD	3 el. ICD	1.7	25.3	10.8 – 11.2	–[2]
$Ne^{++}(2p^{-2}\,{}^1S)$-$Ne^{+}(2p^{-1}\,{}^2P)$	–[1]	3 el. ICD	–[1]	21.4	–[1]	–[2]
$Ne^{++}(2s^{-1}2p^{-1}\,{}^3P)$-$Ne^{+}(2p^{-1}\,{}^2P)$	–[1]	Exchange ICD	–[1]	< 3.1	–[1]	12.0 – 12.6
$Ne^{++}(2p^{-2}\,{}^3P)$-$Ne^{+}(2s^{-1}\,{}^2S)$	–[1]	ETMD	–[1]	< 1.6	–[1]	10.9

[1]Decay channel is closed.

[2]Cannot be estimated.

a follow-up process of the $L_{2,3}M_1M_{2,3}$ Auger decay [22, 68].

Let us now examine the possible interatomic processes in the energy region 110-140eV, see Fig. 3.5(a) and (b). In Fig. 3.5(a) there are two nearly degenerate green curves representing two close-lying $^1\Sigma_g^+$ and $^1\Sigma_u^+$ states of $Ne^{++}(2s^{-2}\ ^1S)$-Ne character. The $^1\Sigma_g^+$ state has a minimum at 2.30 Å and the $^1\Sigma_u^+$ state at 2.15 Å. Two types of tricationic states can be distinguished. The dashed-dotted black curves describe the neon dimer with character $Ne^{++}(2s^{-1}2p^{-1})$-$Ne^+(2p^{-1})$ — the lower lying group of PECs ($^2\Pi_u$ and $^2\Pi_u$) correlate asymptotically with $Ne^{++}\ ^3P$ and $Ne^+\ ^2P$ and the higher lying PECs ($^2\Sigma_u^-$ and $^2\Sigma_u^+$) correlate with $Ne^{++}\ ^1P$ and $Ne^+\ ^2P$. The three pairs of solid black lines describe $Ne^{++}(2p^{-2})$-$Ne^+(2s^{-1})$ states. They all correlate with $Ne^+\ ^2S$, while the lower group ($^2\Sigma_u^-$ and $^2\Pi_u$) produces $Ne^{++}\ ^3P$, the middle group ($^2\Delta_g$ and $^2\Sigma_g^+$) – $Ne^{++}\ ^1D$, and the upper one ($^2\Sigma_g^+$ and $^2\Sigma_u^+$) – $Ne^{++}\ ^1S$.

At $R = 3.1$ Å the green one-site doubly ionized states have energy above the tricationic states $Ne^{++}(2s^{-1}2p^{-1}\ ^3P)$-$Ne^+(2p^{-1}\ ^2P)$ and $Ne^{++}(2p^{-2}\ ^3P)$-$Ne^+(2s^{-1}\ ^2S)$ and thus can relax to them via ICD or ETMD. Since the multiplicity of the doubly ionized fragment has to change from singlet to triplet in both cases, the decay via direct ICD would need a spin-flip and thus, as was discussed in the previous subsection, will have very low probability. However, the former tricationic state is accessible via exchange ICD while the latter via ETMD. Through exchange ICD, one of the $2p$ electrons of the neutral atom will fill a $2s$ vacancy in $Ne^{++}(2s^{-2}\ ^1S)$ and the energy released will be used to eject a $2p$ electron from the same site (see Fig. 3.7(a)). Thus, the $Ne^{++}(2s^{-1}2p^{-1}\ ^3P)$-$Ne^+(2p^{-1}\ ^2P)$ state will be reached. The trication will then break because of the Coulomb repulsion producing Ne^{++} and Ne^+ fragments with the corresponding KER. The process and its energy balance can be written as:

$$Ne^{++}(2s^{-2}\ ^1S)\text{-}Ne \longrightarrow Ne^{++}(2s^{-1}2p^{-1}\ ^3P) + Ne^+(2p^{-1}\ ^2P) + e^-_{eICD},$$

$$E_{Ne^{++}(2s^{-2}\ ^1S)-Ne} = E_{Ne^{++}(2s^{-1}2p^{-1}\ ^3P)} + E_{Ne^+(2p^{-1}\ ^2P)} + E_{e^-_{eICD}} + \text{KER}.$$

In the ETMD, again one of the $2p$ electrons of the neutral atom will fill a $2s$ vacancy in $Ne^{++}(2s^{-2}\ ^1S)$, but in this case the energy released is used to eject another electron from the initially neutral subunit (see Fig. 3.7(b)). Thus, after the ETMD process, the initially neutral neon will be in the doubly ionized ^3P state and $Ne^{++}(2p^{-2}\ ^3P)$-$Ne^+(2s^{-1}\ ^2S)$ trication will be produced. Fragmentation of the trication will then ensue as above.

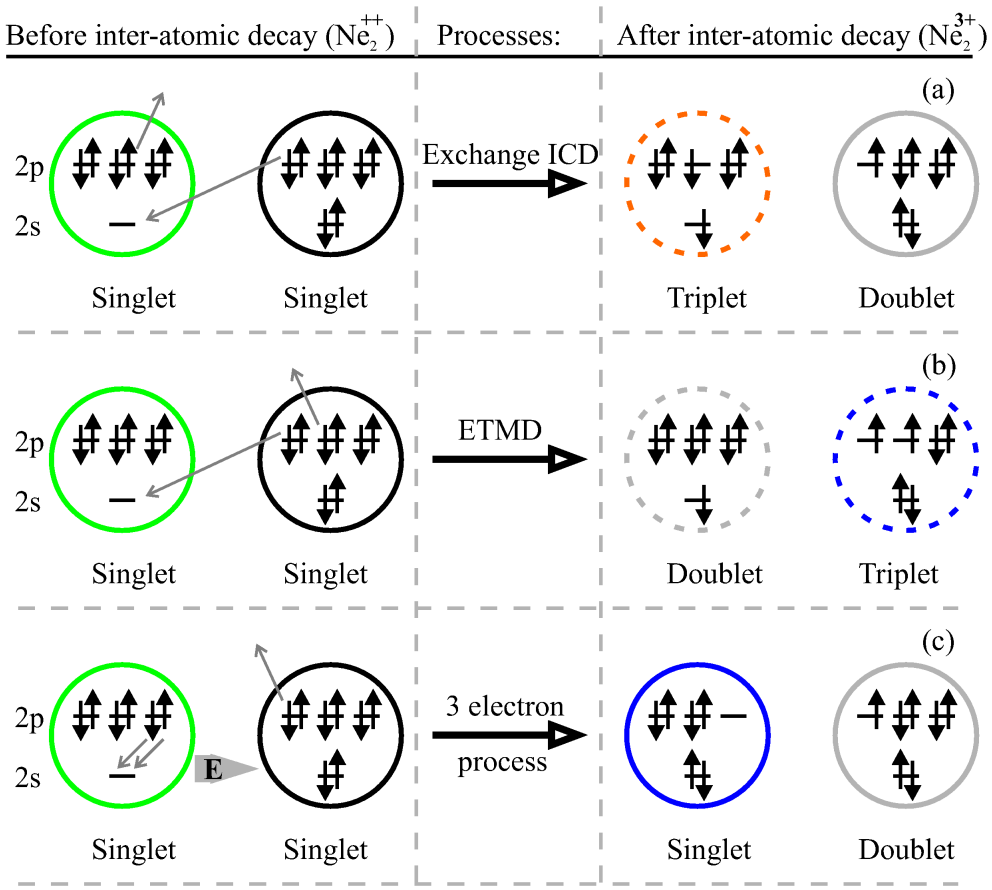

Figure 3.7: Schematic representation of the interatomic decay processes relevant for $Ne^{++}(2s^{-2}\ ^1S)$-Ne. For further details see Table 3.3 and the text.

Written in short:

$$Ne^{++}(2s^{-2}\ ^1S)\text{-}Ne \longrightarrow Ne^{+}(2s^{-1}\ ^2S) + Ne^{++}(2p^{-2}\ ^3P) + e^{-}_{ETMD},$$

$$E_{Ne^{++}(2s^{-2}\ ^1S)-Ne} = E_{Ne^{+}(2s^{-1}\ ^2S)} + E_{Ne^{++}(2p^{-2}\ ^3P)} + E_{e^{-}_{ETMD}} + \text{KER}.$$

Here, we have a case where exchange ICD and ETMD can be distinguished even for a homonuclear system. In a heteronuclear system, ICD and ETMD are easily distinguishable. The energies of the emitted electrons in these exchange ICD and ETMD processes can be deduced from the potential curves of the initial and final states involved. If both processes take place around the equilibrium distance of the neutral, i.e. around 3.1 Å, the kinetic energies of the outgoing electrons will be around 3.1 eV for the exchange ICD process, and around 1.6 eV for the ETMD. However, the efficiency of both processes increases exponentially with the decrease of the internuclear distance and we may thus expect that

the maximum in the energy spectra of the emitted electrons will be shifted to smaller values. This, of course, implies higher values of KER of the back-to-back exploding ions. The points of curve crossing of the dicationic and tricationic states involved determine the maximal value of KER. For the exchange ICD we have crossings between 2.3 and 2.4 Å corresponding to KER of 12.6 to 12.0 eV. The curves of the final states for the ETMD cross those of $Ne^{++}(2s^{-2}\ ^1S)$-Ne around 2.7 Å and thus the largest KER for this process is expected to be 10.9 eV. However, we must note at this point that the energies involved in this ETMD channel overlap those of the much more intense direct ICD channel discussed in Sec. 3.1.1. This will probably make the ETMD process difficult to discern in the data from electron-ion-ion coincidence measurements.

It should be noted that the triply ionized state $Ne^{++}(2p^{-2}\ ^1S)$-$Ne^{+}(2s^{-1}\ ^2S)$ crosses the state $Ne^{++}(2s^{-2}\ ^1S)$-Ne at approximately 3.8 Å. Consequently, for $R > 3.8$ Å another ETMD channel is open, but it will have very minor importance. At this separation ETMD is negligible anyway and, in addition, only a small fraction of the wave packet centered at 3.1 Å is expected to spread beyond that point.

Finally, we would like to mention another interesting possibility for interatomic decay of the $Ne^{++}(2s^{-2}\ ^1S)$-Ne state, though a less probable one. This dicationic state can also decay to $Ne^{++}(2p^{-2}\ ^1D)$-$Ne^{+}(2p^{-1}\ ^2P)$ and $Ne^{++}(2p^{-2}\ ^1S)$-$Ne^{+}(2p^{-1}\ ^2P)$, which lie lower in energy and are shown in Fig. 3.4. However, these interatomic processes are expected to be less efficient, since they involve three electrons: two $2p$ electrons have to fill the two $2s$ holes in one neon site, ejecting one $2p$ electron from the other one (see Fig. 3.7(c)). This ICD type process can be written as:

$$Ne^{++}(2s^{-2}\ ^1S)\text{-Ne} \longrightarrow Ne^{++}(2p^{-2}\ ^1D \text{ or } ^1S) + Ne^{+}(2p^{-1}\ ^2P) + e^{-}_{ICD},$$

$$E_{Ne^{++}(2s^{-2}\ ^1S)-Ne} = E_{Ne^{++}(2p^{-2}\ ^1D\ or\ ^1S)} + E_{Ne^{+}(2p^{-1}\ ^2P)} + E_{e^{-}_{ICD}} + \text{KER}.$$

If these processes take place at the equilibrium distance of the neutral, i.e. 3.1 Å, the energy of the ICD electrons will be 28.5 eV for the ^1D final state and 25.3 eV for ^1S final state. A summary of the expected KERs and secondary electron energies from all the interatomic processes discussed is given in Table 3.3.

For completeness we would like to mention that in this energy region there is another possibility for a cascade process initiated by the Auger decay of $Ne^{+}(1s^{-1})$-Ne. In principle, the neon $1s$ vacancy can decay via double Auger process producing one-site triply ionized sates Ne^{3+}-Ne [69]. Experimental results show that the ratio of the doubly and triply ionized ions produces by the decay of the core ionized system is $Ne^{3+}/Ne^{++} \approx$

0.081 [70]. In Fig. 3.5(b) we present the three attractive PECs which can be populated by the double Auger decay. The lower $^4\Sigma_g^-$ curve has minimum at 2.20 Å and $Ne^{3+}(2p^{-3}$ $^4S)$-Ne character, the middle $^2\Sigma_u^-$ curve has minimum at 2.10 Å and $Ne^{3+}(2p^{-3}$ $^2D)$-Ne character, and the higher $^2\Sigma_u^+$ curve has minimum at 2.15 Å and $Ne^{3+}(2p^{-3}$ $^2P)$-Ne character.

The presented $Ne^{3+}(2p^{-3})$-Ne states have energies below the quadruple ionization threshold and cannot autoionize or participate in an interatomic process accompanied by electron emission. Their PECs, however, interact with the repulsive curves of Ne_2^{3+} (see Fig. 3.5(a)) and we can expect the following process: after the double Auger decay has taken place, the nuclear wave packet will reside on the PECs of the one-site $Ne^{3+}(2p^{-3})$-Ne states and will be centered around the equilibrium internuclear distance of the neutral Ne_2, i.e. 3.1 Å. As time proceeds, the wave packet will start to propagate towards the minima of the curves and at the points of curve crossing there can be, due to nonadiabatic coupling, a transfer of population to the repulsive curves at $Ne^{++}(2p^{-2}$)-$Ne^+(2s^{-1})$ and $Ne^{++}(2s^{-1}2p^{-1})$-$Ne^+(2p^{-1})$. These charge transfer processes can be written as:

$$\begin{aligned} Ne^{3+}(2p^{-3})\text{-}Ne &\longrightarrow Ne^{++}(2p^{-2}) + Ne^+(2s^{-1}\ ^2S) \\ &\longrightarrow Ne^{++}(2s^{-1}2p^{-1}) + Ne^+(2p^{-1}\ ^2P) \end{aligned}$$

$$\begin{aligned} E_{Ne^{3+}(2p^{-3})-Ne} &= E_{Ne^{++}(2p^{-2})} + E_{Ne^+(2s^{-1}\ ^2S)} + \mathrm{KER} \\ &= E_{Ne^{++}(2s^{-1}2p^{-1})} + E_{Ne^+(2p^{-1}\ ^2P)} + \mathrm{KER}. \end{aligned}$$

The crossing points of 3.0 to 1.75 Å correspond to KER values of 9.6 and 16.4 eV.

3.2 Argon dimer

3.2.1 Direct ICD following Auger

In two recent publications Ueda and collaborators gave an experimental proof for the ICD process following Auger decay in argon clusters [21, 22]. There, this novel process is unambiguously identified by electron-ion-ion coincidence spectroscopy in which the kinetic energy of the ICD electron and the repulsion between Ar^+ and Ar^{++} were measured, Fig. 3.8. The ICD, as well as the related to it decay modes in Ar_2 can be successfully studied in a fashion similar to that used in the case of the neon dimer. Analyzing of the PECs of the argon dimer in the different states involved in the process provides a

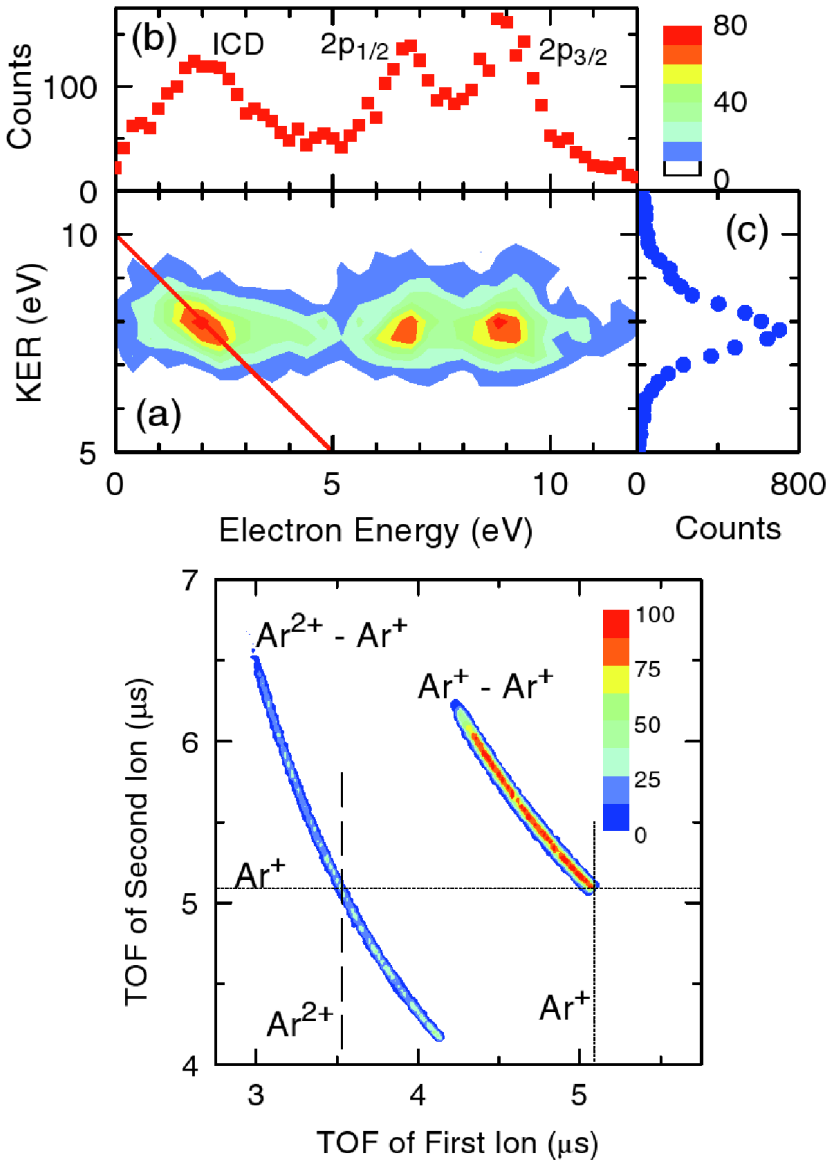

Figure 3.8: Upper panel: (a) Relationship between the electron energy and the total kinetic energy release (KER) of the Ar_2 fragmentation. (b) Electron energy distribution of the electron ejected from Ar dimers. (c) The KER of the Ar_2 fragmentation. Lower panel: Ar dimer ion-ion coincidence TOF spectrum. The dashed line shows the time-of-fight for zero-momentum Ar_2 ions, the dotted line for zero-momentum Ar ions. For further details see Ref. [21] from which the figure is taken.

description of the phenomenon.

The potential energy curve for the ground state of the weakly bound dimer Ar_2 is depicted in Fig. 3.9(a). The computed PEC is characterized by a very shallow minimum at 3.8 Å in very good agreement with other *ab initio* computations on the argon dimer [71–74], with calculations using semiempirical potentials [75], and with experimental results [76]. In Fig. 3.9(c) we present the PEC of the system after the initial $2p$ ionization, $Ar^+(2p^{-1})$-Ar. There are four states arising for this configuration which are practically degenerate: $^2\Sigma_g^+$, $^2\Sigma_u^+$, $^2\Pi_g$ and $^2\Pi_u$. These PECs have minima at 3.15 Å and exhibit a deeper well compared to that of the ground state. The Ar^{++}-Ar Auger one-site final states, which serve as initial states for the ICD process (orange curves), together with the

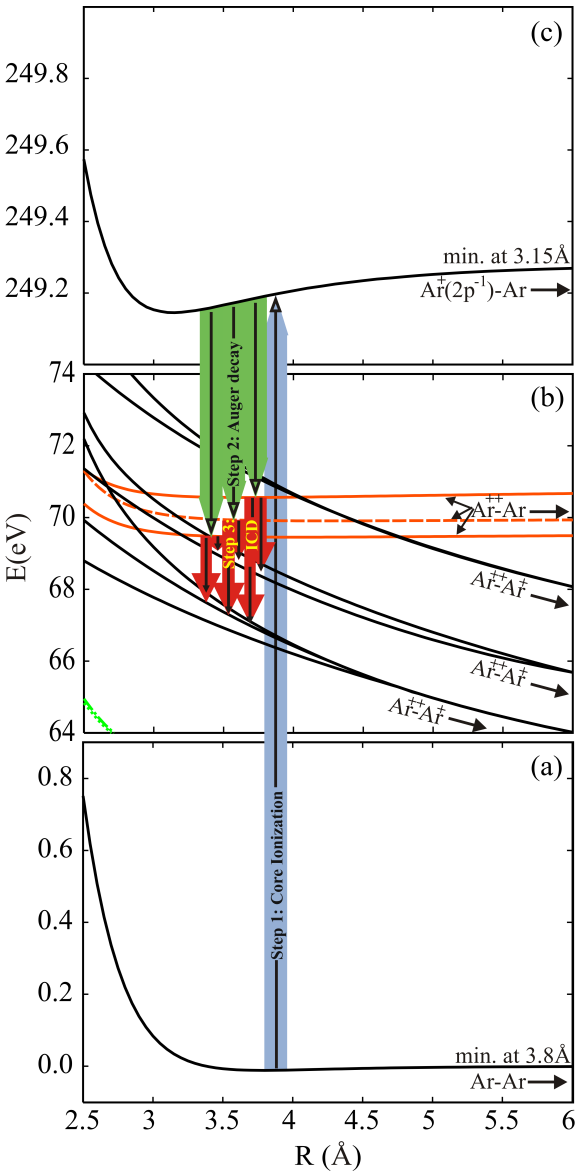

Figure 3.9: Computed potential energy curves (PECs) of the states of Ar_2 involved in the Auger decay following $2p$ ionization and in the subsequent Interatomic Coulombic Decay (ICD) process. (a) Neutral ground state; (b) Dicationic one-site satellite states undergoing ICD (orange curves) and final triply ionized states (black curves); (c) Singly ionized $2p^{-1}$ state. Note that the energy scale in (b) differs from that in (a) and (c). The vertical arrows indicate the steps of the decay cascade: Step 1 (blue background): core ($2p$) ionization; Step 2 (green background): Auger decay; Step 3 (red background): ICD. For further details see the text.

PECs for the Ar^{++}-Ar^{+} triply ionized final states of the ICD (black curves), are given in Fig. 3.9(b). To the best of our knowledge, the PECs for all these ionic states of Ar_2 have not been reported in the literature until now. In Fig. 3.9 the three consecutive steps that describe the cascade process are presented. Arrows are used to schematically represent the transitions between PECs of the states involved. The three steps are as follows:

Step 1 (Core Ionization), the Auger decay is initiated by creating a core hole in the $2p$ level of one of the argon atoms in Ar_2, shown by the black arrow on a blue background:

$$\text{Ar-Ar} \xrightarrow{h\nu} \text{Ar}^{+}(2p^{-1})\text{-Ar} + e^{-}_{photo}.$$

Step 2 (Auger decay), the singly ionized system relaxes by filling the hole in the $2p$ level with a $3s$ electron and emitting a secondary Auger electron from the $3p$ level of the same argon atom. The three black arrows on a green background denote the transition to the three one-site Auger final states relevant for the subsequent ICD (the three orange curves in Fig. 3.9(b)). None of these states can be assigned to a single configuration and they are essentially dicationic *satellite* states, as in this case the $3s^{-1}3p^{-1}$ and $3p^{-3}3d$ configurations are strongly mixed. Thus, the second step of the cascade process can be written as:

$$\mathrm{Ar}^{+}(2p^{-1})\text{-Ar} \longrightarrow \mathrm{Ar}^{++}(3p^{-3}(^2D)3d(+3s^{-1}3p^{-1}))\text{-Ar} + e^{-}_{Auger}.$$

Step 3 (ICD), the one-site dicationic states just produced undergo ICD. The vacancy in the $3s$ level is filled by an electron from the same argon and the energy released is transferred to the neighboring argon, from which a $3p$ electron (e^{-}_{ICD}) is emitted. These transitions are illustrated by a set of black arrows on a red background, and lead to the final repulsive Ar_2^{3+} curves. The process can be written as:

$$\mathrm{Ar}^{++}(3p^{-3}(^2D)3d(+3s^{-1}3p^{-1}))\text{-Ar} \longrightarrow \mathrm{Ar}^{++}(3p^{-2}) + \mathrm{Ar}^{+}(3p^{-1}) + e^{-}_{ICD}.$$

A Coulomb explosion follows as a result of the repulsion between the positive charges in the two centers of the dimer. The final kinetic energy of the two argon ions is equal to the Coulomb repulsion of a single and a double point charge separated by the initial distance between the two argon atoms. The timescale of the $\mathrm{L_{2,3}M_1M_{2,3}}$ Auger decay in argon atom is about 7 fs [77], much faster than the nuclear motion in the dimer. The subsequent ICD is also expected to be faster than the nuclear dynamics [9, 16]. Hence, the internuclear distance will not change much during the cascade process and will stay approximately the same as in Ar_2, namely around 3.8 Å. This was confirmed by the experiments of Ueda [21, 22].

Other processes that may occur in the ICD energy region, as well as possible pathways of relaxation of other Auger final states will be discussed below.

3.2.2 Electronic states of Ar_2^{++} and their decay into Ar_2^{3+}

As a result of the Auger decay from $\mathrm{Ar}^{+}(2p^{-1})$-Ar, electronic states other than those discussed in the previous section also appear. In fact, a rough estimate of the population of the one-site satellite states of $\mathrm{Ar}^{++}(3s^{-1}3p^{-1})$-Ar suggests that they represent less than 3% of all Auger final states. The core ionization energy is about 250 eV, much

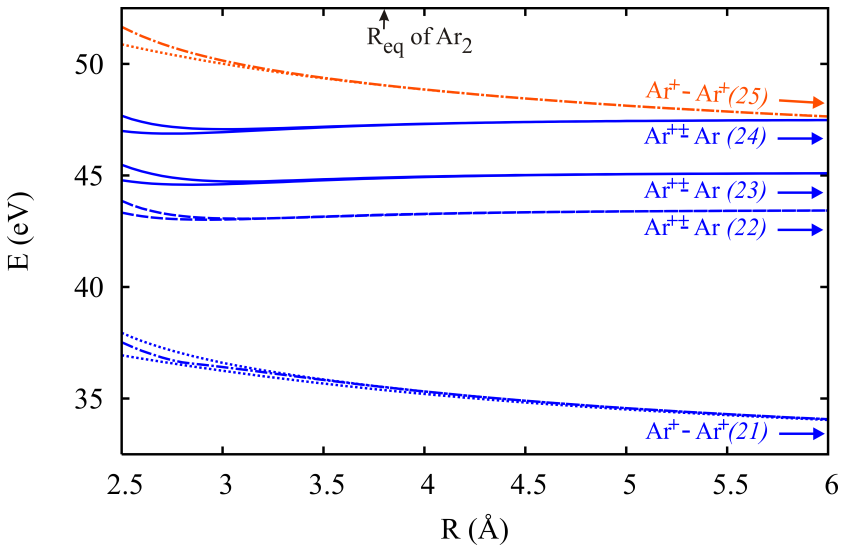

Figure 3.10: Computed potential energy curves of the doubly ionized argon dimer in the energy range 32 - 52 eV. The equilibrium internuclear distance of the neutral Ar_2 (3.80 Å) is marked by a vertical arrow. The blue and orange curves denote states of $3p^{-2}$ and $3s^{-1}3p^{-1}$ character, respectively. For further details see Table 3.5 and the text, as well as Ref. [67].

larger than the energy of dimers having two holes in their $3s$ and $3p$ levels, as well as their excited states. This opens relaxation channels resulting in both Ar^{++}-Ar (one-site) and Ar^{+}-Ar^{+} (two-site) states. Although, $Ar^{+}(2p^{-1})$-Ar is not a typical core ionized state, like those with a hole in $1s$ or $2s$ levels, the dissociating Ar^{+}-Ar^{+} states populated directly by the Auger decay are expected to be a negligible fraction, as also confirmed experimentally [21,67,78]. The nature of the Auger decay will favor the creation of one-site dicationic states (Ar^{++}-Ar) and these relax following diverse pathways.

Energy range 32 to 52 eV

We begin our analysis of the electronic states of doubly ionized Ar_2 with the states lowest in energy, the PECs of which are displayed in Fig. 3.10. As can be seen, at lowest energy states of $3p^{-2}$ character are found (blue curves), the $Ar^{+}(3p^{-1})$-$Ar^{+}(3p^{-1})$ two-site states (repulsive curves) lying below and well separated from the $Ar^{++}(3p^{-2})$-Ar one-site bound ones. In the uppermost region of the figure, $Ar^{+}(3s^{-1})$-$Ar^{+}(3p^{-1})$ two-site states (orange curves) begin to appear.

The group of two-site states at lowest energy correlate at infinite separation with two Ar^{+} ions in their ^2P $(3p^{-1})$ ground state. The group comprises states of singlet multiplicity

Table 3.4: States and energies of the argon atomic ions relevant for the Auger decay and ICD. All data are taken from NIST [3], except for the numbers indicated by * (from Ref. [1]) and & (from Ref. [79]). The spectroscopic data is averaged over the total angular momentum.

Charge	Electronic state	Energy [eV]
Ar^{++}	$3s^{-2}\ ^1S$	74.36
	$3p^{-3}(^2D)3d\ ^1P(48\%)(+3s^{-1}3p^{-1}\ ^1P\ (37\%))$	70.65
	$3p^{-3}(^2D)3d\ ^3P(60\%)(+3s^{-1}3p^{-1}\ ^3P\ (22\%))$	69.94
	$3s^{-1}3p^{-1}\ ^1P\ (43\%)(+3p^{-3}(^2D)3d\ ^1P\ (50\%))$	61.25
	$3s^{-1}3p^{-1}\ ^3P\ (76\%)(+3p^{-3}(^2D)3d\ ^3P\ (17\%))$	57.56
	$3p^{-2}\ ^1S$	47.51
	$3p^{-2}\ ^1D$	45.13
	$3p^{-2}\ ^3P$	43.46
Ar^{+}	$2p^{-1}\ ^2P$	249.28*
	$3s^{-1}3p^{-1}(^3P)4p\ ^2S$	49.98&
	$3p^{-2}(^1S)4p\ ^2P$	39.58
	$3p^{-2}(^1D)3d\ ^2P$	38.58
	$3p^{-2}(^1D)4p\ ^2P$	37.14
	$3p^{-2}(^1S)4s\ ^2S$	36.50
	$3s^{-1}\ ^2S$	29.24
	$3p^{-1}\ ^2P$	15.82

$^1\Sigma_g^+$ (two states), $^1\Sigma_u^-$, $^1\Pi_g$, $^1\Pi_u$, $^1\Delta_g$, and of triplet multiplicity $^3\Sigma_u^+$ (two states), $^3\Sigma_g^-$, $^3\Pi_g$, $^3\Pi_u$, $^3\Delta_u$ (see e.g. [80]). Of these only three, $^3\Pi_u$, $^1\Sigma_g^+$ and $^3\Sigma_u^+$, in order of increasing energy, are shown in the figure. At short distances, all the other PECs lie between the two displayed triplets.

Higher in energy lie the PECs for the bound $Ar^{++}(3p^{-2})$-Ar states. They are clearly divided in three groups correlating at large distances with three different states of $Ar^{++}(3p^{-2})$ (plus a neutral ground state Ar atom). The lower-lying group is of triplet multiplicity and correlates with Ar^{++} in its ^3P state. The two dashed blue curves represent the $^3\Sigma_u^-$ and $^3\Pi_u$ states of the system. The other PECs for the one-site triplets of $Ar^{++}(3p^{-2})$-Ar, namely $^3\Sigma_g^-$ and $^3\Pi_g$ (not shown) lie inbetween. The two higher-lying groups are singlets, the one at lower energy going the ^1D state of Ar^{++} and the higher energy one to the ^1S state. The curves of the $^1\Sigma_u^+$ and $^1\Sigma_g^+$ states enclose the PECs for the $Ar^{++}(3p^{-2}\ ^1D)$-Ar group, which also includes Π_g, Π_u, Δ_g and Δ_u states. For the $Ar^{++}(3p^{-2}\ ^1S)$-Ar group there are only two states: $^1\Sigma_u^+$ and $^1\Sigma_g^+$. Due to the charge-induced dipole interaction, all the PECs for $Ar^{++}(3p^{-2})$-Ar are characterized by deeper wells than that of the

ground state of Ar_2, and minima shifted to shorter internuclear distances (between 2.75 and 3.10 Å). For details see Table 3.5.

PECs of the one- and two-site dissociative states of Ar_2 with two holes in the $3p$ level have been reported in the literature by Cachoncinlle *et al.* [81] for both singlet and triplet states, and by Zaitsevskii and Dement'ev [82], and Daskalopoulou and Peyerimhoff [83] for the triplets. Whenever comparison can be made, these curves, obtained by wavefunction based ab initio methods, agree well with our results.

Finally, highest in energy in Fig. 3.10 lie the repulsive curves of the two-site states of the dication with holes in the $3s$ and $3p$ levels, i.e. $Ar^+(3s^{-1})$-$Ar^+(3p^{-1})$. The dotted orange curve stands for the $^3\Sigma_g^+$ state and the dashed-dotted orange curve for the $^1\Sigma_g^+$. There are additional PECs with Σ_u^+, Π_g and Π_u character for both singlet and triplet (not shown), which lie in the energy band delimited by the curves plotted. The main characteristics of the PECs of all states discussed in this subsection are summarized in Table 3.5.

The two-site states shown in Fig. 3.10 can, in principle, be directly formed by the Auger decay. However, as we already mentioned, the distance between the two argon atoms in the ground state of the dimer is large – about 3.8 Å – and this makes the probability of participation of both atoms in the Auger process practically negligible. In fact, weakly bound van der Waals clusters are good examples for *self-imaging* Auger, a decay process that takes place on one center only and serves to detect a specific atom.

The distance between the two argon atoms in the ground state of the dimer is large – about 3.8 Å – and this makes the probability of participation of both atoms in the Auger process practically negligible, like in the case of the Ne_2 discussed in 3.1.1. Thus, the formation of Ar^+-Ar^+ states (described by the repulsive curves in Fig. 3.10) is essentially possible only as a result of a relaxation process of one of the Ar^{++}-Ar states (described by the attractive curves in Fig. 3.10). Relaxation through nuclear motion may take place with some appreciable rate if the PECs of the states involved cross or get very near. The two repulsive orange curves shown in Fig. 3.10, describing the singlet and triplet states of $Ar^+(3s^{-1})$-$Ar^+(3p^{-1})$, do indeed cross those of the bound states of Ar^{++}-Ar at distances larger than 6 Å. But these crossings are very far from the minima of the PECs of the one-site states and therefore we conclude that the Ar^+-Ar^+ states of Fig. 3.10 are unlikely to be formed as a result of processes involving nuclear dynamics. As we shall see in the next subsection, this type of processes are characteristic of the PECs of Ar_2^{++} lying higher in energy.

Inspecting the relative position of the one-site and two-site dicationic states of $3p^{-2}$

Table 3.5: The computed ionized states of Ar_2 depicted in Figs. 3.9-3.12, ordered by decreasing energy at 6.00 Å. The energies are relative to the Ar_2 ground state at asymptotic distance.

Characterization by dissociation products	State	Equilibrium distance [Å]	Energy at 6.0 Å [eV]	Numbering in Figs. 3.10-3.12
$Ar^+(2p^{-1}\ ^2P)$-Ar	$^2\Sigma_g^+$	3.15	249.27	–[1]
$Ar^{++}(3s^{-2}\ ^1S)$-Ar	$^1\Sigma_g^+$	3.00	74.35	48
$Ar^{++}(3p^{-3}(^2D)3d\ ^1P(48\%)(+3s^{-1}3p^{-1}\ ^1P\ (37\%)))$-Ar	$^1\Sigma_g^+$	3.65	70.67	47
$Ar^{++}(3p^{-3}(^2D)3d\ ^3P(60\%)(+3s^{-1}3p^{-1}\ ^3P\ (22\%)))$-Ar	$^3\Sigma_g^+$	4.25	69.93	46
$Ar^{++}(3p^{-3}(^2D)3d\ ^1P(48\%)(+3s^{-1}3p^{-1}\ ^1P\ (37\%)))$-Ar	$^1\Sigma_g^+$	4.00	69.50	45[2]
$Ar^+(3s^{-1}3p^{-1}(^3P)4p)$-$Ar^+(3p^{-1}\ ^2P)$	$^1\Sigma_g^+$	-	68.34	44
$Ar^+(3s^{-1}3p^{-1}(^3P)4p)$-$Ar^+(3p^{-1}\ ^2P)$	$^3\Sigma_g^+$	-	68.30	44
$Ar^{++}(3p^{-2}\ ^1S)$-$Ar^+(3p^{-1}\ ^2P)$	$^2\Sigma_g^+$, $^2\Sigma_u^+$	-	68.13	43
$Ar^{++}(3p^{-2}\ ^1D)$-$Ar^+(3p^{-1}\ ^2P)$	$^2\Sigma_g^+$, $^2\Delta_g$	-	65.75	42
$Ar^{++}(3p^{-2}\ ^3P)$-$Ar^+(3p^{-1}\ ^2P)$	$^4\Sigma_g^-$, $^4\Delta_g$	-	64.08	41
$Ar^{++}(3p^{-2}\ ^3P)$-$Ar^+(3p^{-1}\ ^2P)$	$^2\Sigma_g^+$	-	64.08	41
$Ar^{++}(3s^{-1}3p^{-1}\ ^1P\ (43\%)(+3p^{-3}(^2D)3d\ ^1P\ (50\%)))$-Ar	$^1\Sigma_g^+$	3.20	61.28	37
$Ar^+(3s^{-1}\ ^2S)$-$Ar^+(3s^{-1}\ ^2S)$	$^1\Sigma_g^+$	-	60.87	36
$Ar^+(3s^{-1}\ ^2S)$-$Ar^+(3s^{-1}\ ^2S)$	$^3\Sigma_u^+$	-	60.87	36
$Ar^+(3p^{-2}(^1S)4p\ ^2P)$-$Ar^+(3p^{-1}\ ^2P)$	$^1\Sigma_g^+$	-	57.87	35
$Ar^+(3p^{-2}(^1S)4p\ ^2P)$-$Ar^+(3p^{-1}\ ^2P)$	$^3\Sigma_u^+$	-	57.87	35
$Ar^{++}(3s^{-1}3p^{-1}\ ^3P\ (76\%)(+3p^{-3}(^2D)3d\ ^3P\ (17\%)))$-Ar	$^3\Sigma_g^+$	3.20	57.54	34
$Ar^+(3p^{-2}(^1D)3d\ ^2P)$-$Ar^+(3p^{-1}\ ^2P)$	$^1\Sigma_g^+$	-	56.95	33
$Ar^+(3p^{-2}(^1D)3d\ ^2P)$-$Ar^+(3p^{-1}\ ^2P)$	$^3\Sigma_g^+$	-	56.88	33
$Ar^+(3p^{-2}(^1D)4p\ ^2P)$-$Ar^+(3p^{-1}\ ^2P)$	$^1\Delta_g$	-	55.42	32
$Ar^+(3p^{-2}(^1D)4p\ ^2P)$-$Ar^+(3p^{-1}\ ^2P)$	$^3\Sigma_u^+$	-	55.40	32
$Ar^+(3p^{-2}(^1S)4s\ ^2P)$-$Ar^+(3p^{-1}\ ^2P)$	$^1\Delta_g$	-	54.83	31
$Ar^+(3p^{-2}(^1S)4s\ ^2P)$-$Ar^+(3p^{-1}\ ^2P)$	$^3\Sigma_g^-$	-	54.81	31
$Ar^+(3s^{-1}\ ^2S)$-$Ar^+(3p^{-1}\ ^2P)$	$^1\Sigma_g^+$	-	47.65	25
$Ar^+(3s^{-1}\ ^2S)$-$Ar^+(3p^{-1}\ ^2P)$	$^3\Sigma_g^+$	-	47.64	25
$Ar^{++}(3p^{-2}\ ^1S)$-Ar	$^1\Sigma_g^+$	3.00	47.48	24
$Ar^{++}(3p^{-2}\ ^1S)$-Ar	$^1\Sigma_u^+$	2.75	47.48	24
$Ar^{++}(3p^{-2}\ ^1D)$-Ar	$^1\Sigma_g^+$	3.10	45.10	23
$Ar^{++}(3p^{-2}\ ^1D)$-Ar	$^1\Sigma_u^+$	2.85	45.10	23
$Ar^{++}(3p^{-2}\ ^3P)$-Ar	$^3\Pi_u$	3.10	43.43	22
$Ar^{++}(3p^{-2}\ ^3P)$-Ar	$^3\Sigma_u^-$	2.90	43.43	22
$Ar^+(3p^{-1}\ ^2P)$-$Ar^+(3p^{-1}\ ^2P)$	$^3\Sigma_u^+$	-	34.07	21
$Ar^+(3p^{-1}\ ^2P)$-$Ar^+(3p^{-1}\ ^2P)$	$^1\Sigma_g^+$	-	34.07	21
$Ar^+(3p^{-1}\ ^2P)$-$Ar^+(3p^{-1}\ ^2P)$	$^3\Pi_u$	-	34.04	21

[1] See Fig. 3.9(c).

[2] See also text in Sec. 3.2.2.

character in Fig. 3.10, we anticipate that, if at all, the lowest-lying Ar^+-Ar^+ states can only be populated by a radiative decay of the bound one-site states – $Ar^{++}(3p^{-2}\ ^3P)$-Ar, $Ar^{++}(3p^{-2}\ ^1D)$-Ar, and $Ar^{++}(3p^{-2}\ ^1S)$-Ar [67]. These $Ar^{++}(3p^{-2})$ states are the final states of the dominant $L_{2,3}M_1M_{2,3}$ Auger decay channel in the Ar atom [84] and it is expected that they will be the most populated states also in the Ar dimer. The radiative charge transfer (CT) process in question and its energy balance are written in a compact form as:

$$Ar^{++}(3p^{-2})\text{-Ar} \longrightarrow Ar^+(3p^{-1}) + Ar^+(3p^{-1}) + \text{photon},$$
$$E_{Ar^{++}(3p^{-2})-Ar} \longrightarrow 2E_{Ar^+(3p^{-1})} + h\nu + \text{KER},$$

where $h\nu$ is the energy of the emitted photon. The radiative process is slow and the nuclei have time to relax before the system starts to disintegrate by CT and Coulomb explosion. The transition to the two-site state is expected to take place close to the minima of the PECs of the one-site $Ar^{++}(3p^{-2}$ (^3P, ^1D, ^1S))-Ar states, i.e. around $R \sim 2.75$ - 3.10 Å. Using the Coulomb law, the kinetic energy of the two Ar^+ ions in the final state amounts to 5.24 - 4.65 eV. This radiative decay has been observed experimentally and discussed in detail in Ref. [67]. See also Refs. [85–87].

Energy range 52 to 65 eV

The PECs of the electronic states lying within the energy region 52-65 eV are depicted in Fig. 3.11. It is immediately evident that, as energy increases, the electronic states of the dication become denser, with many crossings and mixed character. There are only two curves representing bound one-site states, Ar^{++}-Ar, (the two attractive orange curves). They correspond to the $^3\Sigma_g^+$ state at lower energy and the higher $^1\Sigma_g^+$, both with two holes in the $3s$ and $3p$ levels of one of the argon atoms. The corresponding asymptotes involve ^3P and ^1P states of $Ar^{++}(3s^{-1}3p^{-1})$ but, as we already noted, a single configuration description is not appropriate for these states since there is a strong mixing of configurations of $Ar^{++}(3s^{-1}3p^{-1})$ and $Ar^{++}(3p^{-3}3d)$ character. In particular, following the NIST atomic database, at large interatomic distances, the two configurations in the triplet state mix as 76% and 17%, respectively, while for the singlet state the weight ratio is 43% to 50%. Both PECs have minima at 3.2 Å, a shorter equilibrium internuclear distance compared to that of the neutral dimer which is 3.8 Å. Again, not all possible states stemming from the above mentioned mixed electronic configurations are depicted in 3.11. The PECs not shown have characters Σ_u^+, Π_g, and Π_u (singlet and triplet), and

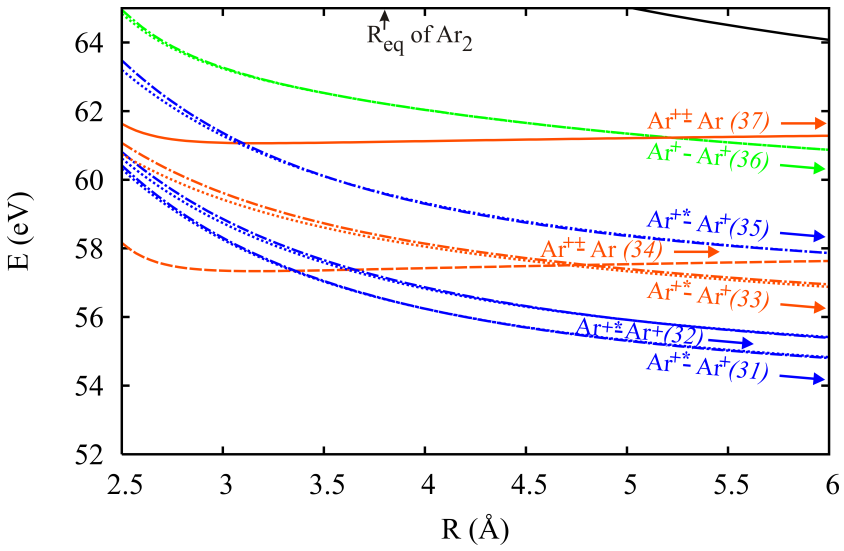

Figure 3.11: Computed potential energy curves of the doubly ionized argon dimer in the energy range 52 - 65 eV. The equilibrium internuclear distance of the neutral Ar_2 (3.80 Å) is marked by a vertical arrow. The blue, orange and green curves denote states of $3p^{-2}$, $3s^{-1}3p^{-1}$ and $3s^{-2}$ character, respectively. The black curve in the upper right corner is a triply ionized state. For further details see Table 3.5 and the text.

are nearly degenerate with those shown in the figure.

There are three types of repulsive Ar^+-Ar^+ curves in Fig. 3.11. The green ones correspond to $Ar^+(3s^{-1})$-$Ar^+(3s^{-1})$, while all the other curves are of satellite states - the blue ones of $Ar^+(3p^{-1})$-$Ar^+(3p^{-1})$ the orange ones of $Ar^+(3s^{-1})$-$Ar^+(3p^{-1})$. The group of black curves seen in the upper right corner of Fig. 3.11 are part of PECs residing at higher energies and will be discussed in the next subsection.

Ordered by increasing energy, the three groups of blue lines are assigned asymptotically to the electronic configurations $Ar^+(3p^{-2}(^1S)4s\ ^2S)$-$Ar^+(3p^{-1}\ ^2P)$, $Ar^+(3p^{-2}(^1D)4p\ ^2P)$-$Ar^+(3p^{-1}\ ^2P)$, and $Ar^+(3p^{-2}(^1S)4p\ ^2P)$-$Ar^+(3p^{-1}\ ^2P)$, respectively. The lower dotted and dashed-dotted blue curves correspond to $^3\Sigma_g^-$ and $^1\Delta_g$ states, the middle ones to $^3\Sigma_u^+$ and $^1\Delta_g$, and the upper ones to $^3\Sigma_u^+$ and $^1\Sigma_g^+$. For each of these groups there are PECs for the states with different symmetries than those presented. However, the calculated spectral intensities of these states for the whole range of interatomic distances are very low which does not allow the construction of reliable PECs out of our data.

The repulsive orange curves represent the PECs of a prominent correlation satellite of $Ar^+(3s^{-1})$-$Ar^+(3p^{-1})$, corresponding to $Ar^+(3p^{-2}(^1D)3d\ ^2S)$-$Ar^+(3p^{-1})$ at large internuclear separations. The dashed-dotted curve represents a $^1\Sigma_g^+$ state. For the triplet states we have chosen to draw the $^3\Sigma_g^+$. The other curves (not plotted in the figure) are: Σ_u^+,

Π_g, Π_u singlets and triplets, and are either degenerate with $^1\Sigma_g^+$ and $^3\Sigma_g^+$, or lie between them.

The last group of PECs depicted in Fig. 3.11 comprises two nearly degenerate green curves of two-site character, those of $Ar^+(3s^{-1}\ ^2S)$-$Ar^+(3s^{-1}\ ^2S)$. Once again, a dashed-dotted line is used for the singlet, $^1\Sigma_g^+$, and a dotted line for the triplet, $^3\Sigma_u^+$.

Let us now discuss the possible transitions between the states depicted in Fig. 3.11. All these states can, in principle, be populated by Auger decay. However, as we discussed, direct transitions to the two-site states have very low probability. Thus, in this energy region the most populated Auger final states will be the one-site satellite states of $Ar^{++}(3s^{-1}3p^{-1})$-Ar (the two orange attractive curves). The PECs of these states cross those of the excited two-site states $Ar^+(3p^{-2}(^1S)4s\ ^2S)$-$Ar^+(3p^{-1}\ ^2P)$, $Ar^+(3p^{-2}(^1D)4p\ ^2P)$-$Ar^+(3p^{-1}\ ^2P)$ and $Ar^+(3p^{-2}(^1S)4p\ ^2P)$-$Ar^+(3p^{-1}\ ^2P)$ (the blue repulsive curves) at R in the range 3.1 to 3.7 Å. CT relaxation pathways involving nuclear dynamics are thus conceivable and, in the language of wave-packet dynamics they can be described in the following way.

As the Auger decay itself is much faster than the nuclear dynamics, after the Auger decay has taken place, the nuclear wave packet will reside on the PECs of the one-site $Ar^{++}(3s^{-1}3p^{-1})$-Ar states and will be centered around the equilibrium internuclear distance of the neutral Ar_2, i.e. 3.8 Å. Then, the wave packet will start to propagate towards the minimum of the curves, located at 3.2 Å. At the points of curve crossing there can be, due to nonadiabatic coupling, a transfer of population to the purely repulsive curves describing the excited two-site states written in short as $Ar^+(3p^{-2}nl)$-$Ar^+(3p^{-1}\ ^2P)$. These charge transfer processes can be represented schematically as:

$$Ar^{++}(3s^{-1}3p^{-1})\text{-Ar} \longrightarrow Ar^+(3p^{-2}nl)\text{-}Ar^+(3p^{-1}\ ^2P),$$
$$E_{Ar^{++}(3s^{-1}3p^{-1})-Ar} = E_{Ar^+(3p^{-2}nl)} + E_{Ar^+(3p^{-1}\,^2P)} + \mathrm{KER},$$

where the latter equation gives the energy balance of the process. The crossing points of 3.1 to 3.7 Å correspond to KER values of 4.65 and 3.89 eV. See Ref. [22] for further discussion of these CT relaxation pathways.

For completeness we mention here two other possible CT channels, though less probable ones. As seen in Fig. 3.11, the PEC of the $Ar^{++}(3s^{-1}3p^{-1})$-Ar singlet one-site state (the upper attractive orange curve) also crosses the curves of the $Ar^+(3s^{-1})$-$Ar^+(3s^{-1})$ two-site states (the green repulsive curves) at 5.2 Å, and the PEC of the triplet one-site state (the lower attractive orange curve) crosses the curves of the two-site $Ar^+(3p^{-2}(^1D)3d\ ^2P)$-$Ar^+(3p^{-1}\ ^2P)$ satellite states (the repulsive orange curves) at 4.7 Å. These curve cross-

ings are located far from the initial position of the center of the wave packet and are not in the direction of its propagation. Correspondingly, we cannot expect them to play an important role. On the other hand, the wave packet is expected to be broad (all attractive PECs are very shallow) and some part of its right tail could reach the crossing points and, thus, some small fraction of it might decay to the two-site states.

An interesting feature of the PECs in the energy region discussed in this subsection is their strong interaction with states of the Rydberg series converging to the triply ionized argon dimer Ar^{++}-Ar^{+}. This series consists of the superposition of the $3p^{-1}nl$ series on one argon and the $3p^{-2}nl$ series on the other one, forming a quasicontinuum of PECs covering the whole energy region shown in Fig. 3.11. The coupling of the doubly ionized states to these Rydberg series causes a breakdown of the spectral lines in the double ionization spectrum into a bunch of satellites, a phenomenon related to the common breakdown of the molecular orbital picture of ionization [88]. This effect is particularly pronounced for the two-site satellite states of $Ar^{+}(3p^{-1})$-$Ar^{+}(3p^{-1})$ and $Ar^{+}(3s^{-1})$-$Ar^{+}(3p^{-1})$ (the blue and orange repulsive curves, respectively). The effect is naturally very weak at large internuclear separation R and increases as R decreases. The spectral lines for these two-site states begin to visibly breakdown into a multitude of lines at $R \sim 6$ Å. This is due to diffuse Rydberg orbitals which have a non-negligible overlap with the localized orbitals of the other argon. For ease of presentation, the PECs of Fig. 3.11 actually represent weighted averages of the energies of the components of the broken down spectral lines.

Energy range 64 to 77 eV

The PECs of doubly ionized states that have energies above the triple ionization threshold and can be subject to ICD following Auger are depicted in Fig. 3.12 together with the PECs of the final Ar^{++}-Ar^{+} states of the ICD.

There are four attractive dicationic PECs in the energy region of the figure. The one highest in energy (green curve) depicts the two degenerate $^1\Sigma_g^+$ and $^1\Sigma_u^+$ states of $Ar^{++}(3s^{-2})$-Ar. The minimum of the curve is located at 3.00 Å. The three bound orange curves originate from the satellite states of $Ar^{++}(3s^{-1}3p^{-1})$-Ar. The triplet (dashed) curve has a minimum at 4.25 Å, and correlates with the atomic state of Ar^{++} where the two configurations $3p^{-3}3d$ and $3s^{-1}3p^{-1}$ contribute in ratio of 60% to 22%.

The other two solid orange curves are two singlet one-site satellite PECs of $Ar^{++}(3s^{-1}3p^{-1})$-Ar, with minima at 4.00 Å and 3.65 Å for the lower and higher curve, respectively. Each of the singlets and triplets actually consist of four essentially degenerate states with symmetries Σ_g^+, Σ_u^+, Π_u and Π_g. It should be stressed here that the NIST atomic database reports

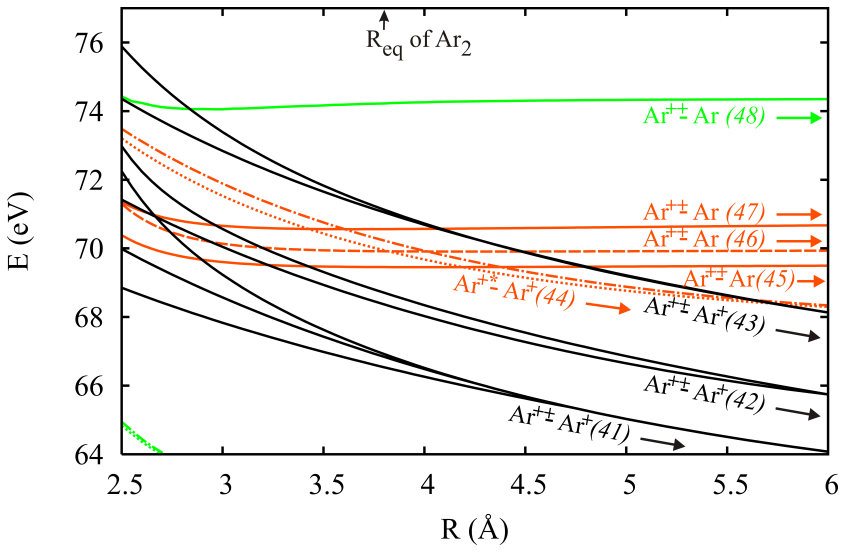

Figure 3.12: Computed potential energy curves of the doubly ionized argon dimer in the energy range 64 - 77 eV. The equilibrium internuclear distance of the neutral Ar_2 (3.80 Å) is marked by a vertical arrow. The orange and green curves denote states of $3s^{-1}3p^{-1}$ and $3s^{-2}$ character, respectively, while the black curves are triply ionized states. For further details see Table 3.5 and the text.

only one Ar^{++} singlet ^{1}P state in which the two configurations $3p^{-3}3d$ and $3s^{-1}3p^{-1}$ contribute by 48% and 37%, respectively. This correlates with the higher in energy PEC in Fig. 3.12. Our computations on the isolated argon atom show that only if we use a basis set as small as cc-pVDZ we find a single singlet state. If larger and better basis sets are used, the second singlet state constantly appears in the spectrum. We note, however, that there is another singlet state of Ar^{++} in the NIST database which energetically correlates well with the lower in energy PEC in Fig. 3.12. In the database it is attributed to a mixture of the $3p^{-3}(^2\mathrm{P})4s$ ^{1}P and $3p^{-3}(^2\mathrm{D})3d$ ^{1}P configurations. We cannot rule out that this state is related to our second singlet state, as our eigenvectors have also some contribution from the $3p^{-3}(^2\mathrm{P})4s$ ^{1}P configuration (which are, however, weak).

The potential energy curves of the final tricationic states of the ICD process are depicted with solid black lines. They can be divided into three groups according to their behavior at asymptotic distances. In particular, what differentiates them is the electronic state of the Ar^{++} $3p^{-2}$ fragment, ^{3}P, ^{1}D and ^{1}S in order of increasing energy, while the Ar^+ fragment is in its $3p^{-1}$ ^{2}P ground state. The lowest in energy $Ar^{++}(3p^{-2}$ ^{3}P)-$Ar^+(3p^{-1}$ ^{2}P) group contains curves with symmetries Σ_g^+, Σ_g^-, Σ_u^+, Σ_u^-, Δ_g, Δ_u, Π_u, and Π_g, both doublets and quartets. Only the $^4\Delta_g$, $^2\Sigma_g^+$, and $^4\Sigma_g^-$ PECs which cover the whole span of energies of this group are shown. The set of $Ar^{++}(3p^{-2}$ ^{1}D)-$Ar^+(3p^{-1}$ ^{2}P) curves, at

intermediate energy, consists of doublets only: $^2\Sigma_g^+$, $^2\Sigma_g^-$, $^2\Sigma_u^+$, $^2\Sigma_u^-$, $^2\Delta_g$, $^2\Delta_u$, $^2\Pi_u$, and $^2\Pi_g$. They lie in the energy band enclosed by the PECs with characters $^2\Sigma_g^+$ and $^2\Delta_g$ depicted explicitly in the figure. Finally, the highest in energy $Ar^{++}(3p^{-2}\ ^1S)$-$Ar^+(3p^{-1}\ ^2P)$ group has only four members of $^2\Sigma_g^+$, $^2\Sigma_u^-$, $^2\Pi_g$, and $^2\Pi_u$ symmetry, forming an energy band enclosed by the depicted $^2\Sigma_g^+$ and $^2\Sigma_u^-$ curves.

In Fig. 3.12 we also see two orange repulsive curves, representing $^1\Sigma_g^+$ (dashed-dotted) and $^3\Sigma_g^+$ (dotted) two-site satellite states of $Ar^+(3s^{-1})$-$Ar^+(3p^{-1})$. The PECs of the other (not shown) singlet and triplet Σ_u^+, Π_u, and Π_g states lie within the energy band enclosed by the two PECs shown. All these PECs dissociate to two Ar^+ ions, one in the ^2S ($3s^{-1}3p^{-1}(^3P)4p$) state and the other in the ^2P ($3p^{-1}$) ground state.

The energy of $Ar^+(3s^{-1}3p^{-1}(^3P)4p\ ^2S)$ is 49.98 eV [79], about 7 eV higher than that of the ground state of Ar^{++} and also higher than its ^1D excited state. Hence, it can autoionize to $Ar^{++}(3p^{-2}\ ^3P$ or $^1D)$. For the dimer, the following intra-atomic decay process thus becomes possible:

$$Ar^+(3s^{-1}3p^{-1}(^3P)4p^2S)\text{-}Ar^+(3p^{-1}\ ^2P) \longrightarrow Ar^{++}(3p^{-2}\ ^3P \text{ or } ^1D) + Ar^+(3p^{-1}\ ^2P) + e^-_{auto}.$$

That this decay by autoionization may in principle take place is also clear from Fig. 3.12, where the repulsive dicationic curves are seen to lie well above the two lowest lying triply ionized PECs. In addition, the repulsive PECs of the two-site satellite states of $Ar^+(3s^{-1})$-$Ar^+(3p^{-1})$ cross the bound ones of the one-site dicationic satellite states of $Ar^{++}(3s^{-1}3p^{-1})$-Ar at $R \sim 3.5$ - 4.5 Å (recall that the equilibrium distance of Ar_2 is 3.8 Å) and, furthermore, they also cross the highest energy group of tricationic states at around 5.7 Å. Thus, the two-site satellite states of $Ar^+(3s^{-1})$-$Ar^+(3p^{-1})$ can serve as an intermediate in the decay of the Auger populated one-site satellite states of $Ar^{++}(3s^{-1}3p^{-1})$-Ar to the triply ionized dimer. The KER of the Ar^{++} and Ar^+ ions in this process should be around 5 eV and the emitted electron is expected to have very low kinetic energy.

Examining now the PECs of the bound states in Fig. 3.12, we see that both the $3s^{-2}$ green one and the $3s^{-1}3p^{-1}$ satellites (orange) can decay to the triply ionized dimer. Let us first concentrate on the one-site satellite states of $Ar^{++}(3s^{-1}3p^{-1})$-Ar (the solid and the dashed orange curves in Fig. 3.12). As was already briefly discussed in Sec. 3.2.1, these states decay via fast nonradiative process to Ar^{++}-Ar^+, i.e. they are subject to ICD. Considering the curves of the final states of the tricationic cluster, both the lower (leading to $Ar^{++}\ ^3P$) and the middle (leading to $Ar^{++}\ ^1D$) groups provide accessible final states for the ICD. In this process an electron from the $3p$ level of the doubly ionized argon fills the hole in its $3s$ level releasing enough energy to ionize the second Ar atom

Table 3.6: Electronic states of Ar_2^{++} which undergo ICD, the corresponding final states of Ar_2^{3+} and energies of the ICD electron (in eV).

Before ICD → After ICD ↓	$Ar^{++}(3p^{-3}(^2D)3d\ ^1P$ $(+3s^{-1}3p^{-1}))$-Ar	$Ar^{++}(3p^{-3}(^2D)3d\ ^3P$ $(+3s^{-1}3p^{-1}))$-Ar	$Ar^{++}(3p^{-3}(^2D)3d\ ^1P$ $(+3s^{-1}3p^{-1}))$-Ar	$Ar^{++}(3s^{-2}\ ^1S)$-Ar
$Ar^{++}(3p^{-2}\ ^1S)$- $Ar^+(3p^{-1}\ ^2P)$	–[1]	–[1]	–[1]	3.17 - 3.10
$Ar^{++}(3p^{-2}\ ^1D)$- $Ar^+(3p^{-1}\ ^2P)$	1.09 - 0.75	1.55 - 1.21	2.19 - 1.85	5.86 - 5.52
$Ar^{++}(3p^{-2}\ ^3P)$- $Ar^+(3p^{-1}\ ^2P)$	2.92 - 2.53	3.38 - 2.99	4.02 - 3.64	7.69 - 7.30

[1]Decay channel is closed.

in the system. The energy of the emitted (ICD) electron is equal to the difference in energy of the initial and final states of the system. The kinetic energy of the two argon ions is equal to that determined by the Coulomb repulsion of a single and a double point charge separated by the distance of the two argon atoms. As the Auger decay and the following ICD are much faster than the nuclear motion in the dimer, the bond length of the system does not change much during the cascade process (Auger followed by ICD) and stays similar to that in Ar_2, i.e. $\sim$3.8 Å. Thus, the KER of the two fragments Ar^{++} and Ar^+ is approximately 7.6 eV. This process was observed in the experiments made by Morishita *et al.* [21] and can be written in short as:

$$Ar^{++}(3p^{-3}(^2D)3d(+3s^{-1}3p^{-1}))\text{-}Ar \longrightarrow Ar^{++}(3p^{-2}) + Ar^{+}(3p^{-1}) + e^-_{ICD}.$$

The energy balance of the process is:

$$E_{Ar^{++}(3p^{-3}3d(+3s^{-1}3p^{-1}))-Ar} = E_{Ar^{++}(3p^{-2})} + E_{Ar^{+}(3p^{-1})} + E_{e^-_{ICD}} + \text{KER}.$$

The energy of the ICD electron, $E_{e^-_{ICD}}$, is given as the difference in energy between the bound PECs of Ar^{++}-Ar and those of the final states Ar^{++}-Ar^+ at 3.8 Å. The electronic configurations of the dimers undergoing ICD, their final states, and the corresponding energies for the ICD electrons are summarized in Table 3.6.

The upper group of curves of the triply ionized dimer lies above the orange one-site dicationic PECs, crossing them at large distances. Therefore, it can serve only as a final state of the electronic decay from the uppermost (green) dicationic states – $Ar^{++}(3s^{-2})$-Ar. Note that the energies of the ICD electrons in these transitions (3.17 - 3.10 eV) are comparable to those originating from the decay of the $3s^{-1}3p^{-1}$ one-site states. Again, we can expect the KER from this ICD process to correspond to an internuclear distance

of 3.8 Å. The process can be written in short as:

$$\mathrm{Ar}^{++}(3s^{-2})\text{-Ar} \longrightarrow \mathrm{Ar}^{++}(3p^{-2}) + \mathrm{Ar}^{+}(3p^{-1}) + e^{-}_{ICD},$$

with energy balance:

$$E_{Ar^{++}(3s^{-2})-Ar} = E_{Ar^{++}(3p^{-2})} + E_{Ar^{+}(3p^{-1})} + E_{e^{-}_{ICD}} + \mathrm{KER}.$$

This type of ICD process is expected to be less probable, since it involves three electrons – two $3p$ electrons have to fill the two $3s$ holes in one of the argons ejecting one $3p$ electron from the other argon. However, a three electron ICD was observed in the heteronuclear cluster NeAr [89].

The states of $\mathrm{Ar}^{++}(3s^{-2})$-Ar can, of course, decay also to the tricationic states lying lower in energy (the middle and lower groups of black repulsive curves in Fig. 3.12). In these processes the energy of the ICD electron is expected to be 5.86 eV and 7.69 eV, respectively. These transitions could not be resolved in the experiments of Ref. [21], due to the energy overlap of these ICD electrons with the photoelectrons coming from the core ionization. In subsequent experiments by the group of Ueda [78], these ICD channels were observed as very low intensity peaks in the electron spectra, confirming their low probability.

Processes of relaxation of the doubly charged systems Ar^{++}-Ar into Ar^{++}-Ar^{+} that involve electron transfer cannot be excluded in this energy region, yet these are going to be much slower compared to the energy transfer in ICD.

3.3 Influence of the nuclear dynamics on the ICD of NeAr

The heteronuclear system NeAr can be used to illustrate the time evolution of the ICD electron spectrum and the effects of the lifetime of the decaying state on its shape, as shown in Ref. [90]. There, the electronic decay of $\mathrm{Ne}^{++}(2s^{-1}2p^{-1})\mathrm{Ar}$ have been computed within the framework of the time-dependent theory of wave packet propagation.

We will first give a general overview of electronic states of the system by means of a simple model for the PECs of the relevant states. The energy diagram of the relevant doubly and triply ionized states of NeAr is depicted in Fig. 3.13. The PECs of the bound doubly ionized $\mathrm{Ne}^{++}\mathrm{Ar}$ and NeAr^{++} states are represented in the diagram by

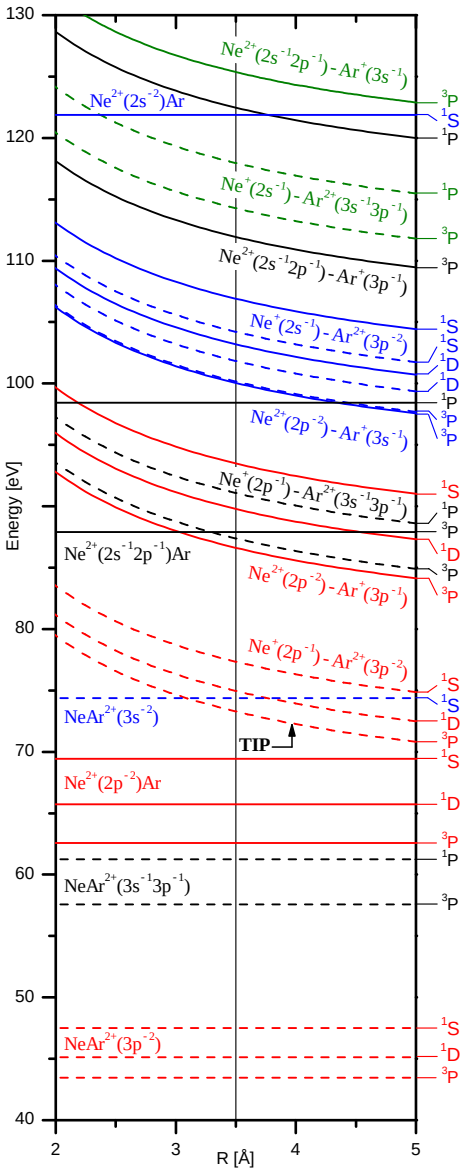

Figure 3.13: Energy diagram of NeAr. Solid and dashed horizontal lines: model PECs of bound doubly ionized $Ne^{++}Ar$ and $NeAr^{++}$ states, respectively. Solid and dashed 2 / R lines: model PECs of repulsive triply ionized $Ne^{++}Ar^{+}$ and $Ne^{+}Ar^{++}$ states, respectively. Asymptotic limits are calibrated to the NIST data [3]. The ground state equilibrium distance of NeAr is indicated at 3.5 Å by the vertical line. For further details see the text, as well as Ref. [90].

solid and dashed horizontal lines, respectively. These states can be populated if Auger decay takes place in NeAr at the equilibrium internuclear distance of the ground state (3.5 Å) indicated in the diagram by the vertical line. The Coulomb repulsion between two ionic fragments of the two-site triply ionized states of the system determines the 2 / R asymptotic behavior of the corresponding PEC. The repulsive Ne^{++}-Ar^{+} and Ne^{+}-Ar^{++} states are shown in the figure by analytical solid and dashed 2 / R curves, respectively. The energy positions of all PECs are calibrated at infinite internuclear distance to the sum of energies of the atomic fragments taken from NIST spectroscopic tables [3]. As can be seen from the figure, the presence of two different atoms, has increased the number of dicationic and tricationic states in comparison with the investigated above homonuclear

species. Therefore, number of possible relaxation pathways is also greater.

Let us consider the de-excitation modes of the $Ne^{++}Ar$ shown in Fig. 3.13. The model PECs of the $Ne^{++}(2p^{-2}\ ^3P,\ ^1D,\ ^1S)Ar$ states are depicted by three solid horizontal red lines between 62 and 70 eV. They are energetically below the triply ionized states and are, therefore, electronically stable. The first $Ne^{++}Ar$ state that is above the triple ionization threshold and can decay by electron emission, is $Ne^{++}(2s^{-1}2p^{-1}\ ^3P)Ar$ - the lowest solid horizontal black line at 87.89 eV . Three ETMD channels of this state, to $Ne^{+}(2p^{-1})Ar^{++}(3p^{-2}\ ^3P,\ ^1D,\ ^1S)$ shown by the three dashed repulsive red curves are energetically open at all internuclear distances, while the dICD to the $Ne^{++}(2p^{-2}\ ^3P)Ar^{+}(3p^{-1})$, i.e. lowest solid repulsive red curve is open from about 3.1 Å. Finally, at distances larger than 3.4 Å the ETMD of $Ne^{++}(2s^{-1}2p^{-1}\ ^3P)Ar$ can lead to the formation of $Ne^{+}(2p^{-1})Ar^{++}(3s^{-1}3p^{-1}\ ^3P)$ - the lowest dashed repulsive black curve.

The higher in energy $Ne^{++}(2s^{-1}2p^{-1}\ ^1P)Ar$ - the uppermost solid horizontal black line at 98.42 eV is electronically unstable and has many possible deexcitation pathways. Among them are the ETMDs to $Ne^{+}(2p^{-1})Ar^{++}(3p^{-2}\ ^3P,\ ^1D,\ ^1S)$, as well as to $Ne^{+}(2p^{-1})Ar^{++}(3s^{-1}3p^{-1}\ ^3P,\ ^1P)$, i.e. the dashed repulsive black curves, which are open at all internuclear distances. Similar to the triplet state, $Ne^{++}(2s^{-1}2p^{-1}\ ^1P)Ar$ can also undergo ICD transitions to the $Ne^{++}(2p^{-2}\ ^3P,\ ^1D,\ ^1S)Ar^{+}(3p^{-1})$ states, the three solid repulsive red curves. The transition to $Ne^{++}(2p^{-2}\ ^3P)Ar^{+}(3p^{-1})$ is an exchange ICD due to the flip of the total spin of the one-site two-hole state of the Ne^{++} fragment from singlet to triplet. The two transitions to $Ne^{++}(2p^{-2}\ ^1D)Ar^{+}(3p^{-1})$ and $Ne^{++}(2p^{-2}\ ^1S)Ar^{+}(3p^{-1})$ are obviously dICDs. One can see from Fig. 3.13 that the dICD of $Ne^{++}(2s^{-1}2p^{-1}\ ^1P)Ar$ to $Ne^{++}(2p^{-2}\ ^1D)Ar^{+}(3p^{-1})$ is energetically open in the whole R range, whereas the dICD to $Ne^{++}(2p^{-2}\ ^1S)Ar^{+}(3p^{-1})$ is possible only at internuclear distances larger than 2.2 Å.

The uppermost one-site doubly ionized state $Ne^{++}(2s^{-2}\ ^1S)Ar$, shown by the solid horizontal blue line at 121.89 eV, is also electronically unstable. Although its energy is higher than that of many two-site triply ionized states, we emphasize that the dICD transition from this state is highly improbable for the following reasons. The only possible dICD of this state is the transition to $Ne^{++}(2s^{-1}2p^{-1}\ ^1P)Ar^{+}(3p^{-1})$ - the uppermost solid repulsive black curve. This transition is energetically open only at large internuclear distances, 3.8 Å or more. Thus, being created around 3.5 Å, the nuclear wave packet starts to propagate toward smaller internuclear distances because the minimum of the corresponding dicationic PEC is known to be shifted to smaller R than that of the ground state, due to polarization effects. The ICD transition rate falls off at large internuclear

distances as R^{-6} and is small for large R. Therefore, the relative intensity for the process must be very low, and only a weak trace of this transition is expected to be observed in experiments at around zero ICD electron energy. Despite this, $Ne^{++}(2s^{-2}\ ^1S)Ar$ can release its excess energy via: (i) ETMD to $Ne^{+}(2s^{-1})Ar^{++}(3p^{-2}\ ^3P,\ ^1D,\ ^1S)$ - the dashed repulsive blue curves, (ii) ETMD to $Ne^{+}(2s^{-1})Ar^{++}(3s^{-1}3p^{-1}\ ^1P,\ ^3P)$ - dashed repulsive green curves, and (iii) eICD to $Ne^{++}(2s^{-1}2p^{-1}\ ^3P)Ar^{+}(3p^{-1})$ - the lowest solid repulsive black curve. Three-electron ICD transitions of $Ne^{++}(2s^{-2}\ ^1S)Ar$ are also possible to $Ne^{++}(2p^{-2})Ar^{+}(3p^{-1})$ and $Ne^{++}(2p^{-2})Ar^{+}(3s^{-1})$ and are confirmed by the experiment [89]. Three electron ETMD to $Ne^{+}(2p^{-1})Ar^{++}(3p^{-2})$ and $Ne^{+}(2p^{-1})Ar^{++}(3s^{-1}3p^{-1})$ is also feasible. Since many electronic decays of the $Ne^{++}Ar$ states are energetically allowed, one can neglect the possible one-site atomic radiative decays of these states the radiative transitions are typically orders of magnitude slower.

In order to complete the present analysis we will now briefly discuss the $NeAr^{++}$ states. As seen from the energy diagram (Fig. 3.13), the model PECs of $NeAr^{++}(3p^{-2}\ ^3P,\ ^1D,\ ^1S)$ - the three dashed horizontal red lines between 43 and 48 eV, as well as the model PECs of the $NeAr^{++}(3s^{-1}3p^{-1}\ ^3P,\ ^1P)$ - two dashed horizontal black lines between 57 and 62 eV, are energetically below the TIP and are therefore electronically stable. One-site radiative decay of the $NeAr^{++}(3s^{-1}3p^{-1})$ states to the $NeAr^{++}(3p^{-2})$ ones is, however, possible. Electronic decay of $NeAr^{++}(3s^{-2}\ ^1S)$ (the dashed horizontal blue line at 74.36 eV) to $Ne^{+}(2p^{-1})Ar^{++}(3p^{-2}\ ^3P)$ - the lowest dashed repulsive red curves is open at internuclear distances larger than 3 Å. This weak decay channels involve, however, three-electron transition matrix elements and compete with the one-site radiative decay to $NeAr^{++}(3s^{-1}3p^{-1})$.

One can expect that the dICDs of the $Ne^{++}(2s^{-1}2p^{-1}\ ^1P,\ ^3P)Ar$ states discussed above are the most probable de-excitation pathways of these states. A more accurate interpretation of these electronic transitions requires precise PECs, corresponding decay rates, and the accurate treatment of the underlying nuclear dynamics.

Our study continues with the dICD of $Ne^{++}(2s^{-1}2p^{-1}\ ^3P)Ar$, since this electronic state can be very well populated by the Auger decay of the neon atom (see Table 3.1) and its decay is influenced the most by the nuclear dynamics of the system. The process can be written in short as:

$$Ne^{++}(2s^{-1}2p^{-1}\ ^3P)\text{-}Ar \longrightarrow Ne^{++}(2p^{-2}\ ^3P) + Ar^{+}(3p^{-1}) + e^{-}_{ICD}.$$

The time evolution of the partial ICD spectrum computed for this transition is depicted in Fig. 3.14(a). The symmetric maximum centered around the vertical transition energy

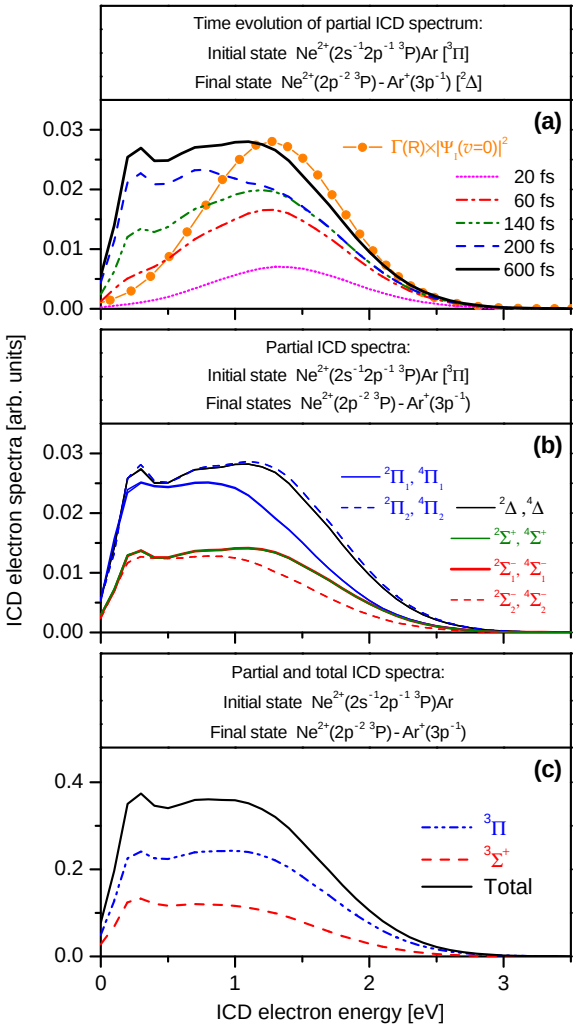

Figure 3.14: Computed partial and total ICD spectra for the transition between the $Ne^{++}(2s^{-1}2p^{-1}\ ^3P)Ar$ and $Ne^{++}(2p^{-2}\ ^3P)Ar^+(3p^{-1})$ states. Panel (a): Time evolution of the partial spectrum for the transition between the $^3\Pi$ initial and $^2\Delta$ final states. Panel (b): Partial spectra for the decay of the $^3\Pi$ initial state into a manifolds of final doublet and quartet states. The symmetries of all 12 final states are indicated in the legend (see also description in text). Panel (c): Total spectrum and partial spectra of the decay of the $^3\Pi$ and $^3\Sigma^+$ initial $Ne^{++}(2s^{-1}2p^{-1}\ ^3P)Ar$ states. For further details see Ref. [90].

of about 1.3 eV is the first to develop. After its creation close to the right turning point of the PEC of the initial ICD state, the intermediate wave packet starts to propagate toward smaller internuclear distances. As intermediate wave packet reaches the left turning point after about 125 fs, the low energy region of the spectrum starts to develop. A clearly demonstrating an asymmetry already at 140 fs. After about 250 fs the intermediate wave packet has done a complete vibrational cycle and, because of decay, its norm is reduced by a factor of about 50. The spectrum converges to its final form after about 600 fs, when the decay of the intermediate wave packet is essentially complete.

In order to simulate an instantaneous ICD transition, a mirror reflection image of the initial wave packet is also shown in Fig. 3.14(a) by the orange line with solid circles. The Gaussian-like shape of the spectrum has a maximum at the energy equal to that of the vertical transition between the computed in Ref. [90] PECs of the initial and the final state. In fact, in the case of the dICD of $Ne^{++}(2s^{-1}2p^{-1}\ ^1P)Ar$ this shape of the electron

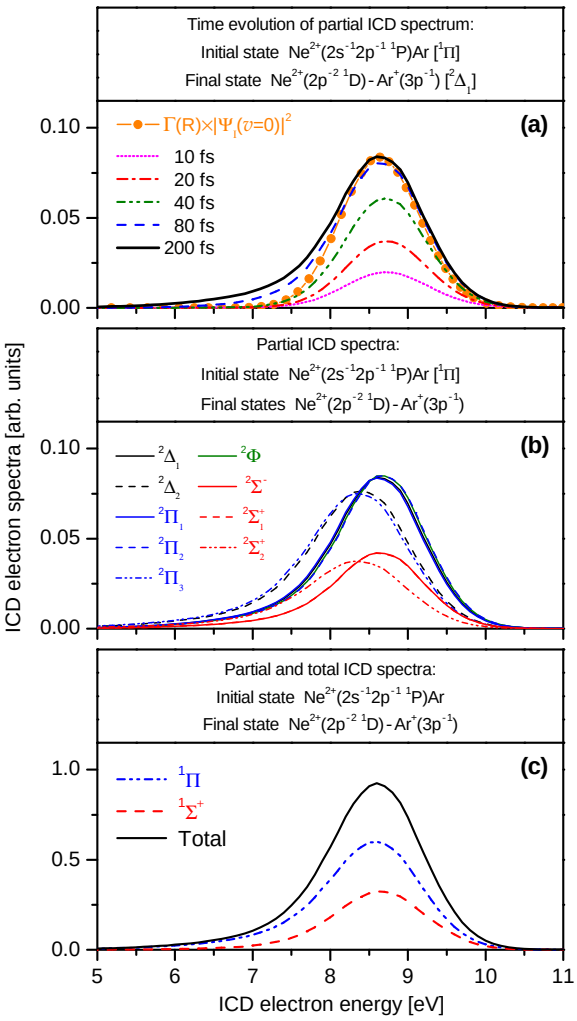

Figure 3.15: Computed partial and total ICD spectra for the transition between the $Ne^{++}(2s^{-1}2p^{-1}\ ^1P)Ar$ and $Ne^{++}(2p^{-2}\ ^1D)Ar^+(3p^{-1})$ states. Panel (a): Time evolution of the partial spectrum for the transition between the $^1\Pi$ initial and $^2\Delta$ final states. A mirror reflection of the initial wave packet $|\Psi_i(v=0)|^2$ on the final PEC is shown by circles in order to simulate an instantaneous decay with a transition ICD rate estimated as R^{-6}. Panel (b): Partial spectra for the decay of the $^1\Pi$ initial state into a manifolds of final doublet and quartet states. The symmetries of all 12 final states are indicated in the legend (see also description in text). Panel (c): Total spectrum and partial spectra of the decay of the $^1\Pi$ and $^1\Sigma^+$ initial $Ne^{++}(2s^{-1}2p^{-1}\ ^1P)Ar$ states. For further details see Ref. [90].

spectrum is preserved throughout the process (Fig. 3.15), i.e. the almost instantaneous decay there is very slightly affected by the time evolution of the system.

Looking at the converged result for the partial decay spectum of $Ne^{++}(2s^{-1}2p^{-1}\ ^3P)Ar$ in Fig. 3.14(a), it becomes obvious that the nuclear dynamics considerably influences the relaxation pathway. The resulting spectrum is considerably broader than the model one for instantaneous ICD. In addition, it exhibits a distinct asymmetry, with a shoulder on the low electron energy side. This shoulder and the asymmetry grow as time proceeds see Fig. 3.14(a) and are clear signatures of nuclear dynamics. In an instantaneous ICD there is no time for the nuclei to move and, consequently, the observed asymmetry and shoulder do not appear. The total ICD electron spectrum computed for the relaxation of is shown in 3.14(c) by a solid line, it form is very close to that of the discussed channel.

3.4 Conclusions

The noble gas clusters and their dimers are suitable systems for the study of ICD. This comes as a result of their comparatively simple geometry and electronic structure. Thus, they have been the first objects of both theoretical and experimental investigation. The electronic decay modes of doubly ionized and excited states of Ar_2 produced via Auger decay were also the first to be experimentally observed. Later, experimental works show the abundance of ICD and related to it phenomena in argon, neon, krypton [91] and mixed clusters of various sizes. However, some of the obtained results needed a better interpretation which can be achieved with the help of the theory.

Therefore, the different ionic states of the neon dimer and their relaxation pathways were investigated. For this purpose, elaborated ab initio methods were used to calculate the potential energy curves of the core ionized system $Ne^+(1s^{-1})$-Ne, of different one- and two-site dicationic states, as well as of all the two-site tricationic states with holes in the $2p$ and $2s$ levels. To the best of our knowledge these PECs have not been discussed in the literature until now. The computed potential curves were then used to explain various interatomic decay processes initiated by the Auger decay of $Ne^+(1s^{-1})$-Ne.

The interatomic Coulombic decay following the Auger process was analyzed examining the charged states of Ne_2 involved in the two step relaxation. This cascade phenomenon was theoretically predicted a few years ago [20] and was recently confirmed experimentally [24]. Contrary to the previously studied ICD following Auger decay in Ar_2 [21, 68], in the case of neon dimer one can clearly distinguish different types of interatomic decay mechanisms, namely the direct ICD, exchange ICD, and ETMD.

There is one open channel for the efficient direct ICD from a state populated by the Auger decay. It is from the $Ne^{++}(2p^{-1}2s^{-1}\ ^1P)$-Ne state. Less efficient and operating mainly at distances smaller than the equilibrium one, the exchange ICD and ETMD, are nonetheless also possible for this state. The other main electronic state of the neon dimer which can undergo interatomic decay is $Ne^{++}(2s^{-2}\ ^1S)$-Ne. The direct ICD process here would need a spin-flip, a process with so low probability that this channel can be regarded as closed. However, exchange ICD or ETMD to different final states can take place. Another possibility for decay of this states is the three-electron ICD process where two $2p$ electrons fill the two holes in the $2s$ initial vacancies and a $2p$ electron from the neighboring neon atom is emitted. Compared to the other interatomic decay mechanisms this three-electron process should produce electrons of much higher energy ($\approx$ 25-29 eV). However, these type of processes are expected to be less efficient than the competing exchange ICD and ETMD.

The one-site dicationic states with two vacancies in the $2p$ shell lie below the triple ionization threshold and cannot further decay by electron emission. Nevertheless, they can relax via radiative charge transfer to the two-site dicationic states of the type $Ne^+(2p^{-1})$-$Ne^+(2p^{-1})$ that subsequently undergo Coulomb explosion.

Charge transfer at the points of curve crossing is also feasible for the triply ionized states of the dimer $Ne^{3+}(2p^{-3})$-Ne, which can be populated by a double Auger process or photo ionization. The double Auger decay represents about 8% of the total decay rate of the neon 1s vacancy.

The results of our calculations show that despite its seeming simplicity the neon dimer is lavish in interesting physical phenomena and provides the opportunity for studying various kinds of ultrafast and fast interatomic mechanisms.

The potential energy curves presented in Section 3.1.1 were also used in a computation accounting for the nuclear dynamics of the system. The total and partial ICD electron spectra were computed within the framework of the time-dependent theory of wave packet propagation [65]. Thereby, the impact of nuclear dynamics accompanying the electronic decay on the computed ICD-electron spectra was investigated in detail.

The possibility of ICD following Auger decay in the argon dimer was also investigated. We have calculated in our study, the potential energy curves of the core ionized system $Ar^+(2p^{-1})$-Ar, of different one- and two-site dicationic states, as well as of the lowest two-site tricationic states. To the best of our knowledge, except for the dicationic states with two holes in the $3p$ level [81–83], these PECs have not been discussed in the literature until now. The calculated potential curves are used to explain various possible relaxation pathways initiated by the Auger decay of $Ar^+(2p^{-1})$-Ar.

As was theoretically predicted [20] and later studied experimentally [21, 78], an Auger decay can be followed by ICD in a weakly bound system. In the argon dimer this cascade process is possible if the final dicationic Auger states have energies above the triple ionization threshold ($\sim$67 eV). Although the main $Ar^{++}(3p^{-1}3s^{-1})$-Ar states are below the triple ionization threshold, one-site satellite states originating by admixture with $3p^{-3}3d$ configurations are above it and can thus decay by ICD. Another open channel for ICD is the state $Ar^{++}(3s^{-2}\ {}^1S)$-Ar. However, the ICD from this state is a three-electron process (two $3p$ electrons fill the two holes in the $3s$ atomic orbital and a $3p$ electron from the neighboring argon atom is emitted) and is, hence, less efficient.

The PECs of those electronic states of Ar_2^{++}, which do not participate in an ICD but can be formed as a result of the Auger decay, are used to study other relaxation processes involving one- and two-site doubly ionized argon clusters. Three types of relaxation

pathways other than that can be observed. In the low energy region, 32 - 52 eV, one can expect a radiative charge transfer process between the $Ar^{++}(3p^{-2})$-Ar and $Ar^{+}(3p^{-1})$-$Ar^{+}(3p^{-1})$ states. Experimental proof of this process can be found in Ref. [67]. In the higher energy regions there are several open channels for nonadiabatic CT processes due to curve crossings, i.e. processes involving nuclear dynamics. These are, e.g., the transitions from the one-site satellite states of $Ar^{++}(3s^{-1}3p^{-1})$-Ar to the excited two-site states of $Ar^{+}(3p^{-2}nl)$-$Ar^{+}(3p^{-1})$ in the energy region 52 - 65 eV. Finally, the two-site state $Ar^{+}(3s^{-1}3p^{-1}(^{3}P)4p\ ^{2}S)$-$Ar^{+}(3p^{-1})$ can undergo an intra-atomic decay process, by autoionizing to $Ar^{++}(3p^{-2})$-$Ar^{+}(3p^{-1})$. We also mention that decay processes of Ar^{++}-Ar to Ar^{++}-Ar^{+} that involve nonadiabatic electron transfer are also possible in the energy region where ICD is operative, but are expected to have a negligible effect.

In a study of the effects of the nuclear dynamics on the shape of the ICD electron spectum of doubly ionized states of NeAr, it was shown that the mirror reflection image of the initial wave packet relates well to the almost instantaneous dICD of $Ne^{++}(2s^{-1}2p^{-1}\ ^{1}P)$Ar. In the case of the decay of the triplet state with the same electron configuration, the nuclear dynamics considerably influences the process. The resulting spectrum is considerably broader than the model one for instantaneous relaxation and exhibits a distinct asymmetry with a shoulder on the low electron energy side.

Cascade decay processes like those studied in diatomic species exist in larger systems, as well. The sequential interatomic decay, where the first step is an Auger decay with interatomic character and the second step is a ICD, was identified in argon trimers [22]. Electron-ion-ion-ion coincidence spectroscopy in which the kinetic energy of the slow ICD electron and the kinetic energy release among the three Ar^{+} ions are measured in coincidence. There, the $2p$ hole state in Ar_3 decays to the one-site two-hole states $Ar^{++}(3s^{-1}3p^{-1})$-Ar-Ar that couples to the two-site satellite states $Ar^{+}(3p^{-2}nl)$-$Ar^{+}(3p^{-1})$-Ar. These states are subject to ICD and relax to $Ar^{+}(3p^{-1})$-$Ar^{+}(3p^{-1})$-$Ar^{+}(3p^{-1})$, as the nl electron fills the $3p$ hole in the same Ar site and one of the $3p$ electrons in the third Ar site is emitted as a slow e^{-}_{ICD}.

Chapter 4

Relaxation processes in small biochemically relevant hydrogen bonded systems

The ICD can be initiated by a removal of an electron from the inner-valence shell of a molecule belonging to a biological structure. In this case, the two positive ions that are formed in the process would not only break the bond between them. These free radicals are highly reactive [92, 93] and they, as well as the low energy electrons (LEE) [94, 95] accompanying the decay, can cause a severe damage to any biological system that interacts with them.

Being orders of magnitude faster than the photon emission or the relaxation processes involving nuclear dynamics, the electronic decay modes will be the dominant ones in larger structure, as well. In principle, the ICD can be outperformed by the auto-ionization of the initially created electronic state when the latter is energetically allowed. Therefore, if an inner-valence ionized molecule cannot autoionize, but has neighbors, like in a hydrogen bonded cluster, the system is a prime candidate for ICD [8,10,11,14,15]. Weak interactions of these kinds are typical in biochemistry and the ICD is likely to happen in living tissues containing hydrogen bonded macromolecules.

In what follows, we shall discuss the ICD in small bimolecular systems that contain an oxygen atom as a proton donor or as a proton acceptor. These systems represent the most common types of hydrogen bonding between water and biochemically relevant molecules. We shall later see that the ionization of the inner-valence shell of H_2O triggers ICD in all of the studied species. This result is of great importance, as H_2O makes up more than 70% of the weight of most living organisms. Thus, if a biological object is exposed to an

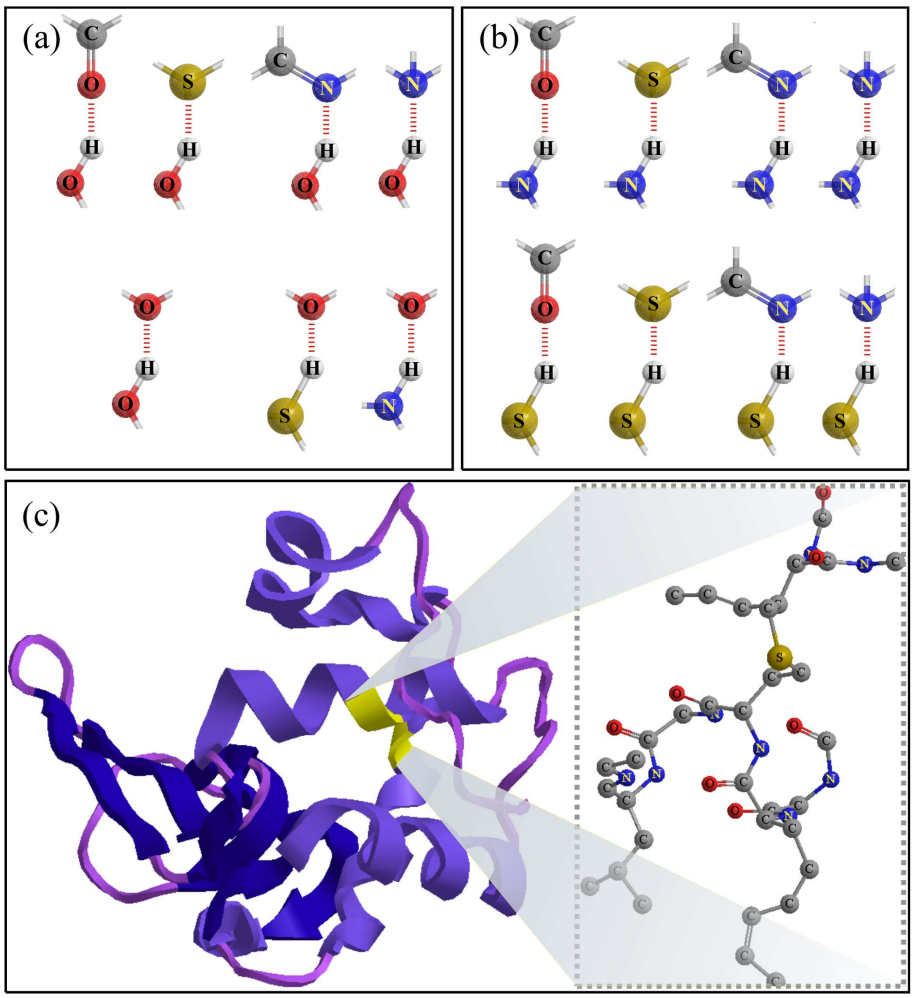

Figure 4.1: The H, C, N, O, and S containing molecular fragments and types of hydrogen bonding (panels (a) and (b)) that are common for the studied $H_2O\cdots HCHO$, $H_2O\cdots H_2CNH$, $H_2O\cdots NH_3$, $NH_3\cdots H_2O$, $H_2O\cdots H_2S$, $H_2S\cdots H_2O$, and $H_2O\cdots H_2O$ (p-donor$\cdots$ p-acceptor), as well as for biochemical systems like the enzyme lysozyme (panel (c)). For further details see the text.

ionizing radiation, the water that it contains will absorb most of it.

As this is the first study of ICD in such systems, we shall not investigate hydrogen bonded macromolecules, but rather use a set of simple compounds. Since four chemical elements (hydrogen, carbon, nitrogen, and oxygen) make up more than 99% of the mass of most cells, the majority of hydrogen bonds of even the most sophisticated biological system will contain them [96]. By adding sulfur to compare with its weaker bonding and easier ionization, we arrive at a small set of molecular fragments, where the C, N, O, and S atoms are in single and double covalent bonds typical for them (Fig. 4.1(a) and (b)).

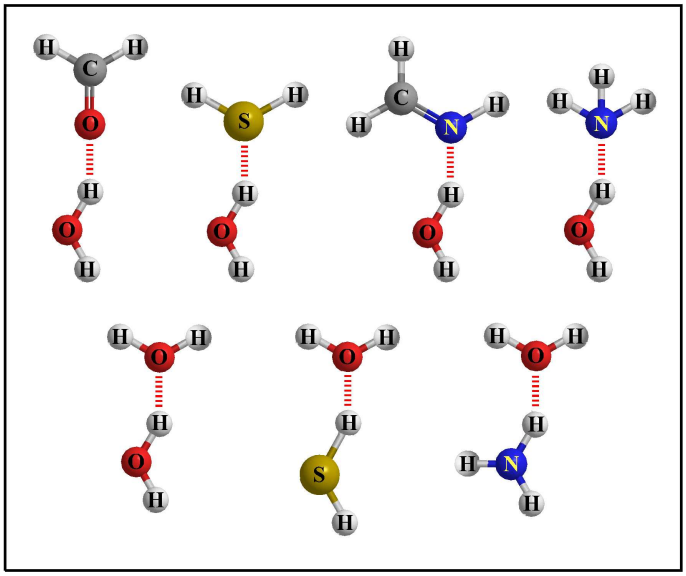

Figure 4.2: The simplest bimolecular species ($H_2O\cdots HCHO$, $H_2O\cdots H_2CNH$, $H_2O\cdots NH_3$, $NH_3\cdots H_2O$, $H_2O\cdots H_2S$, $H_2S\cdots H_2O$, and $H_2O\cdots H_2O$) that contain the most common types of hydrogen bonding between water and biochemically relevant species. The depicted set incorporates the fragments from Fig. 4.1(a) with their spare bonds saturated with hydrogen atoms. For further details see the text.

These fragments constitute building blocks common in larger structures like the enzyme lysozyme depicted in Fig. 4.1(c).

The simplest systems that incorporate the fragments from Fig. 4.1(a) are those in which the spare bonds are saturated with hydrogens, see Fig. 4.2. They contain oxygen and can be used to investigate the processes characteristic for a macromolecule embedded in water. Working with $H_2O\cdots HCHO$, $H_2O\cdots H_2CNH$, $H_2O\cdots NH_3$, $NH_3\cdots H_2O$, $H_2O\cdots H_2S$, $H_2S\cdots H_2O$, and $H_2O\cdots H_2O$ (p-donor$\cdots$ p-acceptor) we can easily analyze the results of our computations and identify the rudimentary effects that govern their interactions. Moreover, if the investigated phenomena are of fundamental nature, they are likely to exist in larger systems, as well. The selected species contain well known compounds like water, ammonia, formaldehyde, and hydrogen sulfide that should be ideal also for performing experimental studies of the discussed phenomena.

We shall begin with a comprehensive investigation of the ICD of the populated by inner-valence ionization, as well as Auger decay electronic states of $(H_2O)_2$ and shall return to $H_2O\cdots HCHO$, $H_2O\cdots H_2CNH$, $H_2O\cdots NH_3$, $NH_3\cdots H_2O$, $H_2O\cdots H_2S$, and $H_2S\cdots H_2O$ in Section 4.2.

4.1 Intermolecular Coulombic decay of singly and doubly ionized states of $H_2O\cdots H_2O$

The physical and chemical properties of water have been intensively studied (see, e.g., Refs. [97, 98] and references therein). The interest in understanding the characteristics

of this substance originates not only from its molecular or collective properties, but also from its strong impact on our daily life. The ability of water to form hydrogen bonds with itself and with other polar moleclues leads to its peculiar behavior and interaction with the environment. Its abundance in nature makes it the most important solvent in organic and inorganic chemistry, a medium for almost all biochemical reactions, and a prerequisite for the existence of almost all life forms on Earth. This calls for thorough investigations of processes which take place with the participation of water.

Accurate quantum mechanical calculations are ideal for studying clusters consisting of two or several water molecules [97]. Ample theoretical works have been devoted to the study of the water dimer in particular. This system is attractive because of its small size, relative simplicity, and importance for environmetal chemistry [99]. It allows a fine modelling of the H-bonding and of structural properties [97, 100]. In fact, new computational methods are tested on this system and compared to experimental results [98,101,102]. Most importantly, studying the water dimer we can concentrate on processes which involve only two H_2O molecules and better identify the rudimentary effects that govern their interaction.

Very recently the ICD phenomenon was observed experimentally in water dimer [14] and in big water clusters [15]. The results show that the ICD in water is extremely fast, leaving practically no time for an internal rearrangement of the participating molecules [14] (see also [103]), and that the emitted secondary electron has a low energy (between 0 and 10 eV) [14, 15]. One of our main objectives is to shed more light on the ICD phenomenon in water and to help in better understanding the experimental results.

In fact, ICD in water dimer was one of the illustrative examples in the first report on this de-excitation process [7]. First steps in the theoretical study of ICD following inner-valence ionization of small water clusters were undertaken in Ref. [11] where a rough estimate of the kinetic-energy spectrum of the emitted ICD electrons was made. In what follows, we will continue to study the ICD process following inner-valence ionization of a water dimer and expand our exploration of the matter by a first qualitative analysis of the ICD following Auger decay in water dimer which has not been measured so far. Interestingly, an analogy between the discussed in the previous chatper Ne_2 and $(H_2O)_2$ can be made, as far as the two systems are isoelectronic.

In order to analyze the possible decay mechanisms of the ionized water dimer we will use PECs of the initial and the final states of the processes. We will model the potential energy hypersurfaces of $(H_2O)_2$, $(H_2O)_2^+$, and $(H_2O)_2^{++}$ and work with the energy as a function of the distance between the two oxygen atoms, R_{O-O}. These one-dimensional

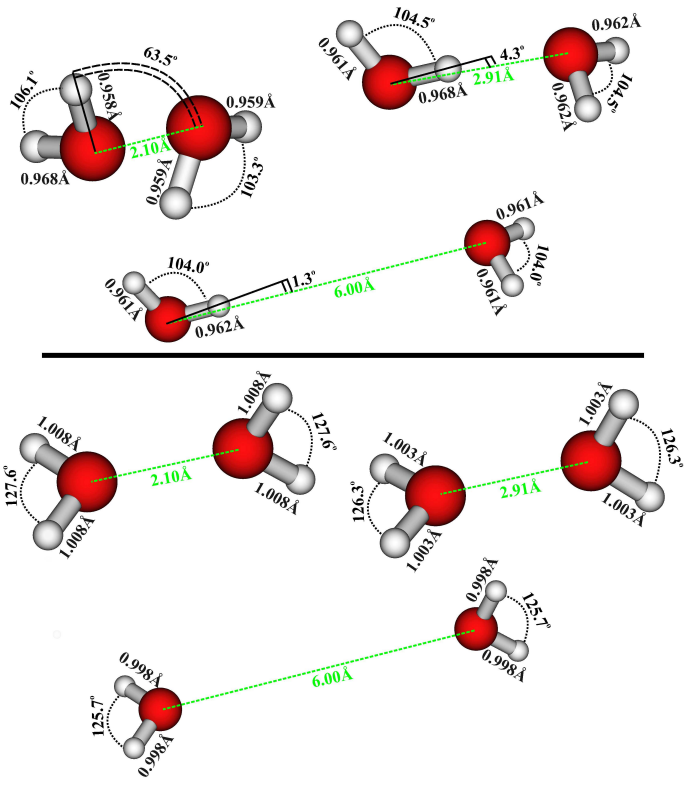

Figure 4.3: Optimized geometries of the neutral and two-site doubly ionized water dimer at fixed oxygen-oxygen distances of 2.10 Å, 2.91 Å, and 6 Å. Upper panel: Neutral $(H_2O)_2$ in C_s symmetry. Lower panel: two-site A_1 state of the dication $H_2O^+H_2O^+$ in C_{2V} symmetry. Note that the computed values of bond lengths and angles of the singlet and the triplet states are equal when shown with the precision used in the figure. For further details see the text.

cuts through the potential-energy hypersurfaces give a simplified, but, as we will see by a comparison with the experimental results wherever available, a meaningful treatment of the relaxation processes. It is thus possible to estimate features in the electron spectra of the intermolecular decay process of $(H_2O)_2^+$, and $(H_2O)_2^{++}$ for which precise calculations including the electron and nuclear dynamics are not currently feasible.

4.1.1 ICD and related decay processes initiated by an inner-valence vacancy

Before analyzing the electronic spectra and the possible decay modes, we would like to say a few words about the structures of the studied system. In the course of our study we have optimized the geometries of the water dimer in its neutral ground state, as well as in the ground state of $H_2O^+H_2O^+$. We have used ab-initio methods and basis sets that treat with good accuracy the electron correlation in the system (see Section 2.2.5). This was needed to correctly characterize the weakly interacting hydrogen bonded subunits of $(H_2O)_2$ and the Coulomb repulsion of the two-site dication.

The structural data of the water dimer and its dication are presented in Fig. 4.3 for several O-O distances. The optimized geometries of the neutral and of the ionized dimer

are characterized by two water molecules which lie in perpendicular planes. The neutral dimer $(H_2O)_2$ has its minimal energy at the O-O distances of 2.91 Å (1.95 Å hydrogen bond length) and possesses C_s symmetry, see the upper panel of Fig. 4.3. Our result is in an excellent agreement with Refs. [100–102] not only in terms of bond lengths, but of bond angles, as well. The angle between the H participating in the hydrogen bond, the oxygen of the proton-donor water molecule, and the oxygen of the proton-acceptor one is 4.3 degrees. It increases to as much as 63.1° at 2.10 Å which is the minimal value of the O-O separation in our study and decreases to 1.3° at 6 Å.

The relaxed $H_2O^+H_2O^+$ belongs to the higher C_{2V} symmetry group, as the two H_2O^+'s are oriented perpendicular to each other and have the maximally possible distance between the hydrogen atoms for a given O-O distance, due to the electrostatic repulsion of the partial charges in the system (see the lower panel of Fig. 4.3). The H-O-H angle and the O-H bond which describe the dication in the A_1 symmetry representation have very similar values in both singlet and triplet multiplicities and do not change significantly with the separation of the two parts of the dimer. The length of the O-H bond shortens from 1.008 Å to 0.998 Å and the H-O-H angle alters from 127.6° to 125.7° as the two ions are shifted apart from 2.10 to 6.00 Å. Their values can be compared with those of a single water molecule with a hole in the highest occupied molecular orbital (HOMO). Calculated with the same (RS3) method and basis set (d-aug-cc-pVQZ), the $^2B_1$ state of H_2O^+ has a O-H bond length of 0.996 Å and angle of 109.7°. Thus, the geometry of H_2O^+ cation is much closer to that of the ground state H_2O than to that of the two subunits in $H_2O^+H_2O^+$.

Electronic Spectra

Having the structure of the dimer at different intermolecular distances, we can compute and investigate its spectra. In this subsection we discuss the single- and double-ionization spectra of $(H_2O)_2$ which were calculated at the optimized geometries of the neutral water dimer. This means that we describe a system which was ionized and did not have time to relax. Therefore, our data will be useful for studying phenomena which are faster than the nuclear motion. This is the case for the ICD and related electronic decay processes which transpire in a femtosecond time scale. For completeness, we will later take a look at the double-ionization energies of the relaxed dication and compare them with those discussed here.

We begin our investigation with an overview of the possible relaxation modes of the singly ionized water dimer. For this purpose we examine its single- and double-ionization

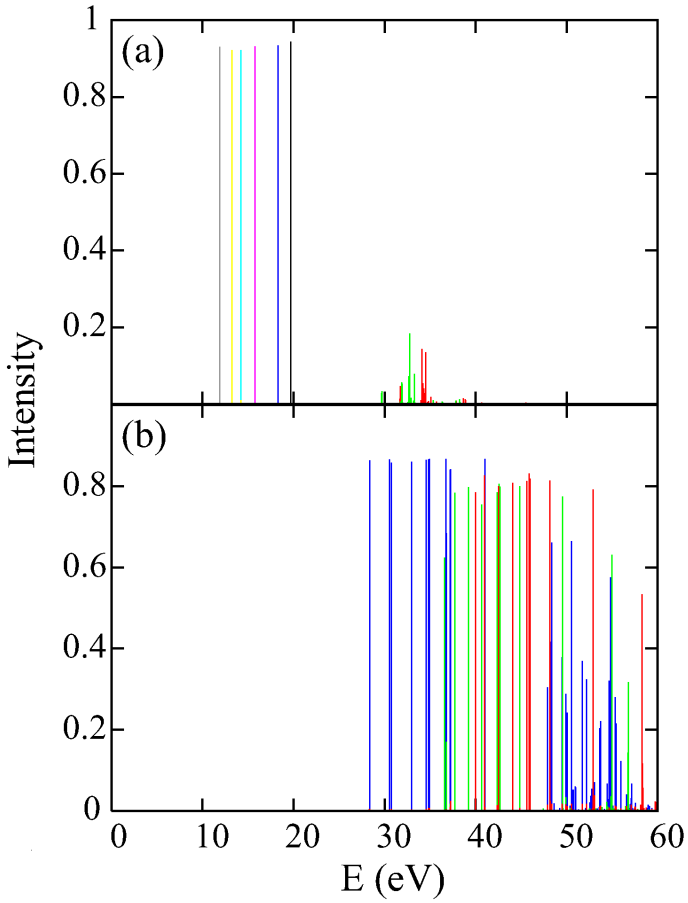

Figure 4.4: Ionization spectra of $(H_2O)_2$ with fully optimized geometry in C_s symmetry. The colors of the lines indicate different types of states. (a) Singly ionized water dimer with the following color encoding of the spectral lines: gray – $2a''^{-1}$, yellow – $8a'^{-1}$, cyan – $7a'^{-1}$, pink – $6a'^{-1}$, blue – $5a'^{-1}$, black – $1a''^{-1}$, green – $4a'^{-1}$, and red – $3a'^{-1}$. (b) Doubly ionized water dimer with the following spectral lines: blue - $H_2O^+H_2O^+$ states, green - states of the doubly ionized proton donor molecule $H_2O^{++}_{d.}H_2O$, and red - states of the doubly ionized proton acceptor molecule $H_2O^{++}_{a.}H_2O$. For further details see Tables 4.1, 4.2, and the text, as well as Ref. [11].

spectra in the energy range from 0 to 60 eV. The ionization potentials (IP) depicted in Fig. 4.4(a) characterize the initial states of the decay processes. One can clearly distinguish two types of spectral lines. The first one, with energies below 20 eV, correspond to electronic configurations with one hole in the outer-valence shell. Here, each line has high intensity and corresponds to a $H_2O^+(2p^{-1})H_2O$ state, as shown in Table 4.1. These states lie below the double-ionization threshold that is determined by the line lowest in energy in Fig. 4.4(b). They cannot participate in a processes accompanied by electron emission and may decay either radiatively or via coupling to the nuclear degrees of freedom. The green and red sets of lines beginning at about 30 eV relate to the $2s^{-1}$ states in the proton donor and proton acceptor, respectively. They are examples of the so-called "breakdown of the molecular orbital picture" [104] reflecting the strong correlation between the electrons. There, a removal of an electron from a particular molecular orbital gives rise to a multitude of ionic states forming a quasi-continuum of lines in the spectrum. For the isolated H_2O molecule this feature is well known, as its ionization spectrum was intensively studied, both theoretically and experimentally (see, e.g., Refs. [11, 54–56, 105, 106]). In

Table 4.1: Single-ionization potentials relevant for the ICD of water. Shown are computed values for $(H_2O)_2$ (both of the proton (p) - donor and the proton - acceptor) in comparison to the corresponding experimental values of H_2O taken from Ref. [54]. The states are assigned to Hartree-Fock molecular orbitals (MO) and in the case of the dimer the site on which the positive charge is localized is given.

Calculation $(H_2O)_2$ in symmetry C_s					Experiment H_2O in symmetry C_{2V}		
Ionized MO	Localization of the charge	Energy [eV] at R_{O-O} distance of:			Ionized MO	Energy [eV]	Relative Intensity[1]
		2.10 [Å]	2.91 [Å]	10.00 [Å]			
$3a'$	p^+-acceptor	33.89[2]	34.09[2]	33.44[2]	$2a_1$	32.62[2]	0.41
$4a'$	p^+-donor	33.11[2]	32.74[2]	33.36[2]			
$1a''$	p^+-acceptor	18.58	19.70	19.16	$1b_2$	18.78	1.68
$5a'$	p^+-donor	19.08	18.31	19.08			
$6a'$	p^+-acceptor	15.65	15.77	15.13	$3a_1$	14.84	1.16
$7a'$	p^+-donor	14.05	14.21	15.05			
$8a'$	p^+-acceptor	11.54	13.25	12.81	$1b_1$	12.60	1.00
$2a''$	p^+-donor	12.53	11.90	12.73			

[1]Relative to the $1b_1$ intensity. Taken from Ref. [54].
[2]The value of the spectral maximum.

our investigation on the dimers we are only interested in two peculiarities: 1) the $2s^{-1}$ states in both the proton donor and the proton acceptor have energies above that of $H_2O^+(2p^{-1})H_2O^+(2p^{-1})$ and 2) these energies are below that of $H_2O^{++}(2p^{-2})H_2O$. This is made clear by the double ionization spectrum of the system (shown in Fig. 4.4(b)) where the spectral lines of the *two-site* $H_2O^+(2p^{-1})H_2O^+(2p^{-1})$ states are depicted in blue, while those of the *one-site* $H_2O^{++}(2p^{-2})H_2O$ states are green for the proton donor and red for the proton acceptor.

Thus, $H_2O^+(2s^{-1})H_2O$ cannot autoionize and become $H_2O^{++}H_2O$, but can participate in a process accompanied by electron emission from the neutral subunit in the cluster, namely ICD. Another interesting detail of the double-ionization spectrum of the dimer is the change in the intensity of the spectral lines with a defined character (encoded by different colors in Fig. 4.4(b)). Those with energy below 48.23 eV are dominated by a single electron configuration $H_2O^+(2p^{-1})H_2O^+(2p^{-1})$ and have high intensities, while some of the higher in energy spectral lines form groups with lower intensity that correspond to $H_2O^+(2s^{-1})H_2O^+(2p^{-1})$. The states with two vacancies in $2s$ lie at even higher energies, above 65 eV and 80 eV for the two-site and one-site states, respectively (not shown in

Fig. 4.4(b)). The one-site $H_2O^{++}(2s^{-2})H_2O$ state lies below the triple ionization threshold of H_2O, which we have calculated to be 86.17 eV for the quartet and 89.51 eV for the doublet. Therefore, $H_2O^{++}(2s^{-2})H_2O$ cannot autoionize and become $H_2O^{3+}H_2O$.

Once we have inspected the broad picture, we can focus on $H_2O^{+}(2s^{-1})H_2O$ and the final states of their decay. These are shown in Fig. 4.5 which contains the spectra of the studied system with optimized geometries of $(H_2O)_2$ at O-O distances of 2.10, 2.91, and 6.00 Å. This will allow us to follow the spectral changes as the O-O distance changes. We will start at 6.00 Å, for which the interpretation of the spectrum is the simplest. The interaction of the two water molecules is very weak at this distance and their geometries are very similar to each other and close to that of an isolated water molecule (see Ref. [11, 102]). Consequently, their spectra are similar. The $2s^{-1}$ spectral lines are shown in the upper panel of Fig. 4.5 (a). They almost overlap, but even at this large distance those of the proton donor (depicted in green) are shifted slightly, but visibly to lower energies compared to those of the proton acceptor. This results from the interaction of the hydrogen atom and the two oxygens of the hydrogen bond. The oxygen which acts as a proton acceptor pulls the H-atom and the positive charge attributed to it away from the donor molecule, thus slightly reducing the electron density around the oxygen of the acceptor. The resulting partial charge is more positive and the energy needed to create a hole in the $2s$ level is slightly higher than in the isolated H_2O molecule. The effect on the donor is in the opposite direction and its spectral lines are slightly shifted to lower energies. This phenomenon is enhanced at smaller O-O distances and will lead, as we will later see, to a very different behavior of the $2s^{-1}$ potential curves in the proton-donor and proton-acceptor molecules of $(H_2O)_2$.

The donor and the acceptor spectral lines highest in intensity are marked by an arrow in all the figures. They will be in the center of our discussion below, because the corresponding ionic states are the most populated after inner-valence ionization of the system and undergo changes typical for the whole system as the O-O distance varies. These lines are used for constructing the PECs of the states decaying via ICD discussed in the next subsection.

The double-ionization spectrum of water dimer at $R_{O-O} = 6.00$ Å is shown in the lower panel of Fig. 4.5(a). The green and red lines stand for $H_2O^{++}(2p^{-2})$ one-site states of the donor and acceptor, respectively. It is interesting to compare their energies with those of the corresponding states populated in the Auger spectrum of the isolated water molecules [55], see Table 4.2. The blue lines in the lower panel of Fig. 4.5(a) correspond to the two-site $H_2O^{+}(2p^{-1})H_2O^{+}(2p^{-1})$ states. Their repulsive nature is demonstrated by

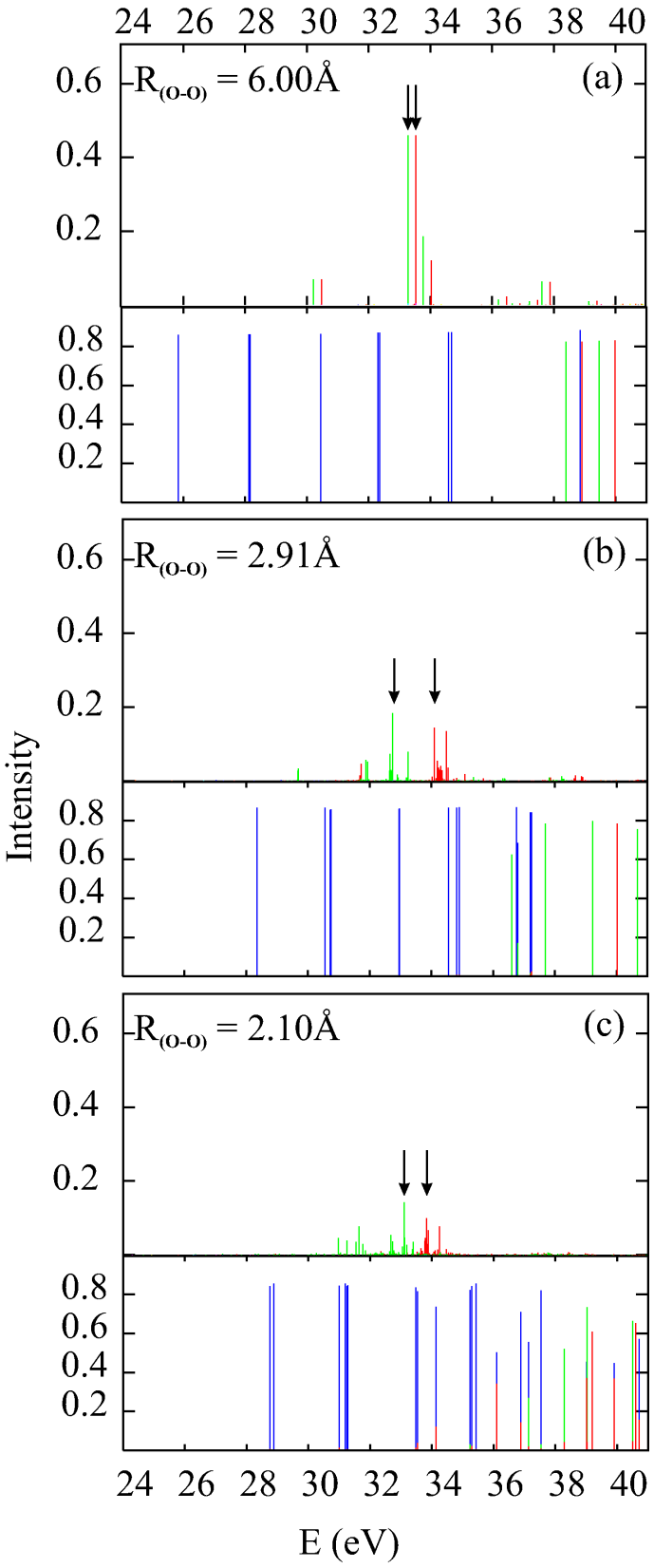

Figure 4.5: Ionization spectra of $(H_2O)_2$ for three different oxygen-oxygen distances: 2.10Å (a), 2.91Å or the equilibrium (b), and 6.00Å (c). Upper panels – singly ionization spectra, lower panels – double ionization spectra. The colors of the lines indicate different types of states. In the upper panel: green – $H_2O^+_{d.}(2s^{-1})H_2O$; red - $H_2O^+_{a.}(2s^{-1})H_2O$. In the lower panels: blue – $H_2O^+H_2O^+$ states, green – $H_2O^{++}_{d.}H_2O$, and red – $H_2O^{++}_{a.}H_2O$. Arrows denote the line with the highest intensity. The energies of these lines are used in the construction of the corresponding PECs in Fig. 4.7. For further details see Tables 4.1 and 4.2, as well as the text.

Table 4.2: Experimental values for double-ionization potentials of H_2O as obtained by Auger electron spectroscopy taken from Refs. [55–57]. The relative intensities given are calculated using the ADC(2) scheme. These potentials are used for the asymptotic assignment of the PECs presented in Fig. 4.7.

Ionized MOs	Character	Energy [eV]	Intensity[1]	Peak Nr.[2]
$2a_1\ 2a_1$	$^1A_1$	82.23	0.60	P1
$2a_1\ 1b_2$	$^1B_2$	72.23	0.50	P2
$2a_1\ 3a_1$	$^1A_1$	67.53	0.51	P3.1
$2a_1\ 1b_1$	$^1B_1$	64.63	0.82	P3
$2a_1\ 1b_2$	$^3B_2$		0.49	
$2a_1\ 3a_1$	$^3A_1$	57.83	0.71	P4
$2a_1\ 1b_1$	$^3B_1$		0.82	
$1b_2\ 1b_2$	$^1A_1$	53.23	0.39	P5
$1b_2\ 3a_1$	$^1B_2$	46.13	0.45	P6
$1b_2\ 3a_1$	$^3B_2$		0.45	
$1b_2\ 1b_1$	$^1A_2$		0.64	
$3a_1\ 3a_1$	$^1A_1$		0.56	
$1b_2\ 1b_1$	$^3A_2$		0.63	
$3a_1\ 1b_1$	$^1B_1$	41.33	0.75	P7
$1b_1\ 1b_1$	$^1A_1$		1.00	
$3a_1\ 1b_1$	$^3B_1$	39.13	0.72	P8

[1]Relative to that of the computed $1b_1\ 1b_1\ ^1A_1$ state.
[2]In the experimental Auger spectrum of H_2O.

the PECs which are constructed with their use and are closely examined in Section 4.1.1.

Let us now take a look at Fig. 4.5(b) containing the spectra of the dimer in its ground state geometry. As already stated, the ICD process is ultrafast, much faster than the motion of the oxygen atoms and we can expect these spectra to be the most relevant for the decay. Consequently, Fig. 4.5(b) is used to show which of the ICD and related phenomena take place. For this purpose, we examine the spectral lines of the decaying $2s^{-1}$ states denoted by an arrow in the figure and compare their energies with those of the doubly ionized system. From the figure and the nature of the involved states we can conclude that at this distance the direct, as well as exchange ICD initiated by a $2s$ vacancy are energetically allowed processes in both the proton donor and the proton acceptor, as already found in [11]. In brief:

$$H_2O^+(2s^{-1})H_2O \longrightarrow H_2O^+(2p^{-1}) + H_2O^+(2p^{-1}) + e^-_{ICD}.$$

We now turn to the question whether ETMD is possible at the equilibrium distance. The energy of the singly ionized proton-acceptor molecule is higher than that of the acceptor and the one-site double-ionization threshold of the proton acceptor is rather low. Nevertheless, even if we assume the maximal error of the computation methods that we use [107], ETMD seems unlikely to be a possible process for nearly all the populated states. In particular, when performing the energy adjustment to the experimental values for the corresponding molecular states at asymptotic distances, as discussed in Sec. 2.2.5., one sees that this channel is actually closed. However, it is apparent from the upper panel of Fig. 4.5(b) that there are satellite states of $2s^{-1}$ nature with very low intensity, but high in energy which are above that of the double ionization threshold ($H_2O^{++}H_2O$) and thus can undergo ETMD, i.e. decay processes of the type:

$$H_2O^+(2s^{-1})H_2O \longrightarrow H_2OH_2O^{++}(2p^{-2}) + e^-_{ETMD}.$$

The low population of these states high in energy, as well as the possibility of these states to decay also via the much more probable ICD mechanism, makes the ETMD channel unimportant.

The $(H_2O)_2$ geometry at $R_{O-O} = 2.10$ Å is characterized by almost equal distances of the two oxygen atoms from the H-atom of the hydrogen bond (see Fig. 4.3) and by a rather strong interaction of these atoms. The single- and double-ionization spectra of the dimer at this intermolecular separation are shown in Fig. 4.5(c). The spectra reflect the strong overlap between the MOs of the two constituents and the decreased distinguishability between the proton-donor and the proton-acceptor water molecules. The two-site $H_2O^+(2p^{-1})H_2O^+(2p^{-1})$ states lie at higher energies due to the stronger electrostatic repulsion of the two positive charges in the system. However, some of these states are still positioned below the spectral lines of $2s^{-1}$. Therefore, even at this very small separation the ICD takes place. Another feature of the spectra is the much more pronounced breakdown of the molecular orbital picture. It is enhanced by the overlap of the MOs and the penetration of the $2p$ orbitals of one of the subunits into the other. An interesting point to note is that looking at Fig. 4.5(c) the possibility of an open autoionization channel from the $2s^{-1}$ state could not be excluded, as far as the energy difference of the states that participate is within the computational error of the methods we have used. However, when performing the asymptotic shifts described above, one finds that autoionization is energetically forbidden.

Finally, we should highlight that with the decrease of R_{O-O}, we observe an increase of the energy split between the one-site ionization potentials belonging to the proton-donor

Table 4.3: Types, energies, and asymptotic assignment of the PECs of the singly and doubly ionized states of $(H_2O)_2$ depicted in Fig. 4.6.

State type	Energy [eV] in Fig. 4.6 at R_{O-O} distance of 6[Å]	Asymptotically adjusted to:	Group numbering in Fig. 4
Relaxed dication	27.06	$H_2O^+(1b_1^{-1}\ ^2B_1)$-$H_2O^+(1b_1^{-1}\ ^2B_1)$	401
Final for ICD	27.56	$H_2O^+(1b_1^{-1}\ ^2B_1)$-$H_2O^+(1b_1^{-1}\ ^2B_1)$	402
Final for ICD	29.80 (29.83)	$H_2O^+(1b_1^{-1}\ ^2B_1)$-$H_2O^+(2a_1^{-1}\ ^2A_1)$	403 (404)
Closed[1] for ICD	32.07	$H_2O^+(3a_1^{-1}\ ^2A_1)$-$H_2O^+(3a_1^{-1}\ ^2A_1)$	405
Decaying via ICD	32.48 (32.73)	$H_2O^+(2a_1^{-1}\ ^2A_1)^2$-$H_2O$	406 (407)
Closed[1] for ICD	33.70 (33.76)	$H_2O^+(1b_1^{-1}\ ^2B_1)$-$H_2O^+(1b_2^{-1}\ ^2B_2)$	408 (409)
Closed for ICD	35.93	$H_2O^+(3a_1^{-1}\ ^2A_1)$-$H_2O^+(1b_2^{-1}\ ^2B_2)$	410

[1]These dicationic states can be final of the ICD process, but not for the most populated states undergoing ICD shown in Fig. 4.6 (see also text).

[2]The value of the spectral maximum of $H_2O^+(2a_1^{-1}\ ^2A_1)$ from Ref. [54] is used.

($H_2O_{d.}$) and the proton-acceptor ($H_2O_{a.}$), respectively (see Fig. 4.5). Spectral lines that are degenerate at asymptotic distance differ at $R_{O-O} = 2.91$ Å by as much as 1.4 eV in $H_2O^+H_2O$ and 2.5 eV in $H_2O^{++}H_2O$. This is a result of the change in the charge density in $H_2O_{d.}$ and $H_2O_{a.}$ at the equilibrium R_{O-O} of $(H_2O)_2$ due to the interaction of the bonding hydrogen with the two oxygen atoms, as already discussed above.

Ab-initio computed PECs

For our semi-quantitative study of the electronic decay we need the PECs of the participating states of $(H_2O)_2$, $H_2O^+H_2O$, $H_2O^+H_2O^+$, and $H_2O^{++}H_2O$ as a function of the O-O distance. In order to describe our reduced dimensionality model we will begin with the ground state of the system – $(H_2O)_2$. In its geometry optimization we have kept R_{O-O} fixed and allowed the other bonds, as well as the angles in the dimer to vary. The resulting ground-state curve, which is a cut along the minimal in energy O-O pathway, is depicted in Fig. 4.6(a). It is characterized by a shallow well of 0.21 eV depth at an O-O distance of 2.91 Å. This is an expected value which matches the fully optimized geometry of $(H_2O)_2$ reported in a number of papers, see e.g. Refs. [100, 101]. The ground state of the dimer rapidly increases its energy at smaller distances up to 0.65 eV at $R_{O-O} =$ 2.10 Å, where the H-atom of the bond is equidistant from the two oxygens, while at 6 Å the two water molecules are very weakly bound, by slightly less than 0.02 eV.

The PECs in Fig. 4.6(b) are based on that of the ground state, as they have been constructed by adding the IPs and DIPs of the corresponding states to it and later shifted to fit the experimental values asymptotically (see Section 2.2.5). The two black curves in Fig. 4.6(b) are those of the $H_2O^+(2s^{-1})H_2O$ states decaying by ICD. There are many

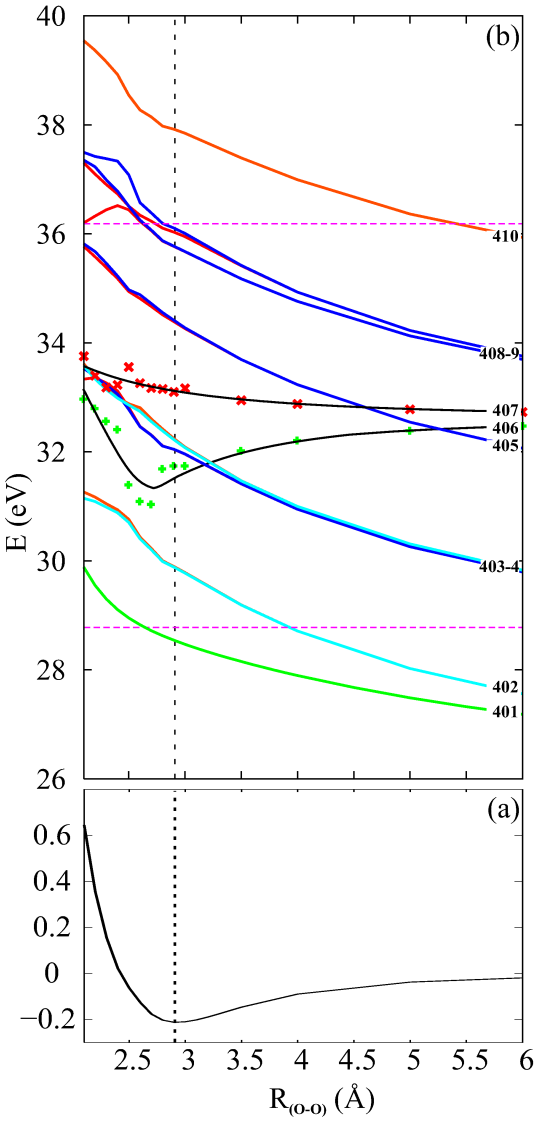

Figure 4.6: Computed potential energy curves of $(H_2O)_2$, $H_2O^+H_2O$, and $H_2O^+H_2O^+$. The equilibrium oxygen-oxygen distance (R_{O-O}) of the neutral $(H_2O)_2$ (2.91 Å) is marked by a vertical dashed line. Panel (a): the ground state of the water dimer. Panel (b): the asymptotically adjusted energies of the spectral lines with highest intensity of the proton acceptor and the proton donor are depicted with red crosses and green pluses, respectively. Note that these highest populated states are indicated in Fig. 4.5. Other states decaying by ICD can also be seen in Fig. 4.5, they are located in between the two horizontal dashed lines shown. To guide the eye, they are least square fitted with the two black curves shown. The blue and red repulsive curves depict the computed doubly ionized $H_2O^+H_2O^+$ states with the geometry of $(H_2O)_2$ optimized at fixed R_{O-O}. The nearly degenerate green curves stand for the energy of the relaxed $H_2O^+H_2O^+$ singlet and triplet ground state. For further details see Table 4.3, as well as the text.

states which undergo ICD and we concentrate here on those of highest intensity only, one for the proton donor and one for the proton acceptor. The curves shown have been obtained by fitting to the energy values of selected (see the previous subsection) spectral lines of the proton acceptor and the proton donor which are depicted with red crosses and green pluses, respectively. The two PECs have completely different behavior. The one for the acceptor is a rather flat repulsive curve decreasing by 1.0 eV within the whole range of the intermolecular distances shown in the figure. The one for the donor is an attractive curve with a well at about 2.7 Å. The minimum is about 1.27 eV lower than the energy at $R_{(O-O)}$ of 6.00 Å. This dissimilarity in the behavior of the two curves originates from the change in the electron densities around the O-atoms of the proton-donor and the proton-acceptor molecules mentioned in the previous subsection. Furthermore, as

it was already discussed the ionization of $2s^{-1}$ MO gives rise to a multitude of states, because of the strong electronic correlation. To reflect this, we have drawn in Fig. 4.6(b) two horizontal dashed lines to indicate the energy band within which those states are located. If energetically allowed, all states within this band can undergo ICD. However, for simplicity of discussion we restrict ourselves here to the two PECs representing the most populated $2s^{-1}$ states.

The final states populated by the ICD decay are the two-site triplet and singlet $H_2O^+(2p^{-1})H_2O^+(2p^{-1})$ shown as blue and red repulsive curves in Fig. 4.6(b). Their character, asymptotic assignment, multiplicity, and symmetry are given in Table 4.3. There are two groups of these curves that lie below the PECs of the most populated $H_2O^+(2s^{-1})H_2O$ states at 2.91 Å and are thus particularly suited as final states for ICD transitions. In this decay an electron from the $2p$ shell will fill the $2s$ vacancy of the initially ionized water molecule and the released energy will eject an electron from the other water molecule. A Coulomb explosion will follow as a result of the repulsion of the two H_2O^+ produced. The average value of KER, obtained from the difference in the energies of the PECs of the $H_2O^+H_2O^+$ states at 2.91 Å and infinite separation of the two ions, is 4.8 eV. This value for the expected KER has to be compared to the experimentally obtained one of about 4.2 eV [14]. The discrepancy of 0.6 eV is the energy which goes into the internal degrees of freedom of the two separating H_2O^+. As shown recently [103], mainly to the rotation of the proton-donor molecule during the back-to-back flight of the two ions in the Coulomb explosion. This 0.6 eV cannot, of course, be determined by Fig. 4.6. The corresponding energy of the emitted ICD electron is determined as the difference in the energy of the initial and the final state at the ground state distance which is denoted by the vertical dashed line in the figure. As the result of the decay of the proton-donor molecule we thus have an ICD electron with energy of 2.6 eV if the products of the process are $H_2O^+(1b_1^{-1}\ ^2B_1)$-$H_2O^+(1b_1^{-1}\ ^2B_1)$ and of only 0.2 eV if they are $H_2O^+(1b_1^{-1}\ ^2B_1)$-$H_2O^+(3a_1^{-1}\ ^2A_1)$. The PEC of the proton acceptor is higher in energy as seen in Fig. 4.6(b) and leads to ICD-electron energies which are 1.35 eV above those of the donor. Taking into account the decay of the whole band of $2s^{-1}$ states, the spectrum of the electrons emitted in the ICD process should spread between 0 and about 12 eV with a maximum at the low-energy limit (see Fig. 4.13 where equation 4.1 is implemented, as well as [11]). This is in an excellent agreement with the experimental results for the ICD-electron spectrum reported in Ref. [14], as well as in Ref. [15].

The KER of the ICD initiated in the $H_2O_{a.}$ and $H_2O_{d.}$ are very similar if the process is very fast. However, we can still expect that due to the different shape of the curves of

the decaying state of the proton donor and the proton acceptor their KER can slightly alter. The electron wave packet can move a little bit to smaller O-O distances in the case of $H_2O^+_{d.}(2s^{-1})H_2O$, since the PEC is attractive around 2.91 Å. Therefore, a slight shift to higher kinetic energies could be observed. In contrast, in the case of the repulsive curve of the acceptor, $H_2O^+_{a.}(2s^{-1})H_2O$, the wave packet may move a little bit to larger O-O distances before it drops down to the $H_2O^+H_2O^+$ states and a slight shift lower KER may be seen. However, such kind of split in the KER spectrum was not observed experimentally (see Fig. 4.5 of Ref. [14]) suggesting once again that the ICD is so fast that the dimer explodes by the Coulomb repulsion before there is time for the nuclei to change their positions.

We stress that unlike the diatomic noble-gas clusters which were discussed in Section 3 and extensively studied experimentally [9, 16, 17], in polyatomics the excess energy is not distributed only between the ICD electron and the KER. This energy will be distributed to rotational and vibrational degrees of freedom in the system, as well. However, systematic studies of these effects can only be performed if the nuclear dynamics during the process are accounted for on the many multi-dimensional potential energy surfaces participating in the ICD process. This heavy task is much beyond our present work. A first step in this direction is the investigation of the KER which has already been undertaken in Ref. [103], where the nuclear dynamics throughout the Coulomb explosion were treated quasi-classically.

Until now, we have assumed an instantaneous ICD process in which the nuclei of the molecules in the dimer barely move. Accordingly, we have used optimized geometries of the system in its ground state and then calculated the spectra of these structures. Indeed, the results obtained here and in the respective investigation of the resulting Coulomb exposion [103] are in accord with the measurements on the water dimer [14]. From these measurements alone it has also been concluded that the ICD is ultrafast. Without the knowledge of lifetimes of the various states decaying by ICD it is impossible to make more quantitative statements. Such lifetimes have been computed (see, e.g. [8–10, 25, 26]) and measured before [30], but not for complex systems like the water dimer. Nevertheless, the following observation based on PECs alone is also informative.

If the wave packet will have time to evolve on the PECs of the $H_2O^+(2s^{-1})H_2O$ states before the decay is accomplished, the KER distribution will be much broader and will tend to show two distinctive maxima, reflecting the different character of the PECs for the inner-valence ionized proton donor (attractive PEC) and proton acceptor (repulsive PEC). One can also hypothetically inquire a transition to relaxed final states. The two almost

degenerate green lines in Fig. 4.6(b) are the PECs of the singlet and triplet of $H_2O^+H_2O^+$ with holes in the HOMO and the HOMO−1 MOs at their fully optimized geometries. These two-site states have, as expected, lower energies than the PECs previously shown. In addition, as a consequence these two distinctive maxima of the KER spectrum will be shifted by nearly 2 eV to lower energies, since the relaxed final PECs are less repulsive than those of the unrelaxed dication. Clearly, none of these trends was observed experimentally.

4.1.2 ICD following Auger decay in water

Let us now turn to the question of the intermolecular decay modes of one-site dicationic states of water dimer. The $H_2O^{++}H_2O$ states can be populated not only by a direct photo-ionization, but also by an Auger decay [55]. The Auger decay itself produces high energy electrons that have no or very little direct genotoxic effect in living cells. However, as this has already been shown in the case of noble gas clusters, the final Auger states can further decay by ICD if the system has a suitable environment. Since the ICD produces typically low-energy electrons, such kind of two-step decay of core ionized water molecules can be a direct source of LEEs. It is, thus, of greater interest to investigate the ICD after Auger decay in water dimer and, more importantly, the energies of its products.

Although the ICD of $H_2O^{++}H_2O$ states has already been proposed in Ref. [7], the process has not been studied until now. For this reason, we will examine the relaxation modes of the states most populated via Auger decay of the water dimer that have energies in the range from 60 to 90 eV. These are the one-site dicationic states of the type $H_2O^{++}(2p^{-1}2s^{-1})H_2O$ and $H_2O^{++}(2s^{-2})H_2O$. At equilibrium geometry they lie above the triple ionization threshold of $(H_2O)_2$ and thus the following cascade can take place: after core ionizing an O1s electron in one of the water molecules an Auger decay brings the initially ionized H_2O into dicationic states that further decay by ICD or related phenomena. The consecutive steps of the process can be written in short as:

Step 1 (core ionization):

$$H_2OH_2O \xrightarrow{h\nu} H_2O^+(1s^{-1})H_2O + e^-_{photo},$$

Step 2 (Auger decay):

$$H_2O^+(1s^{-1})H_2O \longrightarrow H_2O^{++}(2p^{-2}/2s^{-1}2p^{-1}/2s^{-2})H_2O + e^-_{Auger},$$

Step 3 (ICD or ETMD):

$$H_2O^{++}(2s^{-1}2p^{-1}/2s^{-2})H_2O \longrightarrow H_2O^{++}(2p^{-2}) + H_2O^{+}(2p^{-1}) + e^{-}_{ICD/ETMD}.$$

Model PECs

In order to examine the energies of the products of the ICD process (the last step of the above cascade) we employ a simple model for the PECs of doubly and triply ionized states of $(H_2O)_2$. We will use horizontal lines for the bound $H_2O^{++}H_2O$ states, $1/R$ curves for the $H_2O^{+}H_2O^{+}$ states, and $2/R$ curves for the $H_2O^{++}H_2O^{+}$ states. All the curves will be asymptotically adjusted to the experimentally obtained energies of the corresponding ionic fragments [54, 55, 57]. Although this is a crude approximation, our experience with PECs computed fully ab initio and those obtained with this simple model for Ne_2, Ar_2, and NeAr [68, 90, 108] (see also Chapter 3) shows that the model PECs give a good estimation of the possible decay channels and their energetics. The additional complication in the case of molecular dimers, namely the internal nuclear degrees of freedom, is effectively minimized by the extreme efficiency of the decay processes we are interested in. As we saw in the previous section, the assumption that the nuclei are fixed during the ICD process leads to results that agree well with the experimental observations. In addition, at intermolecular distances larger than 2.91 Å the computed PECs of the two-site dicationic states discussed in the previous section are very close to $1/R$ curves. All this gives us the confidence that the model curves to be discussed in this section provide a good qualitative description of the decay processes of interest.

The model curves for the one-site doubly and two-site triply ionized states of water dimer in the energy range from 60 to 90 eV are shown in Fig. 4.7. Their character, asymptotic assignment, multiplicity, and symmetry are collected in Table 4.4. The repulsive $H_2O^{++}H_2O^{+}$ curves form three groups which contain PECs of states that are asymptotically adjusted to energies formed as a sum of the energy of a water dication in a singlet state and the energy of a water monocation in a doublet state, see Table 4.4. Triplet dicationic states can also undergo ICD and their contribution is included in the total ICD spectrum reported below. However, for the ease of presentation we will not discuss them explicitly in the following. Accordingly, we have red, green, and blue sets comprised of all combinations of the three lowest dicationic configurations of the type $H_2O^{++}(2p^{-2})$ and the three lowest monocationic configurations of the type $H_2O^{+}(2p^{-1})$. The one-site dicationic states of the type $H_2O^{++}(2p^{-1}2s^{-1}/2s^{-2})H_2O$ are shown as black horizontal lines in Fig. 4.7.

Table 4.4: Types, energies, and asymptotic adjustment of the model PECs of the one-site doubly ionized and the two-site triply ionized states of $(H_2O)_2$ depicted in Fig. 4.7.

State type	Energy [eV] at R_{O-O} distance of 6[Å]	Asymptotically adjusted to:	Group numbering in Fig. 4.7
Final for ICD	56.53	$H_2O^{++}(3a_1^{-1}1b_1^{-1}\ ^3B_1$ (P8^1))-$H_2O^+(1b_1^{-1}\ ^2B_1)$	t1
Final for ICD	58.73	H_2O^{++}(states of P7^1)-$H_2O^+(1b_1^{-1}\ ^2B_1)$	r1
Final for ICD	58.77	$H_2O^{++}(3a_1^{-1}1b_1^{-1}\ ^3B_1$(P8^1))-$H_2O^+(3a_1^{-1}\ ^2A_1)$	t2
Final for ICD	60.97	H_2O^{++}(states of P7^1)-$H_2O^+(3a_1^{-1}\ ^2A_1)$	g1
Final for ICD	63.53	H_2O^{++}(states of P6^1)-$H_2O^+(1b_1^{-1}\ ^2B_1)$	r2
Decaying via ICD	64.63	H_2O^{++}(states of P3^1)-H_2O	61
Final for ICD	64.91	H_2O^{++}(states of P7^1)-$H_2O^+(1b_2^{-1}\ ^2B_2)$	b1
Final for ICD	65.77	H_2O^{++}(states of P6^1)-$H_2O^+(3a_1^{-1}\ ^2A_1)$	g2
Doubly ionized	67.00	$H_2O^+(2a_1^{-1}\ ^2A_1)^2$-$H_2O^+(2a_1^{-1}\ ^2A_1)^2$	62
Decaying via ICD	67.53	$H_2O^{++}(2a_1^{-1}3a_1^{-1}\ ^1A_1$ (P3.1^1))-H_2O	63
Final for ICD	69.71	H_2O^{++}(states of P6^1)-$H_2O^+(1b_2^{-1}\ ^2B_2)$	b2
Final for ICD	70.63	$H_2O^{++}(1b_2^{-2}\ ^1A_1$ (P5^1))-$H_2O^+(1b_1^{-1}\ ^2B_1)$	r3
Decaying via ICD	72.23	$H_2O^{++}(2a_1^{-1}1b_2^{-1}\ ^1B_2$ (P2^1))-H_2O	64
Final for ICD	72.87	$H_2O^{++}(1b_2^{-2}\ ^1A_1$ (P5^1))-$H_2O^+(3a_1^{-1}\ ^2A_1)$	g3
Final for ICD	76.81	$H_2O^{++}(1b_2^{-2}\ ^1A_1$ (P5^1))-$H_2O^+(1b_2^{-1}\ ^2B_2)$	b3
Decaying via 3e-ICD	82.23	$H_2O^{++}(2a_1^{-2}\ ^1A_1$ (P1^1))-H_2O	65

[1]For details see Table 4.2 and the text.

[2]The value of the spectral maximum of $H_2O^+(2a_1^{-1}\ ^2A_1)$ is used [54].

Analogously to the $2s^{-1}$ state of water, which we have analyzed above, the $H_2O^{++}H_2O$ states within the energy range of 60 to 90 eV are an andmixture of several electronic configurations. All of the one-site dications include a $2s^{-1}$ type one-hole configuration which interacts strongly with its $2p^{-2}np$ satellites. Therefore, sets of lines associated to these PECs are present in the spectrum of the dimer (see Ref. [11], Fig. 6). Thus, an energy band like the one formed for $H_2O^+(2s^{-1})H_2O$ may better describe them. However, we have decided not to overburden the figure and work with a single line at the center of each set. This should not influence the conclusions which we make, because as we have already pointed out, all lines in each set follow the same pattern of behavior. Another pronounced effect will be the splitting of the curves at small R_{O-O}. Nevertheless, assuming that the decay processes discussed here are orders of magnitude faster than the oxygen motion, the heavy atoms in the two subunits in the cluster should only slightly move before the decay takes place. Therefore, we expect that our estimates for the ICD electron energies and KER accompanying the relaxation modes which are collected in Table 4.5 should reflect reality to a good approximation.

The $H_2O^{++}H_2O$ states can be divided into two groups. The first consists of the three lower lying states which are of $2s^{-1}2p^{-1}$ type and the second consists of one state of $2s^{-2}$ character. The three lower lying states have been assigned to $H_2O^{++}(2a_1^{-1}1b_1^{-1}\ ^1B_1)$, $H_2O^{++}(2a_1^{-1}3a_1^{-1}\ ^1A_1)$, and $H_2O^{++}(2a_1^{-1}1b_2^{-1}\ ^1B_2)$, corresponding to peaks P3, P3.1, and

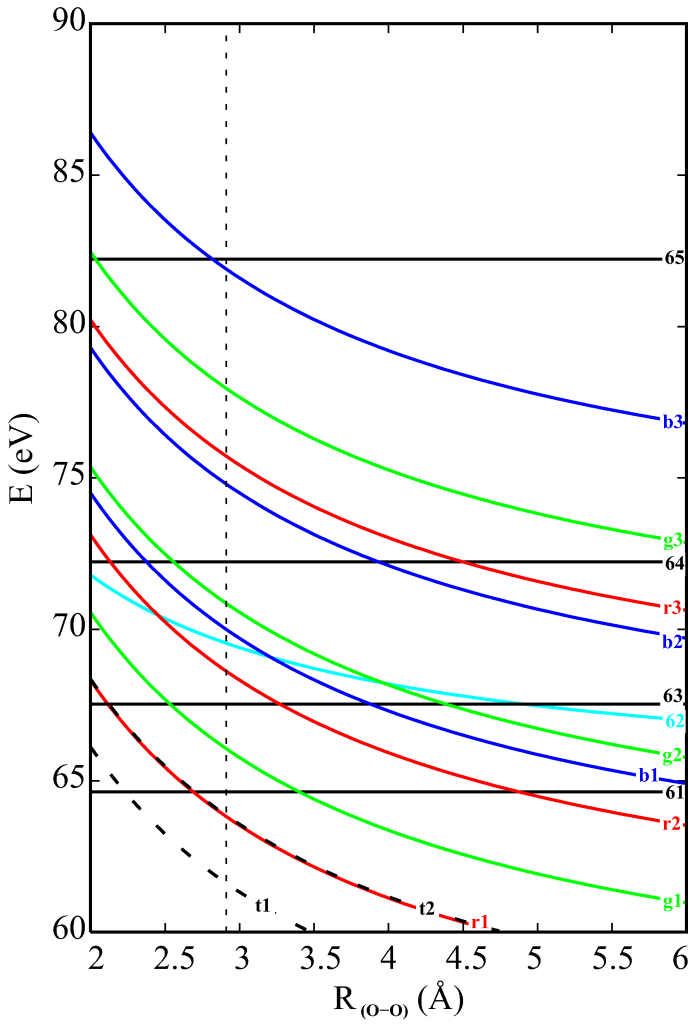

Figure 4.7: Energy diagram of the ionized states of $(H_2O)_2$ in the energy range 60 - 90 eV. The equilibrium oxygen-oxygen distance (R_{O-O}) of the neutral $(H_2O)_2$ (2.91 Å) is marked by a vertical dashed line. The horizontal lines depict bound $H_2O^{++}H_2O$ states, while the repulsive $1/R$ potential curve represent $H_2O^{+}H_2O^{+}$ states and the repulsive $2/R$ potential curves the $H_2O^{++}H_2O^{+}$ ones. For further details see Table 4.4 and the text.

P2 in the Auger experiment of isolated water molecules, respectively (see Table 4.2). The highest in energy dicationic state has been assigned to $H_2O^{++}(2a_1^{-2}\ ^1A_1)$, corresponding to peak P1 in the experimental spectrum. If we now examine the repulsive $H_2O^{++}H_2O^{+}$ curves below them, we can determine the type of decay which can take place. A direct ICD will be the preferable decay mode of the one-site dicationic states produced by O1s Auger. This scenario has been already discussed in detail in Chapter 3 for the case of van der Waals dimers. The multiplicity of the initially ionized subunit does not change in the course of a direct process. Thus, the dICD will dominate the relaxation modes by electron transfer. Taking this in consideration we will not discuss the possibility of eICD or ETMD here. The dICD process is described by a 2p electron that fills the 2s vacancy in the same $H_2O^{++}(2s^{-1}2p^{-1})$ subunit to produce $H_2O^{++}(2p^{-2})$ resulting in an energy transfer to its neighbor where a 2p electron is ejected, see the detailed listing in Table 4.4 and 4.5.

Table 4.5: Electronic states of $H_2O^{++}H_2O$ which undergo ICD to $H_2O^{++}H_2O^+$. Given are the expected energy at which the spectrum of the emitted electron is maximal (in eV), as well as the position of the maximum in the kinetic energy release spectrum (Max. KER) of the back-to-back exploding ions (in eV).

BEFORE DECAY → AFTER DECAY ↓	Energy of the ICD electron (in eV)				Max. KER (in eV)
	H_2O^{++}(states of P3[1])-H_2O	$H_2O^{++}(2a_1^{-1}3a_1^{-1})$ $^1A_1$ (P3.1[1])-H_2O	$H_2O^{++}(2a_1^{-1}1b_2^{-1}$ $^1B_2$ (P2[1]))-H_2O	$H_2O^{++}(2a_1^{-2}$ $^1A_1$ (P1[1]))-H_2O	
$H_2O^{++}(3a_1^{-1}1b_1^{-1}$ $^3B_1$ (P8[1])) - $H_2O^+(1b_1^{-1}$ $^2B_1)$	3.0067	5.9067	10.6067	20.6067	
H_2O^{++}(states of P7[1]) - $H_2O^+(1b_1^{-1}$ $^2B_1)$	0.8067	3.7067	8.4067	18.4067	
$H_2O^{++}(3a_1^{-1}1b_1^{-1}$ $^3B_1$ (P8[1])) - $H_2O^+(3a_1^{-1}$ $^2A_1)$	0.7667	3.6667	8.3667	18.3667	
H_2O^{++}(states of P7[1]) - $H_2O^+(3a_1^{-1}$ $^2A_1)$	–[2]	1.4667	6.1667	16.1667	
H_2O^{++}(states of P6[1]) - $H_2O^+(1b_1^{-1}$ $^2B_1)$	–[2]	–[2]	3.6067	13.6067	
H_2O^{++}(states of P7[1]) - $H_2O^+(1b_2^{-1}$ $^2B_2)$	–[2]	–[2]	2.2267	12.2267	< 9.0[3]
H_2O^{++}(states of P6[1]) - $H_2O^+(3a_1^{-1}$ $^2A_1)$	–[2]	–[2]	1.3667	11.3667	
H_2O^{++}(states of P6[1]) - $H_2O^+(1b_2^{-1}$ $^2B_2)$	–[2]	–[2]	–[2]	7.4267	
$H_2O^{++}(1b_2^{-2}$ $^1A_1$ (P5[1])) - $H_2O^+(1b_1^{-1}$ $^2B_1)$	–[2]	–[2]	–[2]	6.5067	
$H_2O^{++}(1b_2^{-2}$ $^1A_1$ (P5[1])) - $H_2O^+(3a_1^{-1}$ $^2A_1)$	–[2]	–[2]	–[2]	4.2667	
$H_2O^{++}(1b_2^{-2}$ $^1A_1$ (P5[1])) - $H_2O^+(1b_2^{-1}$ $^2B_2)$	–[2]	–[2]	–[2]	0.3267	

[1]For details see Table 4.2 and the text.
[2]Decay channel is closed.
[3]An estimate based of the ground state geometry of $(H_2O)_2$.

We have a completely different event in the case of $H_2O^{++}(2a_1^{-2}$ $^1A_1)H_2O$ which is depicted in Fig. 4.7 by the highest in energy horizontal line. This doubly ionized state has two holes in the $2s$ level of one of the water molecules. Thus, it may decay via dICD to the states shown by the repulsive curves below it. However, here a three electron process has to take place in which the two $2s$ vacancies are filled and another electron is ejected, since all possible final states have two $2p$ holes in one of the subunits and one $2p$ hole on the other. This three electron process is much less probable than the dICD. Nevertheless, it is expected to be the dominant relaxation mode of $H_2O^{++}(2a_1^{-2}$ $^1A_1)H_2O$ as the more efficient electronic decay processes are energetically forbidden.

ICD-electron spectra

Having arrived at the overall picture of the possible ICD channels we are now able to make a rough estimate of the energy distribution of the emitted ICD electrons. Assuming an instantaneous two step process, Auger followed by ICD, the wave packet of the decaying $H_2O^{++}H_2O$ states will have the same form as that of the ground state in $(H_2O)_2$ [65]. To this end we consider Gaussian type wave packets with a full width at half maximum (FWHM) of 0.5 Å centered at the equilibrium distance $R_{O-O} = 2.91$ Å. The form and the width of the wave packet are identical to those which one would obtain for a diatomic system in which each of the two particles have nuclear masses equal to the effective mass of H_2O lying on a potential curve like the one shown in Fig. 4.6(a). The nuclear wave functions of the decaying $H_2O^{++}H_2O$ states have been given weights according to the intensities of the peaks in the Auger spectrum of water (see Table 4.2) in order to have the correct population of the states decaying via ICD. Using equal decay rates for all of the open channels shown in Table 4.5, we have computed the e^-_{ICD} spectra depicted in Fig. 4.8(a). The black curve there represents the total energy distribution of the ejected ICD electrons and includes the contributions from the decay of both the singlet and triplet $H_2O^{++}H_2O$ states. It has one well pronounced maximum at 1 eV followed by a sharp drop in the intensity and oscillatory behavior in the range from about 6 to 12 eV.

These features can be better interpreted by inspecting the electron spectra of each of the ICD channels. The singlet and triplet states which undergo electronic decay represent 33% of the states populated by Auger in H_2O [55] and we expect similar populations in $(H_2O)_2$. The red and the dashed black lines in Fig. 4.8(a) describe the decay of $H_2O^{++}(2a_1^{-1}1b_1^{-1}\ ^1B_1)H_2O$ and $H_2O^{++}(2a_1^{-1}1b_2^{-1}\ ^3B_2)H_2O$, respectively. The ICD from these states can lead to the formation of the $H_2O^{++}H_2O^+$ states shown by the repulsive curves energetically below them. The partial ICD spectra (the red and the dashed black curves in the figure) exhibit two maxima, like the total spectrum, but drop to 0 at about 5 eV. In the case of $H_2O^{++}(2a_1^{-1}3a_1^{-1}\ ^1A_1)H_2O$, the situation is different as there are three singlet tricationic states below it. Therefore, its decay is characterized by a spectrum with a maximum close to 1 eV and a drop to 0 intensity just above 2.5 eV. The oscillatory behavior of the total ICD spectrum from 5 to 10 eV and 10 to 20 eV appears due to the relaxation of $H_2O^{++}(2a_1^{-1}1b_2^{-1}\ ^1B_2)H_2O$ and $H_2O^{++}(2a_1^{-2}\ ^1A_1)H_2O$, respectively. These states are much higher in energy and thus their decay produces ICD electrons with higher energies. For this reason, the spectra depicted in Fig. 4.8(a) by the blue and pink line spread to 10 and 20 eV, respectively. The appearance of maxima listed in Table 4.5 can be generally anticipated by inspecting the accumulation of the final tricationic PECs at

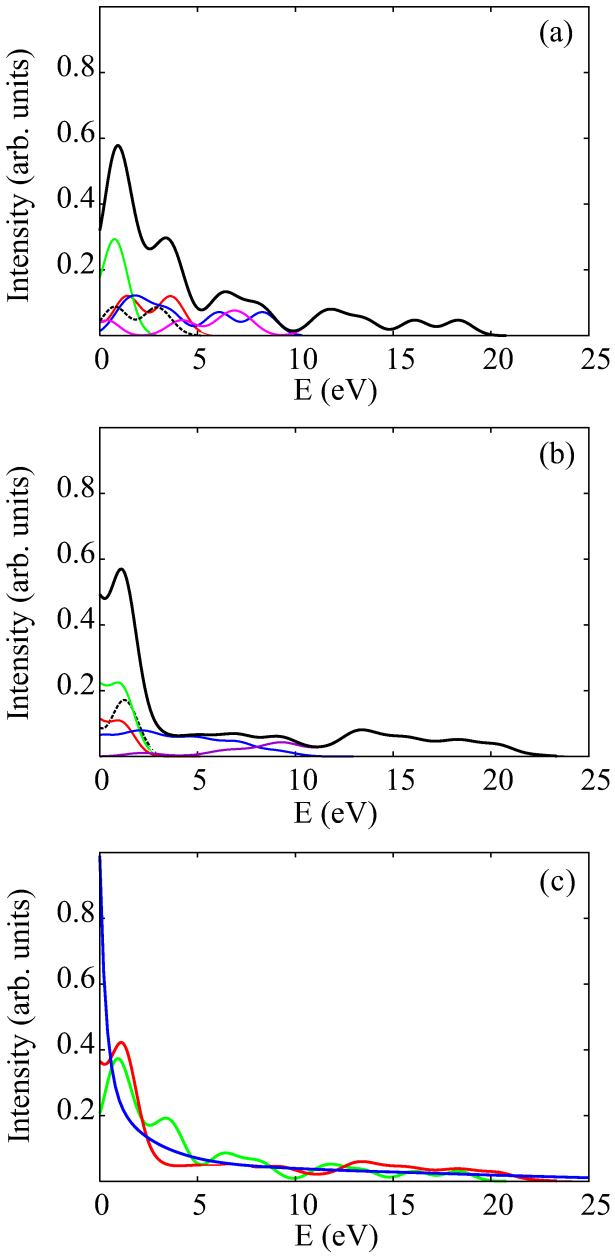

Figure 4.8: Estimated partial and total electron spectra of ICD following O1s Auger decay in $(H_2O)_2$ obtained via the three different approaches discussed in the text. (a) A PEC for each peak in the experimental Auger spectrum of H_2O is used. The PECs are adjusted to the maxima at the corresponding peaks in the experimental Auger spectrum [55]. (b) A PEC for every line in the *ab initio* computed double ionization spectrum and every combination of single and double ionization potentials for the final states is used. (c) A comparison between the total ICD-electron spectra of panel (a) – green line, panel (b) – red line, and that obtained via Eq. (4.1) using only the experimental Auger and photoionization spectra – blue line.
The color coding used in panels (a) and (b) is as follows: total spectrum – black curve, ICD from $H_2O^{++}(2a_1^{-1}1b_1^{-1}\ ^1B_1)H_2O$ – red curve, ICD from $H_2O^{++}(2a_1^{-1}3a_1^{-1}\ ^1A_1)H_2O$ – green curve, ICD from $H_2O^{++}(2a_1^{-1}1b_2^{-1}\ ^1B_2)H_2O$ – blue curve, ICD from $H_2O^{++}(2a_1^{-2}\ ^1A_1)H_2O$ – magenta curve, and the contribution to the ICD spectrum from the populated by Auger triplet states - black dashed curve.

the vertical transition for each decaying state, i.e., at the dashed vertical line in Fig. 4.7.

For computing the ICD-electron spectrum discussed above, we have represented the final states of the Auger process that can further decay via ICD by PECs constituted from the experimental data of the separated H_2O^{++} and H_2O contributions, see Tables 4.1 and 4.2. This rather simplified picture allows one to carry out the spectral analysis using experimental data of the separated constituents which is available, but does not account for the electron correlations in the dicationic and tricationic water dimer. The same procedure as the one discussed above can be implemented to compute the e^-_{ICD} spectrum using the single and triplet double ionization potentials of water which we have computed. Thus, for the computation of the spectra in Fig. 4.8(b) all of the decaying states listed in Table 4.2 with energy above 64 eV have been used, while the final states of the electronic decay were built as a combination of the H_2O^{++} states below 47 eV and the three $2p^{-1}$ type states of H_2O^+. Since a breakdown of the molecular orbital picture is observed in the higher lying dicationic states, $H_2O^{++}(2a_1^{-1}1b_2^{-1}\ ^1B_2)H_2O$ and $H_2O^{++}(2a_1^{-2}\ ^1A_1)H_2O$ give rise to sets of spectral lines. Thus, for computing the spectra of Fig. 4.8(b) 148 transitions in total have been taken into account, while the spectra shown in Fig. 4.8(a) was build from 21 transitions. Nevertheless, the total e^-_{ICD} spectrum presented in Fig. 4.8(b) has a very similar shape to that of Fig. 4.8(a). However, the large number of transitions included has led to smoothening of the curve and to a faster drop of the total intensity after a maximum at about 1 eV.

As we already pointed out, the electron correlation present in the dication gives rise to multitude of states that can be assigned to the same electron configuration forming an energy band. This effect has been partially included in the spectrum of Fig. 4.8(b), as two of the decaying dicationic configurations were represented by multiple lines. However, a more realistic result can be achieved if experimental spectra of the system before and after ICD are used. In this case the spectra of the emitted ICD-electrons $S(E)$ can be represented as a convolution of the spectra of the initial and the final for the decay states

$$S(E) = \frac{\int_0^\infty S_{in}(E - E')S_{fin}(E')dE'}{\int_0^E S_{fin}(E')dE'}, \tag{4.1}$$

where $S_{in}(E)$ is the spectrum of the system before the decay, in our case one-site doubly ionized water dimer, and $S_{fin}(E)$ is the spectrum of the system after the decay – two-site triply ionized water dimer in the present case. Note that in order to obtain correctly the weights of the different channels, one has to normalize to the initial population. Otherwise,

decay channels from higher in energy states that are always open will artificially get more weight than channels that are closed from some energy on. In the above expression this is accounted for by dividing the convolution by the appropriate energy-dependent wight.

Since, there are no experimental data available for the double and triple ionization of $(H_2O)_2$, we have resorted to the spectra of H_2O from Refs. [55–57]. For the spectrum of the one-site dicationic water dimer we have used the experimental Auger data. The spectrum of the $H_2O^{++}H_2O^+$ has been built via integration of the valence photoelectron [54] and Auger spectra [55] of water shifted by the energy of electrostatic repulsion between the ions. With the help of such obtained $H_2O^{++}H_2O$ and $H_2O^{++}H_2O^+$ spectra and Eq. (4.1) we have computed the total ICD-electron spectrum shown by a blue line in Fig. 4.8(c). It has a monotonously decreasing shape with a maximum at 0 eV and decreases to 10% of its maximal intensity at 6 eV. Inspecting Fig. 4.8(c), where the total spectra resulting from all three procedures discussed above are shown for comparison, we can conclude that although having different shapes, the three approaches suggest that the majority of electrons emitted in an ICD following Auger decay in water dimer will have kinetic energies between 0 and 8 eV. Thus, the ICD following Auger decay in water also appears as a source of LEEs. Moreover, more than one third of all the states populated by Auger decay in water will further undergo ICD and produce low-energy electrons.

4.2 ICD and the other electronic decay processes initiated by inner-valence ionization of $H_2O\cdots HCHO$, $H_2O\cdots H_2CNH$, $H_2O\cdots NH_3$, $NH_3\cdots H_2O$, $H_2O\cdots H_2S$, $H_2S\cdots H_2O$, and $H_2O\cdots H_2O$

The ICD of the water dimer was analyzed in the previous section, while additional information about the ICD electron spectrum of $(H_2O)_2$ can be found in Refs. [11, 109]. Thus, we shall now use $H_2O\cdots H_2O$ to show the influence of the hydrogen bonding on the electronic spectra of the two water units in it. The single ionization spectra of H_2O with the relaxed geometry of an isolated molecule, with the geometry of the proton-donor in $H_2O\cdots H_2O$, and that of the proton-acceptor in $H_2O\cdots H_2O$ are depicted in panels (a), (b), and (c) of Fig. 4.9, respectively. One immediately sees that the three spectra are very similar, which is an expected result, since the difference in the geometries of the species is insignificant. However, as shown in Fig. 4.5(b), the position of the spectral lines belonging to the p-donor and p-acceptor molecules in the dimer is grater. This is an additional proof that the electrostatic interaction of the two units in $H_2O\cdots H_2O$ has a stronger effect on the ionization spectra then the change the geometry of the water moleclues due to the hydrogen bonding.

The optimized geometries of $H_2O\cdots HCHO$, $H_2O\cdots H_2CNH$, $H_2O\cdots NH_3$, $NH_3\cdots H_2O$, $H_2O\cdots H_2S$, $H_2S\cdots H_2O$, and $H_2O\cdots H_2O$ are depicted in Fig. 4.10. All of the systems are in C_s symmetry. The atoms of $H_2O\cdots H_2CNH$ are semiplanar, while the other six species have their two molecules lying in two perpendicular planes. The hydrogen bonding has a comparatively weak impact on the geometry of the individual subunits and their structure is only slightly different form those of the isolated molecules. The technical details of the methods used to optimize the structures and to calculate the single- and double-ionization potentials of the studied set of systems can be found in Section 2.2.4.

The relaxed geometries shown in in Fig. 4.10 have certain peculiarities. The weakest intermolecular bonding is that of $H_2O\cdots H_2S$ (Note that throughout the text, we write the proton donor first and the proton acceptor second in the chemical formulae of the bimolecular systems.). There, the distance between the H atom donated by the oxygen in water and the sulfur atom of the sulfide is 2.515 Å. In the structure in which the sulfur atom donates the hydrogen, i.e., in $H_2S\cdots H_2O$, the hydrogen bond is 2.098 Å and thus shorter by as much as 0.4 Å than in $H_2O\cdots H_2S$. In fact, $H_2O\cdots H_2S$ and $H_2S\cdots H_2O$ exhibit the largest difference in the length of the intermolecular bond of all studied $X\cdots Y$ and

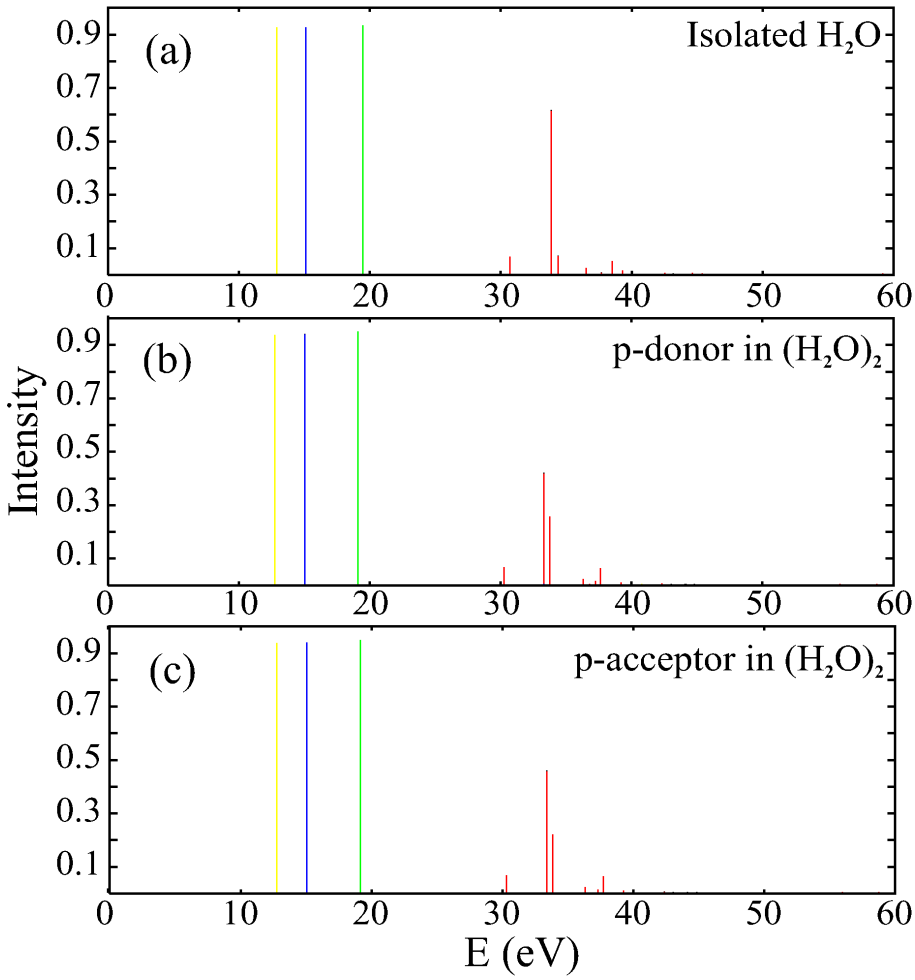

Figure 4.9: Single ionization spectra of H_2O with: (a) the relaxed geometry of an isolated molecule; (b) the geometry of the proton-donor in $H_2O\cdots H_2O$, and (c) the geometry of the proton-acceptor in $H_2O\cdots H_2O$. For further details see the text.

Y$\cdots$X pairs. The shortest hydrogen bond is that of $H_2O\cdots H_2CNH$. Its length of 1.942 Å is very close to that of $H_2O\cdots H_2O$. Interestingly, the largest elongation of the O-H bond in a proton donating H_2O is observed in $H_2O\cdots NH_3$. This results from the orientation of the two molecule positioning the three atoms (O, H, and N), which determine the hydrogen bond, on a line. Nevertheless, even here, the electrostatic attraction between the proton and the partial negative charge on the N atom elongates the O-H bond by only 0.014 Å compared to isolated H_2O [110].

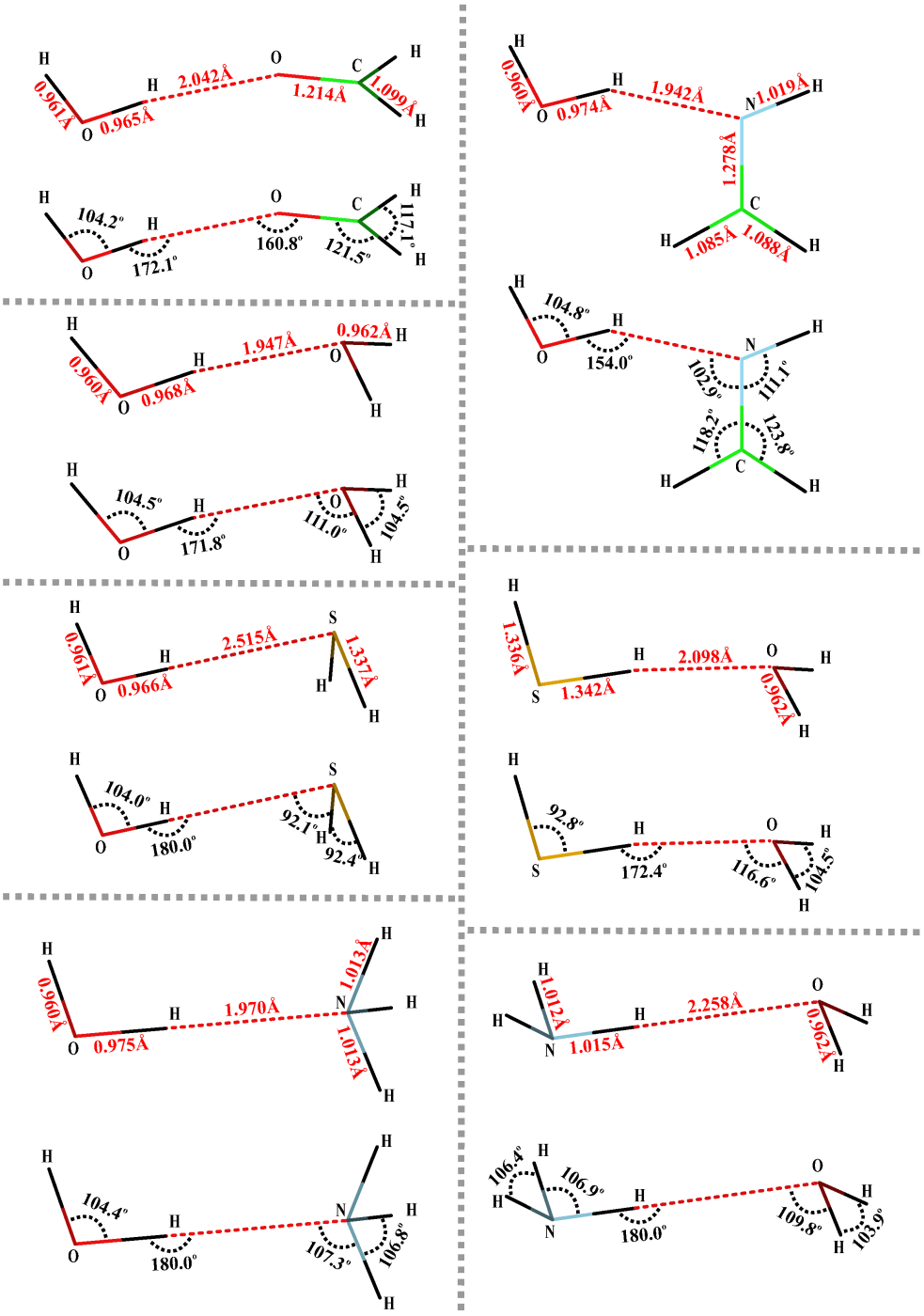

Figure 4.10: Optimized geometries of $H_2O \cdots HCHO$, $H_2O \cdots H_2CNH$, $H_2O \cdots NH_3$, $NH_3 \cdots H_2O$, $H_2O \cdots H_2S$, $H_2S \cdots H_2O$, and $H_2O \cdots H_2O$ (p-donor $\cdots$ p-acceptor). All of the investigated systems exhibit the C_S symmetry with their p-donor and the p-acceptor molecules lying in perpendicular planes, except for H_2O - H_2CNH which has its atoms semiplanar. For further details see the text.

4.2.1 $H_2O\cdots HCHO$

We shall closely examine one of the selected systems, namely the water-formaldehyde cluster ($H_2O\cdots HCHO$), as it exhibits all decay modes that are characteristic for the other species. The most important features of the investigated systems – the possible electronic decay channels and the energies of the secondary emitted electrons, are summarized in Table 4.6. There, an estimate of the KER, can also be found. Note that the KER value given is calculated as the Coulomb repulsion of two elementary charges at a distance equal to that between the centers of mass of the hydrogen bonded subunits at the equilibrium geometry of the cluster. Thus, the possible energy transferred into the internal (vibrational and rotational) degrees of freedom of the ions is not accounted for. One should expect that the KER to be observed in an experiment will have slightly lower values, as shown in Section 4.1 (see also Refs. [14] and [103]), where the back-to-back flight of the two ions in the Coulomb explosion of $H_2O^+\cdots H_2O^+$ is studied.

The single- and double-ionization spectra of $H_2O\cdots HCHO$ are depicted in panels (a) and (b) of Fig. 4.11, respectively. They reflect the electronic degrees of freedom and are computed using the procedures described in section 2.2.4. The IPs in Fig. 4.11(a) can be divided into two groups. Those with energies below 20 eV are states corresponding to ionization out of the outer-valence shell. They lie below the double-ionization threshold of the system of 25.3 eV, which is defined by the lowest in energy line in panel (b), and thus cannot decay by electron emission. Their energies and spectral intensities are given in Table 4.7. The spectral lines above 20 eV are the states stemming from the inner-valence ionization of the system. Most of these states are above the double-ionization threshold and thus can participate in an electronic decay. These are the states that we will concentrate on in the present study. In Fig. 4.11(a) these states are depicted with different colors indicating the different atoms on which the inner-valence vacancy is mainly localized. These are termed as: $2s$-type lines of carbon plotted in blue, $2s$-type lines of oxygen in water shown in green, and $2s$-type lines of oxygen in formaldehyde depicted in red. The two sets of $O2s^{-1}$ states are typical examples of the "breakdown of the molecular orbital picture of ionization" [104] resulting from the strong correlation between the electrons. They are typical electronically decaying states and their maxima in the electronic spectra will be positioned at the points of the computed ionization potentials bearing the highest spectral intensities of the corresponding groups. Those states are marked with arrows in Fig. 4.11(a).

The lowest in energy dicationic state is at 25.3 eV and relates to $H_2O^+\cdots HCHO^+$. However, the IP corresponding to the state stemming from the carbon $2s$ ionization has

Table 4.6: The possible inter- and intra-molecular decay modes of the inner-valence (iv) ionized states of the studied species. Given are the products of decay, the energies of the emitted secondary electrons, and the positions of the maxima in the kinetic energy release (KER) spectra of the dissociating systems. The abbreviations used are as follows: intermolecular Coulombic decay (ICD), electron-transfer mediated decay (ETMD), and autoionization (AI). For further details see the text and the Supplementary information.

H-bonded system (p-donor$\cdots$p-acceptor)	Processes and energies				
	Open channels after the iv ionization of the:		Products of decay	Energy range of the emitted e^- [eV]	Maximum in the KER spectrum [eV]
	p-donor	p-acceptor			
$H_2O\cdots HCHO$	ICD		H_2O^+ / $HCHO^+$	0 – 8	$\propto$ 4.4
	ETMD[a]		$H_2O\cdots HCHO^{++}$	$\propto$ 0.0[b]	-
		AI	$H_2O\cdots HCHO^{++}$	0 – 4	-
		ICD	H_2O^+ / $HCHO^+$	0 – 10	$\propto$ 4.4
$H_2O\cdots H_2CNH$	ICD		H_2O^+ / H_2CNH^+	0 – 6	$\propto$ 4.9
	ETMD[a]		$H_2O\cdots H_2CNH^{++}$	0 – 2[b]	-
		AI	$H_2O\cdots H_2CNH^{++}$	$\propto$ 0.0[b]	-
		ICD	H_2O^+ / H_2CNH^+	0 – 4	$\propto$ 4.9
$H_2O\cdots NH_3$	ICD		H_2O^+ / NH_3^+	0 – 7	$\propto$ 4.9
		ICD	H_2O^+ / NH_3^+	0 – 4	$\propto$ 4.9
$NH_3\cdots H_2O$	ICD		NH_3^+ / H_2O^+	0 – 4	$\propto$ 4.4
		ICD	NH_3^+ / H_2O^+	0 – 10	$\propto$ 4.4
		ETMD[a]	$NH_3^{++}\cdots H_2O$	0 – 2	-
$H_2O\cdots H_2S$	ICD		H_2O^+ / H_2S^+	0 – 9	$\propto$ 4.1
	ETMD[a]		$H_2O\cdots H_2S^{++}$	0 – 3	-
$H_2S\cdots H_2O$		ICD	H_2S^+ / H_2O^+	0 – 11	$\propto$ 4.2
		ETMD[a]	$H_2S^{++}\cdots H_2O$	0 – 5	-
$H_2O\cdots H_2O$[c]	ICD		H_2O^+ / H_2O^+	0 – 10	4.0[d]
		ICD	H_2O^+ / H_2O^+	0 – 11	4.0[d]

[a]Process with low probability.

[b]The energy difference is small and could be within or close to the computational error, i.e. the channel might be closed. Note that the process might be accomplished through one of the lower in intensity, but higher in energy satellites of the decaying state.

[c]See Ref. [111] where ICD and related processes following inner-valence and core ionization of $H_2O\cdots H_2O$ are studied.

[d]The experimental and the computed values are taken from Refs. [14] and [103], respectively.

energy of 21.9 eV and hence it cannot take part in an electronic decay process. In contrast, the states corresponding to ionization out of the O2s-type orbitals of both the water and the formaldehyde subunits are above the double-ionization threshold and thus can further decay by electron emission. The lowest in energy dicationic state is of a two-site character ($H_2O^+\cdots HCHO^+$) and, therefore, the decay channels are of intermolecular nature, i.e. the respective decay process is ICD.

Let us discuss first the decay process initiated by inner-valence ionization of the water molecule. The lowest in energy one-site dicationic state having two holes on the water molecule is at 36.6 eV (see the lowest in energy green line in Fig. 4.11(b)), i.e. the inner-valence ionized water cannot autoionize. All open decay channels are to two-site

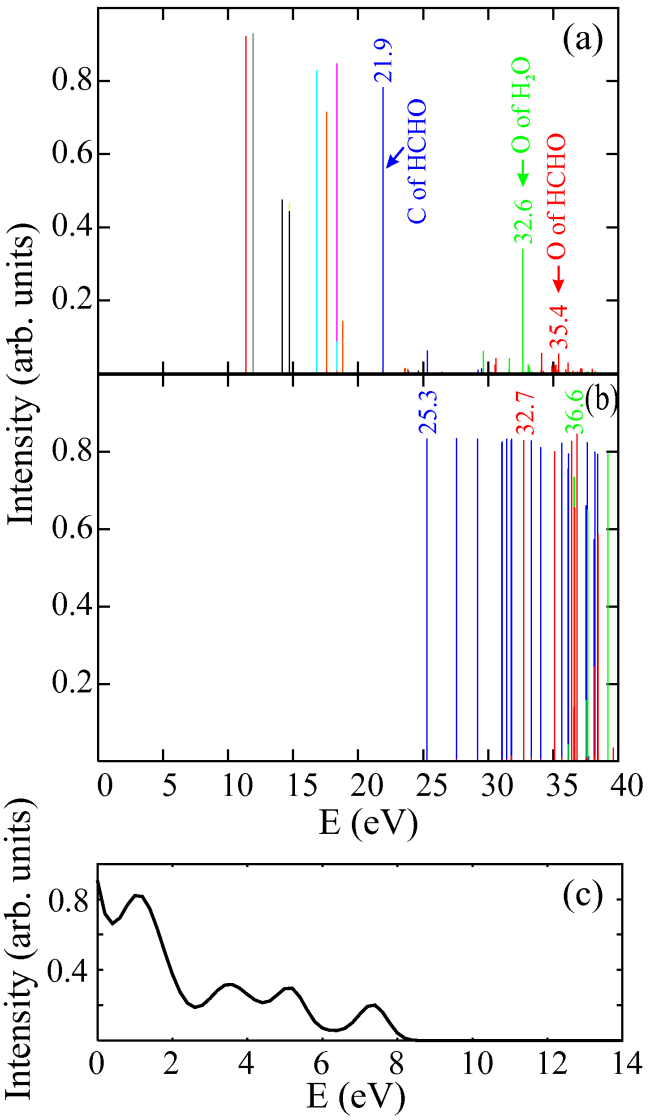

Figure 4.11: Panels (a) and (b): Computed single- and double-ionization spectra of $H_2O\cdots HCHO$ in its ground state equilibrium geometry, respectively. Panel (c): The spectrum of the ICD electron. The colors in panel (a) indicate the different atoms on which the inner-valence hole is mainly localized, while the colors in panel (b) indicate the different types of the dicationic states: the two-site states, $H_2O^+\cdots HCHO^+$, are depicted in blue, the one-site states of the type $H_2O^{++}\cdots HCHO$ are depicted in green, and the one-site states of the type $H_2O\cdots HCHO^{++}$, are depicted in red. For further details see the text and the Supplementary information.

dicationic states (blue lines in Fig. 4.11(b)). Thus, if an electron is removed from the O2s-type orbital of water, an electron from a higher lying orbital of H_2O^+ will fill the O2s vacancy and an electron from the neighboring HCHO will be ejected. The process can be written in short as:

Step 1 (inner-valence ionization):

$$H_2O\cdots HCHO \xrightarrow{h\nu} H_2O^+(2s^{-1})\cdots HCHO + e^-_{photo},$$

Step 2 (ICD):

$$H_2O^+(2s^{-1})\cdots HCHO \longrightarrow H_2O^+(2p^{-1})\cdots HCHO^+(2p^{-1}) + e^-_{ICD},$$

Table 4.7: Calculated values of the single-ionization potentials of the outer-valence shell of $H_2O\cdots HCHO$, their energies and intensities, as well as the contribution of the corresponding $(MO)^{-1}$ configuration to each of the ionic states.

$H_2O\cdots HCHO$ in symmetry C_s			
Energy [eV]	Intensity	Contribution of the $(MOs)^{-1}$ to the ionic state	
		MOs	Coefficients[a]
11.3906	0.925	$3a''$	-0.96
11.9385	0.930	$2a''$	0.96
14.1780	0.932	$10a'$	-0.69
		$9a'$	0.67
14.7183	0.910	$9a'$	0.68
		$10a'$	0.67
16.8247	0.912	$8a'$	0.91
		$7a'$	-0.28
17.5541	0.723	$1a''$	0.85
		$3a''$	-0.09
18.3737	0.935	$7a'$	0.92
		$8a'$	0.30
18.8229	0.144	$1a''$	0.38

[a]Coefficients of the ACD(3) eigenvectors with values above 0.05 are given.

Step 3 (Coulomb explosion):

$$H_2O^+(2p^{-1})\cdots HCHO^+(2p^{-1}) \longrightarrow H_2O^+(2p^{-1}) + HCHO^+(2p^{-1}).$$

where the final hole on the water molecule will be in an orbital consisting mainly of the $2p$ MO of the oxygen, while the hole on formaldehyde will be in an orbital constructed from the $2p$ MOs of the carbon and oxygen.

Since the hydrogen bond is very weak, the repulsion between the two positive charges produced by the ICD process on the two hydrogen bonded species will lead to a Coulomb explosion of the system. The kinetic energy release of the exploding H_2O^+ and $HCHO^+$ can be estimated assuming that ICD is much faster than the nuclear motion of the heavier atoms in the cluster. Considering the 3.3 Å distance between the centers of mass of the hydrogen bonded H_2O and HCHO, a value of 4.4 eV for the KER is expected. However, as mentioned above, the Coulomb repulsion energy can also be partly distributed among the rotational and vibrational degrees of freedom of the ions produced and thus in reality

the maximum in the KER spectrum would appear at lower energies. In the case of the Coulomb explosion following the ICD in $H_2O\cdots H_2O$, this effect yields a decrease of the KER compared to the rigid species approximation by about 0.6 eV, see Section 4.2.1.

The ICD in $H_2O\cdots HCHO$ initiated by inner-valence ionization of the water molecule is schematically represented in the left-hand-side panels of Fig. 4.12. The right-hand-side panels of the same figure show the ICD process that might take place in a carbonyl containing fragment of the enzyme lysozyme hydrogen bonded with H_2O. The ultrafast decay by ICD should be observed in both the water-formaldehyde cluster and the surrounded by water biochemical macromolecule. The mechanism of the decay will be the same in both cases, as also found to be in water dimer and large water clusters [14, 15]. However, due to the much larger number of vibrational and rotational modes in which the excess energy of the final states can be distributed, the production of the two positively charged species will not necessarily lead to a Coulomb explosion and disintegration of the macromolecule but probably rather to a local bond breaking and to a 'heating up' of the system. The low-energy electrons and the radicals produced are expected to further induce damages in the biosystem.

Let us now turn to the question of the energy distribution of the emitted ICD electrons. To compute a decay-electron spectrum, one needs first to construct the full potential energy hypersurfaces of the initial state, the intermediate decaying states, and the final states. In the case of the discussed ICD these are the neutral ground state, the singly ionized states, and the doubly ionized states of the system. In addition, one needs to compute the partial decay widths of each decaying state as a function of the nuclear degrees of freedom and perform nuclear wavepacket dynamics calculations to describe the decay process. Even for diatomics such calculations are notoriously difficult [112]. For polyatomics they are far beyond reach of any current theoretical method. However, our experience with the ICD-electron spectrum of water dimer, discussed in the previous section, shows that only the data from the single- and double-ionization spectra of the system in its equilibrium geometry suffices to obtain ICD-electron spectra in a fairly good agreement with the experimental results [14]. This can be done by using spectral envelopes to account for the vibrational structure of the initial and final for the decay states as described in Section 4.1.2. Here, as before, the correct weights of the different channels, are normalized to the initial population, since, otherwise, decay channels from higher in energy states that are always open and will artificially get more weight than channels that are closed from some energy on, see Eq. 4.1.

The kinetic-energy distribution of the electrons ejected in the ICD of $H_2O\cdots HCHO$

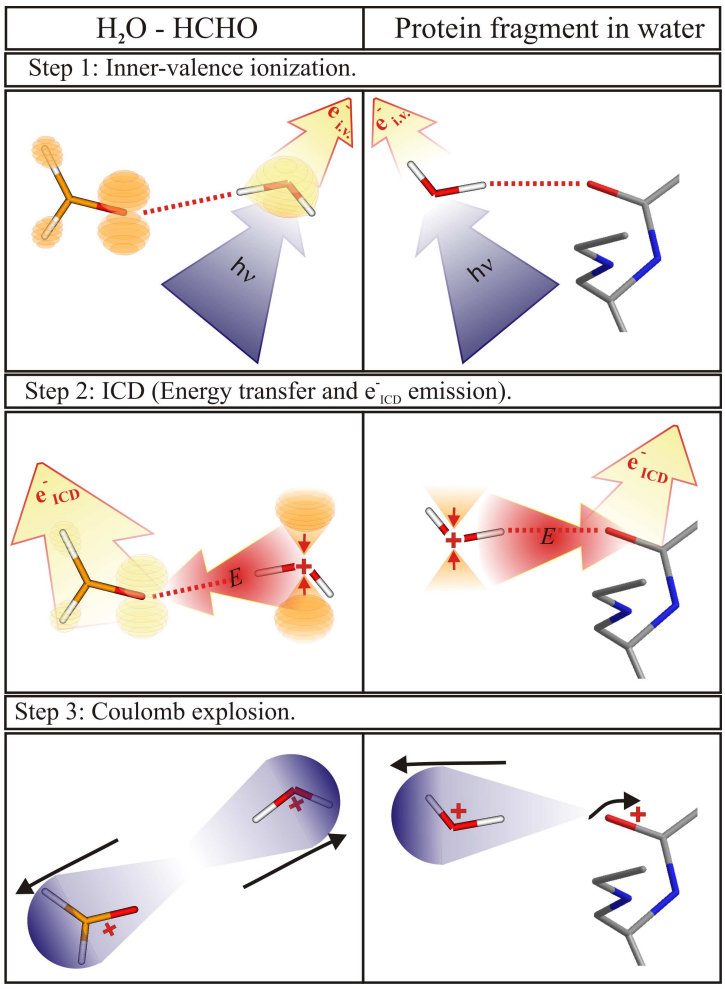

Figure 4.12: Schematic representation of the intermolecular Coulombic decay in $H_2O\cdots HCHO$ (left) and in a H_2O interacting with a fragment from the enzyme lysozyme (right). The ICD process is initiated by an inner-valence ionization of the water molecule (upper panels). The created vacancy is filled by an electron from a higher lying electronic shell of the same unit and a secondary electron is emitted from the neighboring unit (middle panels). In the case of $H_2O\cdots HCHO$ a Coulomb explosion follows, as the two positively charged species fly apart, and a bond breaking and a restructuring of the macromolecule follows in the case of the lysozyme-water complex (lower panels). The produced low-energy ICD electrons and radicals may induce further damages of the biosystem. For more details, see text.

obtained via the above procedure using a FWHM of 0.7 eV is shown in Fig. 4.11(c). The spectrum has a maximum at 0 eV followed by a drop in the intensity suggesting that the emitted e^-_{ICD} will have energies between 0 and 8 eV with more than half of them with energy below 3 eV. We would like to note that the spectrum is not very sensitive to the particular choice of the width of the Gaussian envelopes. Choosing smaller FWHM values will lead to a more structured spectrum, while larger ones will lead to a smoother drop off of the electron-energy distribution. Most likely a measured ICD spectrum will be less structured than the one depicted in Fig. 4.11(c) as the comparison between the ICD-electron spectrum of the water dimer computed via the above procedure (the green line in Fig. 4.13(a) and the one obtained experimentally [14] (Fig. 4.13(b)) shows. Incleasing the FWHM to 1.5 eV smoothens the curve for the ICD electron distribution (see the black line in Fig. 4.13(a)), thus making its shape closer to the observed one. Note that the electron yield between 8 and 12 eV in the experiment is mainly attributed to the photo-electrons accompanying the inner-valence ionization initiating the electronic decay.

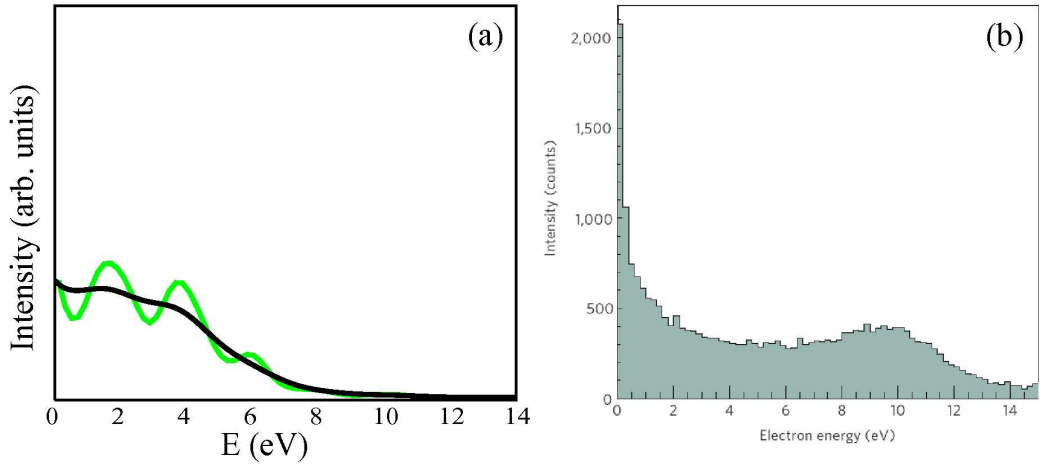

Figure 4.13: (a) Spectra of the emitted e^-_{ICD} in the ICD of $(H_2O)_2$ computed implementing equation 4.1 and the spectral lines in Fig. 4.4(a); the green and the black line are obtained using FWHM of 0.7 and 1.5 eV, respectively. For further details see Tables 4.1, 4.2, and the text, as well as Refs. [11,109]. (b) Measured electron kinetic energy for break-up of the water dimer into H_2O^+/H_2O^+, the figure is taken from Ref. [14]. Note that the electron yield between 8 and 12 eV is mainly attributed to the photo-electrons accompanying the inner-valence ionization initiating the ICD.

The process described above is characterized by a transfer of energy from the initially ionized unit to its neighbor. This is the dominant relaxation mode of $H_2O^+(2s^{-1})\cdots HCHO$ due to its very high efficiency. Nevertheless, we shall discuss the possibility of electron-transfer mediated decay in the water-formladehyde cluster for completeness.

According to our calculations, the position of the main line of $H_2O^+(2s^{-1})\cdots HCHO$ is just one tenth of eV below that of the lowest in energy $H_2O\cdots HCHO^{++}$ state. This doubly ionized *one-site* state of $H_2O\cdots HCHO$ in which two electrons are removed from the formaldehyde molecule is at 32.7 eV, see Fig. 4.11(b). One has to bear in mind that this small energy difference is within the error of the computational methods used, and even if we take into account that the lines shown in Fig. 4.11(b) will acquire widths due to the nuclear degrees of freedom, as discussed above, we cannot definitely say whether ETMD takes place here. For that, even more accurate calculations would be necessary. Nevertheless, we would like to briefly discuss our results on ETMD noting that it is beyond doubt possible for other members of our set of molecules (see Table 4.6 and text below). After the creation of a vacancy in an O2s-type MO of H_2O, an electron from the neighboring subunit can fill it and another (ETMD) electron can be ejected from the

initially neutral HCHO. In short:

$$\mathrm{H_2O^+}(2s^{-1})\cdots\mathrm{HCHO} \longrightarrow \mathrm{H_2O}\cdots\mathrm{HCHO^{++}}(2p^{-2}) + e^-_{ETMD}.$$

Here, the energy of the emitted electron is expected to be close to 0 eV and the created $\mathrm{H_2O}\cdots\mathrm{HCHO^{++}}$ will, of course, not undergo a Coulomb explosion. The ETMD process will compete with the much more probable ICD and thus only a minor fraction of the initially populated $\mathrm{H_2O^+(2s^{-1})}\cdots\mathrm{HCHO}$ will undergo an electron-transfer mediated decay.

Let us now turn to the processes that can be initiated by inner-valence ionization of the formaldehyde, namely the $\mathrm{H_2O}\cdots\mathrm{HCHO^+(2s^{-1}}$ of O) states. As seen in Fig. 4.11(a) the most intense respective line in the ionization spectrum is at 35.4 eV and is higher in energy than both the $\mathrm{H_2O^+}\cdots\mathrm{HCHO^+}$ and $\mathrm{H_2O}\cdots\mathrm{HCHO^{++}}$ thresholds shown in Fig. 4.11(b). This means that the inner-valence ionized HCHO can undergo intermolecular decay, i.e. ICD, as well as an intramolecular decay, i.e. autoionization. Starting from the inner-valence (O2s-type) ionization of formaldehyde
Step 1 (inner-valence ionization):

$$\mathrm{H_2O}\cdots\mathrm{HCHO} \xrightarrow{h\nu} \mathrm{H_2O}\cdots\mathrm{HCHO^+}(2s^{-1}\text{ of O}) + e^-_{photo},$$

the system can undergo the following decay processes:
Step 2 (autoionization and ICD):

$$\mathrm{H_2O}\cdots\mathrm{HCHO^+}(2s^{-1}ofO) \begin{cases} \nearrow & \mathrm{H_2O}\cdots\mathrm{HCHO^{++}}(2p^{-2}) + e^-_{autoion.}. \\ \searrow & \mathrm{H_2O^+}(2p^{-1}) + \mathrm{HCHO^+}(2p^{-1}) + e^-_{ICD}. \end{cases}$$

The formation of $\mathrm{H_2O}\cdots\mathrm{HCHO^{++}}$ by autoionization will be accompanied by the emission of a secondary electron with energies between 0 and 4 eV, while the formation of $\mathrm{H_2O^+}\cdots\mathrm{HCHO^+}$ by ICD will produce electrons with energies between 0 and 10 eV. In order to estimate the relative importance of these intra- and inter-molecular decays, a detailed computation of the decay rates for these processes is needed which is currently not possible. In general, intramolecular electronic decay processes are expected to be faster than the intermolecular ones and, thus, we assume the autoionization process to outperform its intermolecular competitor. However, since the produced ionic fragments by autoionization and ICD differ, the two electronic decay modes could be, in principle, separated and their weights measured in an experiment.

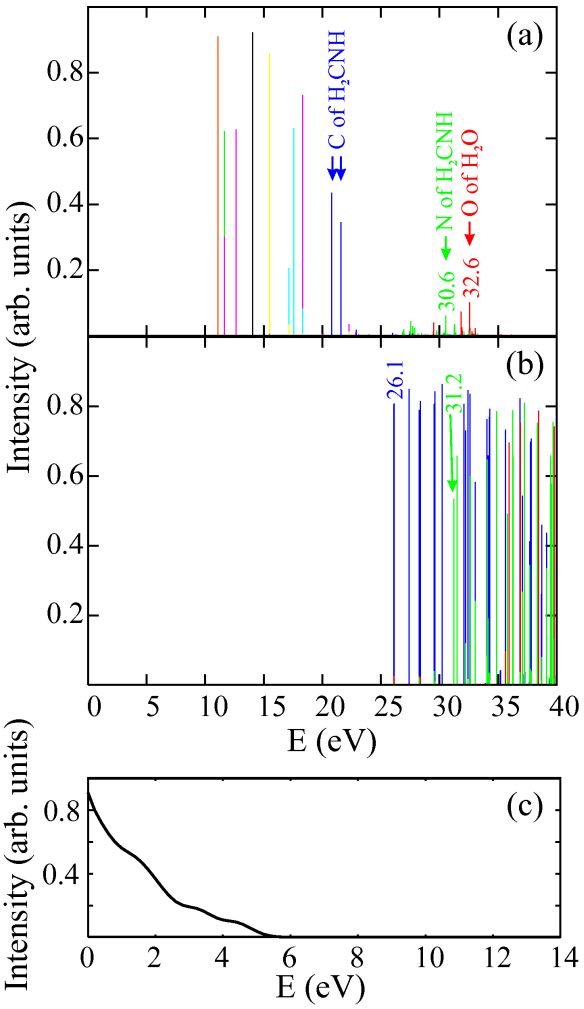

Figure 4.14: Panels (a) and (b): Computed single- and double-ionization spectra of $H_2O \cdots H_2CNH$ in its ground state equilibrium geometry, respectively. Panel (c): The spectrum of the ICD electron. The colors in panel (a) indicate the different atoms on which the inner-valence hole is mainly localized, while the colors in panel (b) indicate the different types of the dicationic states: the two-site states, $H_2O^+ \cdots H_2CNH^+$, are depicted in blue, the one-site states of the type $H_2O \cdots H_2CNH^{++}$ are depicted in green, and the one-site states of the type $H_2O^{++} \cdots H_2CNH$, are depicted in red.

4.2.2 $H_2O \cdots H_2CNH$

The presence of the π-bond in $H_2O \cdots H_2CNH$ makes its properties similar to the water-formaldehyde cluster studied in the previous section. In particular, low single- and double-ionization thresholds are a characteristic feature of the system and the IPs of the carbon 2s-type states are below the double-ionization threshold of $H_2O \cdots H_2CNH$ (see Table 4.8 and Fig.4.14). The spectral lines stemming from the ionization of the O2s-type MO have energies above 29 eV with the most intense line at 32.6 eV. These states are well above the lowest $H_2O^+ \cdots H_2CNH^+$ state located at 26.1 eV and thus an ICD process can be initiated by inner-valence ionization of the water molecule.

The $H_2O^+(2s^{-1}) \cdots H_2CNH$ could also undergo ETMD, but it will compete with the much more efficient ICD and can be neglected. ICD processes can be initiated also from inner-valence ionization of H_2CNH, namely from the state $H_2O \cdots H_2CNH^+(2s^{-1}$ of N). The spectral lines related to the ionization of the N2s orbital are above 27 eV with the

Table 4.8: Calculated values of the single ionization potentials of the outer-valence shell of $H_2O\cdots H_2CNH$, their energies and intensities, as well as the contribution of the $(MOs)^{-1}$ configuration to each of the ionic states. For further details about the computational method see Section 2.2.4 and the references therein.

$H_2O\cdots H_2CNH$ in symmetry C_s			
Energy [eV]	Intensity	Contribution of the $(MOs)^{-1}$ to the ionic state	
		MOs	Coefficients[a]
11.1105	0.914	$11a^{'}$	-0.95
		$9a^{'}$	0.05
11.6344	0.924	$1a^{''}$	0.79
		$2a^{''}$	-0.55
12.6476	0.930	$2a^{''}$	-0.79
		$1a^{''}$	-0.55
14.0567	0.925	$10a^{'}$	-0.96
15.4737	0.877	$9a^{'}$	-0.93
		$7a^{'}$	0.10
		$11a^{'}$	-0.08
17.1475	0.350	$8a^{'}$	-0.45
		$7a^{'}$	-0.32
		$9a^{'}$	-0.19
17.5703	0.647	$8a^{'}$	-0.79
		$7a^{'}$	-0.10
		$9a^{'}$	0.07
18.3116	0.822	$7a^{'}$	0.86
		$8a^{'}$	-0.29
		$9a^{'}$	0.08

[a]Coefficients of the ACD(3) eigenvectors with values above 0.05 are given.

most intense line at about 30.6 eV. Although our computations show that the channel for autoionization is closed for the most intense $H_2O\cdots H_2CNH^+(2s^{-1}$ of N) line, for some higher lying states populated by the ionization of the nitrogen $2s$-type MO the autoionization channel is open. The decay processes in the water-imine system can be written in short as:

Step 1 (inner-valence ionization):

$$H_2O\cdots H_2CNH \xrightarrow{h\nu} H_2O^+(2s^{-1})\cdots H_2CNH + e^-_{photo},$$

Step 2 (ICD):

$$H_2O^+(2s^{-1})\cdots H_2CNH \longrightarrow H_2O^+(2p^{-1})\cdots H_2CNH^+(2p^{-1}) + e^-_{ICD}, or$$

Step 2 ((ETMD), a low intensity process):

$$H_2O^+(2s^{-1})\cdots H_2CNH \longrightarrow H_2O\cdots H_2CNH^{++}(2p^{-2}) + e^-_{ETMD}.$$

Step 1 (inner-valence ionization):

$$H_2O\cdots H_2CNH \xrightarrow{h\nu} H_2O\cdots H_2CNH^+(2s^{-1}ofN) + e^-_{photo},$$

Step 2 (ICD):

$$H_2O\cdots H_2CNH^+(2s^{-1}ofN) \longrightarrow H_2O^+\cdots H_2CNH^+ + e^-_{ICD}, or$$

Step 2 (AI), the channel might be closed:

$$H_2O\cdots H_2CNH^+(2s^{-1}ofN) \longrightarrow H_2O\cdots H_2CNH^{++} + e^-_{AI}.$$

The electronic spectrum of the emitted e^-_{ICD} in the decay of the singly ionized states of $H_2O\cdots H_2CNH$ is depicted in Fig. 4.14(c). It is characterized by a monotonous drop of intensity in the energy range from 0 to 6 eV. Here, as well as in the other systems which we have investigated, the ICD initiated in the water molecule contributes with electrons with energies of the entire spectrum, while the inner-valence ionization of the imine unit of the cluster will lead to the formation of e^-_{ICD} of 5 eV maximum. This is another proof that the electronic structure of water and its comparatively high single ionization potentials make H_2O an ideal promotor of intermolecular electronic processes.

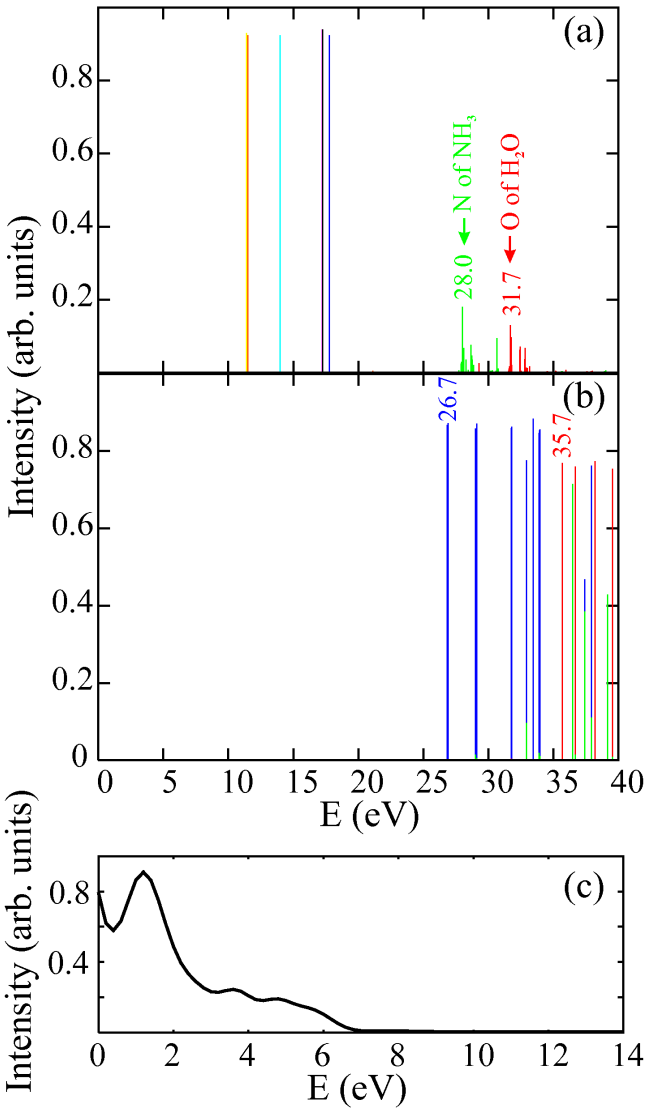

Figure 4.15: Panels (a) and (b): Computed single- and double-ionization spectra of $H_2O \cdots NH_3$ in its ground state equilibrium geometry, respectively. Panel (c): The spectrum of the ICD electron. The colors in panel (a) indicate the different atoms on which the inner-valence hole is mainly localized, while the colors in panel (b) indicate the different types of the dicationic states: the two-site states, $H_2O^+ \cdots NH_3^+$, are depicted in blue, the one-site states of the type $H_2O \cdots NH_3^{++}$ are depicted in green, and the one-site states of the type $H_2O^{++} \cdots NH_3$, are depicted in red.

4.2.3 $H_2O \cdots NH_3$

Let us turn now to $H_2O \cdots NH_3$, see panels (a) and (b) in Fig. 4.15. Our computations show that for this system the ICD process can be initiated by inner-valence ionization of both the H_2O and NH_3 subunits. The most intense line of $H_2O^+(2s^{-1}) \cdots NH_3$ is at 31.7 eV and that of $H_2O \cdots NH_3^+(2s^{-1})$ at 28.0 eV, while the lowest in energy doubly ionized two-site state is positioned at 26.7 eV. There are no ETMD or autoionization channels open, thus ICD appears as the only possible electronic decay mode. The sputum of the emitted electrons is show in Fig. 4.15(c) and the processes can be written as:

Step 1 (inner-valence ionization):

$$H_2O \cdots NH_3 \xrightarrow{h\nu} H_2O^+(2s^{-1}) \cdots NH_3 + e^-_{photo},$$

Table 4.9: Calculated values of the single ionization potentials of the outer-valence shell of $H_2O\cdots NH_3$, their energies and intensities, as well as the contribution of the $(MOs)^{-1}$ configuration to each of the ionic states. For further details about the computational method see Section 2.2.4 and the references therein.

$H_2O\cdots NH_3$ in symmetry C_s			
Energy [eV]	Intensity	Contribution of the $(MOs)^{-1}$ to the ionic state	
		MOs	Coefficients[a]
11.4248	0.930	$8a^{'}$	-0.96
11.5087	0.924	$2a^{''}$	-0.96
13.9853	0.925	$7a^{'}$	0.96
17.2147	0.940	$6a^{'}$	-0.97
17.2483	0.940	$1a^{''}$	0.97
17.7937	0.924	$5a^{'}$	-0.96

[a]Coefficients of the ACD(3) eigenvectors with values above 0.05 are given.

Step 2 (ICD):

$$H_2O^+(2s^{-1})\cdots NH_3 \longrightarrow H_2O^+(2p^{-1})\cdots NH_3^+(2p^{-1}) + e^-_{ICD}.$$

Step 1 (inner-valence ionization):

$$H_2O\cdots NH_3 \xrightarrow{h\nu} H_2O\cdots NH_3^+(2s^{-1}) + e^-_{photo},$$

Step 2 (ICD):

$$H_2O\cdots NH_3^+(2s^{-1}) \longrightarrow H_2O^+(2p^{-1})\cdots NH_3^+(2p^{-1}) + e^-_{ICD}.$$

Although some of the decay channels here bring up e^-_{ICD} with energies of about 10 eV as shown in Tables 4.9 and 4.6, the main part of electrons accompanying the ICD is below 7 eV.

4.2.4 $NH_3\cdots H_2O$

The water and ammonia molecules can also bind such that NH_3 is the proton donor and H_2O the proton acceptor, see Fig. 2. In this case, removing an electron form the inner-valence nitrogen $2s$-type MO will again lead to ICD. However, the inner-valence ionization of the water subunit gives rise not only to ICD, but also to ETMD. The autoionization

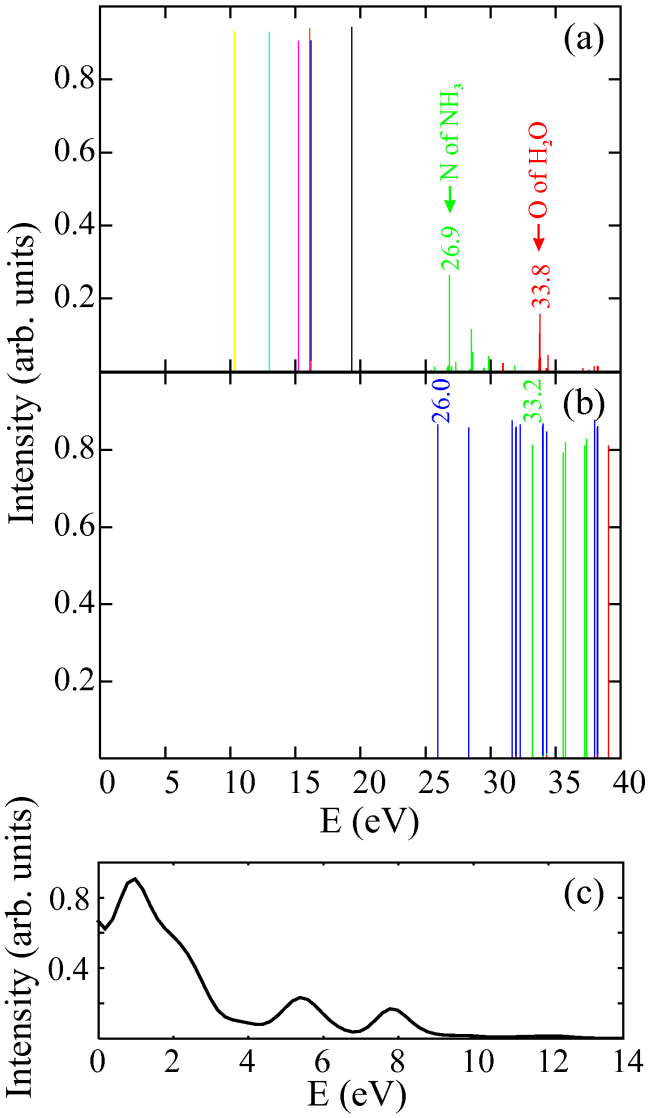

Figure 4.16: Panels (a) and (b): Computed single- and double-ionization spectra of $NH_3 \cdots H_2O$ in its ground state equilibrium geometry, respectively. Panel (c): The spectrum of the ICD electron. The colors in panel (a) indicate the different atoms on which the inner-valence hole is mainly localized, while the colors in panel (b) indicate the different types of the dicationic states: the two-site states, $NH_3^+ \cdots H_2O^+$, are depicted in blue, the one-site states of the type $NH_3^{++} \cdots H_2O$ are depicted in green, and the one-site states of the type $NH_3 \cdots H_2O^{++}$, are depicted in red.

channels are closed in all cases, i.e. inner-valence ionized states of $NH_3 \cdots H_2O$ can decay only by intermolecular mechanisms. In short:

Step 1 (inner-valence ionization):

$$NH_3 \cdots H_2O \xrightarrow{h\nu} NH_3^+(2s^{-1}) \cdots H_2O + e^-_{photo},$$

Step 2 (ICD):

$$NH_3^+(2s^{-1}) \cdots H_2O \longrightarrow NH_3^+ \cdots H_2O^+ + e^-_{ICD},$$

Step 1 (inner-valence ionization):

$$NH_3 \cdots H_2O \xrightarrow{h\nu} NH_3 \cdots H_2O^+(2s^{-1}) + e^-_{photo},$$

Table 4.10: Calculated values of the single ionization potentials of the outer-valence shell of $NH_3\cdots H_2O$, their energies and intensities, as well as the contribution of the $(MOs)^{-1}$ configuration to each of the ionic states. For further details about the computational method see Section 2.2.4 and the references therein.

$NH_3\cdots H_2O$ in symmetry C_s			
Energy [eV]	Intensity	Contribution of the $(MOs)^{-1}$ to the ionic state	
		MOs	Coefficients[a]
10.3142	0.933	$8a^{'}$	-0.97
12.9780	0.932	$7a^{'}$	0.96
15.2198	0.934	$6a^{'}$	-0.95
		$5a^{'}$	-0.17
16.0965	0.940	$2a^{''}$	-0.97
16.2034	0.936	$5a^{'}$	-0.95
		$6a^{'}$	0.17
19.3299	0.944	$1a^{''}$	0.97

[a]Coefficients of the ACD(3) eigenvectors with values above 0.05 are given.

Step 2 (ICD):

$$NH_3\cdots H_2O^+(2s^{-1}) \longrightarrow NH_3^+\cdots H_2O^+ + e^-_{ICD}, or$$

Step 2 ((ETMD), a low intensity process):

$$NH_3\cdots H_2O^+(2s^{-1}) \longrightarrow NH_3^{++}\cdots H_2O + e^-_{ETMD}.$$

The electron spectra of the singly and doubly ionized $NH_3\cdots H_2O$, as well as the spectrum of the e^-_{ICD} accompanying the ICD are depicted in Fig. 4.16, while additional information for the system is given in Tables 4.10 and 4.6.

4.2.5 $H_2O\cdots H_2S$ and $H_2S\cdots H_2O$

The water-hydrogensulfide complex is characterized by a very week hydrogen bond. In the case of H_2O being the proton donor it is more than 2.5 Å long, while in the case of H_2O being the proton acceptor it is about 2.1 Å. In both species the bond is significantly longer than that in the other systems studied (see Fig. 4.10). As a consequence of the large distance between the constituents, the two-site double-ionization threshold is lower due to the reduced Coulomb repulsion energy between the H_2O^+ and H_2S^+ ions. Nevertheless, since the inner-valence shell of H_2S is a $3s$ type MO, the resulting respective ionic states

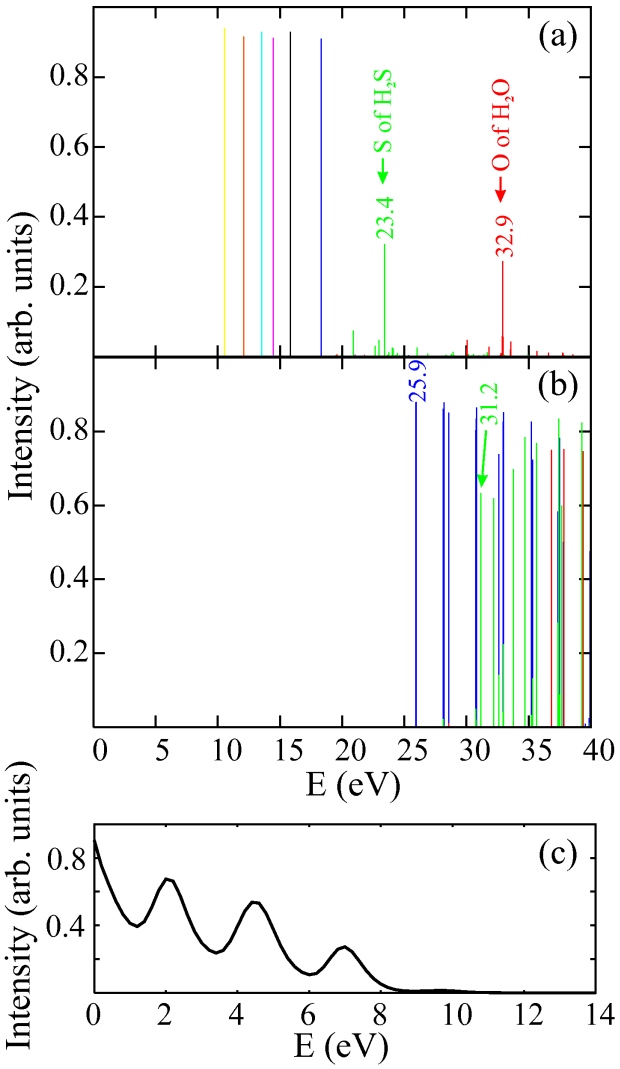

Figure 4.17: Panels (a) and (b): Computed single- and double-ionization spectra of $H_2O \cdots H_2S$ in its ground state equilibrium geometry, respectively. Panel (c): The spectrum of the ICD electron. The colors in panel (a) indicate the different atoms on which the inner-valence hole is mainly localized, while the colors in panel (b) indicate the different types of the dicationic states: the two-site states, $H_2O^+ \cdots H_2S^+$, are depicted in blue, the one-site states of the type $H_2O \cdots H_2S^{++}$ are depicted in green, and the one-site states of the type $H_2O^{++} \cdots H_2S$, are depicted in red.

lie relatively low in energy, the ICD from $H_2S^+(3s^{-1})$ is energetically forbidden, as shown in Figs. 4.17 and 4.18 and Tables 4.11 and 4.12. The inner-valence ionized water, however, can decay both by ICD and ETMD to $H_2O^+ \cdots H_2S^+$ and $H_2O \cdots H_2S^{++}$, respectively.

Thus, the relaxation modes of the inner-valence ionized states of the $H_2O \cdots H_2S$ cluster can be written as:

Step 1 (inner-valence ionization):

$$H_2O \cdots H_2S \xrightarrow{h\nu} H_2O^+(2s^{-1}) \cdots H_2S + e^-_{photo},$$

Step 2 (ICD):

$$H_2O^+(2s^{-1}) \cdots H_2S \longrightarrow H_2O^+(2p^{-1}) \cdots H_2S^+(3p^{-1}) + e^-_{ICD}, or$$

Table 4.11: Calculated values of the single ionization potentials of the outer-valence shell of $H_2O\cdots H_2S$, their energies and intensities, as well as the contribution of the $(MOs)^{-1}$ configuration to each of the ionic states. For further details about the computational method see Section 2.2.4 and the references therein.

$H_2O\cdots H_2S$ in symmetry C_s			
Energy [eV]	Intensity	Contribution of the $(MOs)^{-1}$ to the ionic state	
		MOs	Coefficients[a]
10.5516	0.941	$11a^{'}$	-0.97
12.0951	0.916	$3a^{''}$	0.96
13.5302	0.933	$10a^{'}$	0.96
		$9a^{'}$	0.06
14.4808	0.917	$9a^{'}$	-0.96
		$10a^{'}$	0.06
15.8558	0.929	$2a^{''}$	0.96
18.3367	0.910	$8a^{'}$	0.95

[a]Coefficients of the ACD(3) eigenvectors with values above 0.05 are given.

Table 4.12: Calculated values of the single ionization potentials of the outer-valence shell of $H_2S\cdots H_2O$, their energies and intensities, as well as the contribution of the $(MOs)^{-1}$ configuration to each of the ionic states. For further details about the computational method see Section 2.2.4 and the references therein.

$H_2S\cdots H_2O$ in symmetry C_s			
Energy [eV]	Intensity	Contribution of the $(MOs)^{-1}$ to the ionic state	
		MOs	Coefficients[a]
9.5670	0.941	$2a^{''}$	0.97
12.3485	0.932	$11a^{'}$	0.95
		$10a^{'}$	0.18
13.1514	0.927	$10a^{'}$	0.93
		$11a^{'}$	-0.19
		$9a^{'}$	-0.13
14.6626	0.928	$9a^{'}$	0.95
		$10a^{'}$	0.13
		$8a^{'}$	-0.12
15.8189	0.924	$8a^{'}$	0.95
		$9a^{'}$	0.11
19.4571	0.937	$1a^{''}$	0.97

[a]Coefficients of the ACD(3) eigenvectors with values above 0.05 are given.

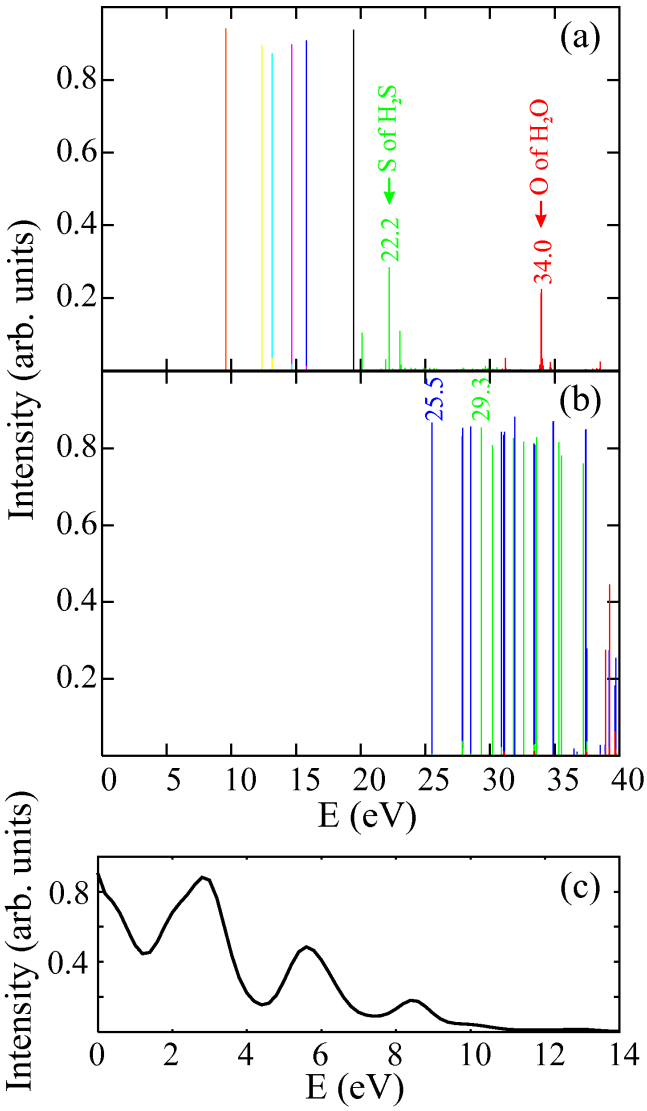

Figure 4.18: Panels (a) and (b): Computed single- and double-ionization spectra of $H_2S \cdots H_2O$ in its ground state equilibrium geometry, respectively. Panel (c): The spectrum of the ICD electron. The colors in panel (a) indicate the different atoms on which the inner-valence hole is mainly localized, while the colors in panel (b) indicate the different types of the dicationic states: the two-site states, $H_2S^+ \cdots H_2O^+$, are depicted in blue, the one-site states of the type $H_2S^{++} \cdots H_2O$ are depicted in green, and the one-site states of the type $H_2S \cdots H_2O^{++}$, are depicted in red.

Step 2 ((ETMD), a low intensity process):

$$H_2O^+(2s^{-1}) \cdots H_2S \longrightarrow H_2O \cdots H_2S^{++}(3p^{-2}) + e^-_{ETMD}.$$

The emitted ICD electron will be in the energy range from 0 to 9 eV, see Fig. 4.17(c). There, four maxima which can be attributed to the decay of the main line of $O3s^{-1}$ state to the four groups of two site states below it. Looking at the distance between the centers of mass of H_2O and H_2S in their ground state, a maximum value of 4.1 eV for KER can be expected.

The intermolecular electronic decay modes in the case of $H_2S \cdots H_2O$ can be written in short as:

Step 1 (inner-valence ionization):

$$H_2S\cdots H_2O \xrightarrow{h\nu} H_2S\cdots H_2O^+(2s^{-1}) + e^-_{photo},$$

Step 2 (ICD):

$$H_2S\cdots H_2O^+(2s^{-1}) \longrightarrow H_2S^+(3p^{-1})\cdots H_2O^+(2p^{-1}) + e^-_{ICD}, or$$

Step 2 ((ETMD), a low intensity process):

$$H_2S\cdots H_2O^+(2s^{-1}) \longrightarrow H_2S^{++}(3p^{-2})\cdots H_2O + e^-_{ETMD}.$$

Here, the e^-_{ICD} spectrum has a very similar shape and a slight spread to higher energy in comparison to $H_2O\cdots H_2S$, see Fig. 4.18(c). This comes as a result of the similarities in the spectra of $H_2O\cdots H_2S$ and $H_2S\cdots H_2O$ where the main line of the $O2s^{-1}$ state has the major contribution to the decay spectra. The maximum KER also has a very close value to the one of the other system containing water and hydrogensulphide, due to the very similar distances between the O and S atoms in the ground state structures, as shown in Table 4.6.

Finally, we briefly comment on the implications of the studied processes in more complex systems. As mentioned already, the electronic decay processes that take place in the small hydrogen bonded systems studied will be operative in large biological macromolecules in aqueous environment, as well. The inner-valence ionization of a water molecule bonded to a macromolecule will always lead to ICD (see Fig. 4.12) as the most efficient relaxation pathway. In the case of inner-valence ionization of the macromolecule participating in the hydrogen bond, the ICD will also be operative (except if the electronic state is low in energy like in H_2S), but depending on the covalent structure of this subunit it may have to compete with a possibly more efficient autoionization. π-bonded structures typically posses low first single and double IPs and relatively high single inner-valence IPs. Our results show (see Table 4.6) that autoionization will be most likely energetically open for such systems. For all other types of covalent bonding the autoionization channel will be most likely closed and thus the ICD will be the only possible mechanism of electronic decay.

4.3 Conclusions

Ultrafast intermolecular decay processes in water containing hydrogen bonded systems, where the H_2O molecule is a p-donor or a p-acceptor, have been investigated. In particular, the most efficient relaxation modes of the inner-valence ionized $H_2O\cdots HCHO$, $H_2O\cdots H_2CNH$, $H_2O\cdots NH_3$, $NH_3\cdots H_2O$, $H_2O\cdots H_2S$, $H_2S\cdots H_2O$ and $H_2O\cdots H_2O$ (p-donor$\cdots$ p-acceptor) have been established. The selected systems represent seven types of hydrogen bonding that are the most commonly formed between water and macromolecules in biochemistry. In addition to the identification of the processes, the energies of the emitted secondary electrons and of the kinetic energy released by the created ions have been estimated, see Table 4.6.

The ultrafast intermolecular Coulombic decay and related decay mechanisms of the singly and doubly ionized water dimer were studied using model potential energy curves, as well. Direct comparison with available experimental data for the ICD in singly ionized water dimers showed that a simplified description in which the internal degrees of freedom are neglected gives surprisingly useful results. The recent experiment on ICD in water dimer [14] suggested that the ICD process initiated by an inner-valence ionization is so fast that the produced two-site dication breaks up by a Coulomb explosion in two, intact water cations. That is why, the description of such kind of ultrafast decay processes with the help of PECs that represent cuts of the $(H_2O)_2$ hypersurface along the minimal in energy O-O pathway of the ground state is meaningful.

Optimizing the geometry of $(H_2O)_2$ at R_{O-O} from 2.10 to 6.00 Å we have determined the shallow minimum of the ground state PEC at 2.91 Å. This equilibrium distance is of great importance for the description of the ICD processes, as it determines the amount of energy which the two subunits will divide among their KER, rotational, and vibrational degrees of freedom in the course of the Coulomb explosion that follows the ICD. It also determines the energy of the emitted ICD-electron. To obtain the KER we constructed the PECs for the initial $H_2O^+(2s^{-1})H_2O$ and the final $H_2O^+H_2O^+$ states using the ground-state optimized structures of the dimer.

The single- and double-ionization spectra of the water dimer computed at its ground-state optimized structures showed that the ICD of the $2s^{-1}$ states of the dimer is open at all intermolecular separations studied, namely at O-O distances from 2.10 to 6.00 Å, irrespective of whether the initially ionized water molecule is the proton donor or the proton acceptor one. However, the PECs for the $2s^{-1}$ states of the proton donor and the proton acceptor show very different behavior. The PEC of the proton donnor is a bound state type curve with a minimum of about 1.27 eV at $R_{O-O} \sim 2.7$ Å, while the PEC

of the proton acceptor is a repulsive curve that decreases by more than 1 eV from 2.10 to 6.00 Å. Thus, in principle, characteristic electron spectra for the two water molecules could be made and their properties may be differentiated. However, our results show that the KER of the two water cations flying back-to-back after the ICD process is the same, namely around 4.8 eV. Very recently we have shown that the discrepancy of 0.6 eV compared to the experimental result of 4.2 eV is due to the energy that is taken by the rotation of the proton-donor water molecule in the course of the Coulomb explosion [103], a degree of freedom that is not taken into account in the present calculations.

Our computations allow us also to make an estimate for the emitted ICD-electron. Taking into account all possible ICD channels initiated by a $2s^{-1}$ state, our estimation for the electron spectrum is that the majority of ICD-electrons have kinetic energy in the range of 0-4 eV peaking at the low-energy limit while the less populated decaying states will lead to a tail reaching to higher energies, as already shown in Ref. [11]. Another important observation is that an ETMD process from the most populated $2s^{-1}$ state is energetically forbidden at all intermolecular distances studied, irrespective of whether the initial ionization is on the proton-donor or the proton-acceptor molecule. Higher lying satellites weakly populated by photoionization can, however, undergo ETMD, but the decay probability is much lower than that of ICD.

The ab initio computed PECs of the final two-site dicationic states of the ICD showed that they are very close to asymptotically adjusted $1/R$ potentials. They differ from them only at O-O distances smaller than that of the ground state equilibrium. This, together with the ultrashort time scale of the ICD process, suggest that a qualitative analysis of the ICD and related processes of doubly ionized water dimers can be made with the help of simple model PECs. Due to the weak bonding of the water dimer, the bound one-site dicationic states can be approximated with a horizontal line adjusted to the corresponding molecular state asymptotically, while the repulsive two-site tricationic states (the final states for the ICD process of one-site dicationic dimers) can be represented as a $2/R$ curves asymptotically adjusted to the molecular states of the corresponding fragments. With the help of this simple model we estimated the open decay channels of the one-site doubly ionized water dimer in the energy range between 60 and 90 eV. These are the $H_2O^{++}H_2O$ states of the $2s^{-1}2p^{-1}$ and $2s^{-2}$ type that can be populated via Auger decay of a O1s core-ionized water molecule. Those one-site dicationic states are energetically above four groups of tricationic $H_2O^{++}H_2O^{+}$ states and thus a number of decay channels are open. There are two processes which will dominate here. The $H_2O^{++}(2s^{-1}2p^{-1})H_2O$ will relax via ICD, while $H_2O^{++}(2s^{-2})H_2O$ will undergo $3e^{-}$ ICD, as its energy is above

the triple-ionization threshold of $(H_2O)_2$, but below that of $H_2O^{++}(2s^{-1}2p^{-1})H_2O^{+}(p^{-1})$. In both cases the interatomic electronic decay will be the dominant relaxation mode.

We estimated the energy of the ICD electrons and of the KER following Auger decay in water dimer. The KERs of the dicationic water molecules are expected to have a peak close to 9 eV. Three different approaches to estimate the ICD electron distribution have been considered, one of them using solely the Auger and photoionization spectra of the isolated water molecules. All approaches give qualitatively similar results. The emitted ICD electrons will exhibit a rather long energy distribution peaked at low energy. The constructed ICD-electron spectra (Fig. 4.8(a), (b), and (c)) show that the large majority of the emitted ICD-electrons will have energies between 0 and 8 eV, while more energetic electrons (10 eV or even more) will originate from the decay of the $H_2O^{++}(2a_1^{-2}\ ^1A_1)H_2O$ state. More than 33% of the dications produced by the Auger decay will undergo ICD emitting thereby low-energy ICD electrons! Obviously, the ICD following Auger decay in water is expected to be an additional source of low-energy electrons and, hence, an important mechanism for initiating damages in biosystems. A result that calls for more investigations.

In the course of our study, the geometries of $H_2O\cdots HCHO$, $H_2O\cdots H_2CNH$, $H_2O\cdots NH_3$, $NH_3\cdots H_2O$, $H_2O\cdots H_2S$, and $H_2S\cdots H_2O$ have been optimized using high precision ab initio methods and large basis sets. The resulting structures are characterized by hydrogen bonds in the range from 1.942 Å to 2.515 Å and are used as an input data ADC computations of their single- and double-ionization spectra. To the best of our knowledge, the ionization spectra of the examined clusters, calculated with such a high precision have not been reported in the literature.

Our results demonstrate that ICD will take place in all of the selected species. In particular, the inner-valence ionization of the water molecule in each of the studied systems will be followed by the very fast and efficient ICD. Inner-valence ionization of the H_2O molecule produces decay channels which are open by several eV, therefore this relaxation mode will also be operative in larger systems containing hydrogen bonding types of the investigated set. That is, the eminent presence of water surrounding the biological objects and the relatively high energy of its inner-valence ionized states, guarantees that ICD will take place. The electronic and steric effects typical for macromolecules are not expected to modify this qualitative result. Although the presence of other water molecules of the environment and of that part of the biomolecule which does not participate in the hydrogen bond will change the ionization potentials of the species forming the hydrogen bond, we expect that these changes will be insufficient to close the energy gap between

the initial and final states of the intermolecular decay. Consequently, ICD will take place and LEEs and radical cations will be produced. These products of the ICD process may further create damages of the biomolecule, as shown in Refs. [14, 15, 17, 92–95].

At the end, we would like to comment on the practical importance of the discussed ICD process. Since ICD appears as a primary source of genotoxic particles (LEEs and cationic radicals), it is clear that a detailed knowledge of this fundamental process may help in finding mechanisms to control it. For example, the ICD channel in ammonia clusters can be closed by protonation of the ammonia, as was shown very recently [113]. Importantly, the low-energy ICD electrons and the cationic radicals are produced at the site of the biosystem that participates in the ICD process, i.e., where the incoming photon was absorbed. Hence, the damages will be most probably induced in a close proximity of this site. This feature may also be probably used in practice. By adding a suitable constituent opening the ICD channel one may produce LEE *locally* on the probe that may subsequently damage some undesirable part of the biosystem. In the long run, one may imagine using this feature of the ICD even in medicine.

List of Publications

*(1) X.-J. Liu, N. Saito, H. Fukuzawa, Y. Morishita, S. Stoychev, A. Kuleff, I. H. Suzuki, Y. Tamenori, R. Richter, G. Prmper, and K. Ueda, J. Phys. B **40**, F1 (2007).

*(2) N. Saito, Y. Morishita, I. H. Suzuki, S. D. Stoychev, A. Kuleff, L. S. Cederbaum, X.-J. Liu, H. Fukuzawa, G. Prmper, K. Ueda, Chem. Phys. Lett. **441**, 16 (2007).

*(3) S. D. Stoychev, A. I. Kuleff, F. Tarantelli, and L. S. Cederbaum, J. Chem. Phys. **128**, 014307 (2008).

*(4) S. D. Stoychev, A. I. Kuleff, F. Tarantelli, and L. S. Cederbaum, J. Chem. Phys. **129**, 074307 (2008).

*(5) Ph. V. Demekhin, S. Scheit, S. D. Stoychev, and L. S. Cederbaum, Phys. Rev. A **78**, 043421 (2008).

*(6) K. Kreidi, T. Jahnke, Th. Weber, T. Havermeier, X. Liu, Y. Morisita, S. Schössler, L. Ph. H. Schmidt, M. Schöffler, M. Odenweller, N. Neumann, L. Foucar, J. Titze, B. Ulrich, F. Sturm, C. Stuck, R. Wallauer, S. Voss, I. Lauter, H. K. Kim, M. Rudloff, H. Fukuzawa, G. Prmper, N. Saito, K. Ueda, A. Czasch, O. Jagutzki, H. Schmidt-Böcking, S. Stoychev, Ph. V. Demekhin, and R. Dörner, Phys. Rev. A **78**, 043422 (2008).

*(7) P. V. Demekhin,Y.-C. Chiang, S. D. Stoychev, P. Kolorenč, S. Scheit, A. I. Kuleff, F. Tarantelli, L. S. Cederbaum, J. Chem. Phys. **131**, 104303 (2009).

*(8) O. Vendrell, S. D. Stoychev, L. S. Cederbaum, ChemPhysChem **11**, 1006 (2010).

*(9) V. Averbukh, Ph.V. Demekhin, P. Kolorenč, S. Scheit, S. D. Stoychev, A. I.Kuleff, Y.-C. Chiang, K. Gokhberg, S. Kopelke, N. Sisourat, L. S. Cederbaum, J. Electron Spectrosc. Relat. Phenom. **183**, 36 (2011).

*(10) S. D. Stoychev, A. I. Kuleff, L. S. Cederbaum, J. Chem. Phys. **133**, 154307 (2010).

*(11) S. D. Stoychev, A. I. Kuleff, and L. S. Cederbaum, J. Am. Chem. Soc., **133**, 6817 (2011).

(12) K. Sakai, S. Stoychev, T. Ouchi, I. Higuchi, M. Schöffler, T. Mazza, H. Fukuzawa, K. Nagaya, M. Yao, Y. Tamenori, A. I. Kuleff, N. Saito, and K. Ueda, Phys. Rev. Lett. **106**, 033401 (2011).

*Containing results presented in the current work.

(13) T. Ouchi, K. Sakai, H. Fukuzawa, I. Higuchi, Ph. V. Demekhin, Y.-C. Chiang, S. D. Stoychev, A. I. Kuleff, T. Mazza, M. Schöffler, K. Nagaya, M. Yao, Y. Tamenori, N. Saito, and K. Ueda1, Phys. Rev. A (2011) Article in Press (available online).

Bibliography

[1] D. A. Shirley, R. L. Martin, S. P. Kowalczyk, F. R. McFeely, and L. Ley, Phys. Rev. B **15**, 544 (1977).

[2] H.Koerber and W. Mehlhorn, Phys. Lett. **13**, 129 (1964).

[3] Y. Ralchenko, F.-C. Jou, D. E. Kelleher, A. E. Kramida, A. Musgrove, J. Reader, W. L. Wiese, and K. Olsen, NIST Atomic Spectra Database (version 3.1.1) (2007) [Online]. **Available: http://physics.nist.gov/asd3**, National Institute of Standards and Technology, Gaithersburg, MD. (2006 - 2007).

[4] M. Thompson, M. D. Baker, A. Christie, and J. F. Tyson, Auger Electron Spectroscopy (Wiley, New York, 1985).

[5] C. D. Wagner and A. Joshi, J. Electron Spectrosc. Relat. Phenom. **47**, 283 (1988).

[6] M. O. Krause, J. Phys. Chem. Ref. Data **8**, 307 (1979).

[7] L. S. Cederbaum, J. Zobeley, and F. Tarantelli, Phys. Rev. Lett. **79**, 4778 (1997).

[8] R. Santra, L. S. Cederbaum, and H.-D. Meyer, Chem. Phys. Lett. **303**, 413 (1999).

[9] R. Santra, J. Zobeley, and L. S. Cederbaum, Phys. Rev. B **64**, 245104 (2001).

[10] R. Santra, J. Zobeley, L. S. Cederbaum, and F. Tarantelli, J. Electron Spectrosc. Relat. Phenom. **114-116**, 41 (2001).

[11] I. B. Müller and L. S. Cederbaum, J. Chem. Phys. **125**, 204305 (2006).

[12] V. Averbukh and L. S. Cederbaum, Phys. Rev. Lett. **96**, 053401 (2006).

[13] I. B. Müller and L. S. Cederbaum, J. Phys. Chem. A **109**, 10424 (2005).

[14] T. Jahnke, H. Sann, T. Havermeier, K. Kreidi, C. Stuck, M. Meckel, M. Schöffler, N. Neumann, R. Wallauer, S. Voss, A. Czasch, O. Jagutzki, A. Malakzadeh, F. Afaneh, T. Weber, H. Schmidt-Bocking, and R. Dorner, Nature Phys. **6**, 139 (2010).

[15] M. Mucke, M. Braune, S. Barth, M. Forstel, T. Lischke, V. Ulrich, T. Arion, U. Becker, A. Bradshaw, and U. Hergenhahn, Nature Phys. **6**, 143 (2010).

[16] A. I. Kuleff and L. S. Cederbaum, Phys. Rev. Lett. **98**, 083201 (2007).

[17] I. B. Müller and L. S. Cederbaum, J. Chem. Phys. **122**, 094305 (2005).

[18] K. Gokhberg, V. Averbukh, and L. S. Cederbaum, J. Chem. Phys. **124**, 144315 (2006).

[19] K. Gokhberg, A. B. Trofimov, T. Sommerfeld, and L. S. Cederbaum, Europhys. Lett. **72**, 228 (2005).

[20] R. Santra and L. S. Cederbaum, Phys. Rev. Lett. **90**, 153401 (2003).

[21] Y. Morishita, X.-J. Liu, N. Saito, T. Lischke, M. Kato, G. Prümper, M. Oura, H. Yamaoka, Y. Tamenori, I. H. Suzuki, and K. Ueda, Phys. Rev. Lett. **96**, 243402 (2006).

[22] X.-J. Liu, N. Saito, H. Fukuzawa, Y. Morishita, S. Stoychev, A. Kuleff, I. H. Suzuki, Y. Tamenori, R. Richter, G. Prümper, and K. Ueda, J. Phys. B **40**, F1 (2007).

[23] Y. Morishita, N. Saito, I. H. Suzuki, H. Fukuzawa, X.-J. Liu, K. Sakai, G. Prümper, K. Ueda, H. Iwayama, K. Nagaya, M. Yao, K. Kreidi, M. Schöffler, T. Jahnke, S. Schössler, R. Dörner, T. Weber, J. Harries, and Y. Tamenori, J. Phys. B **41**, 025101 (2008).

[24] K. Kreidi, T. Jahnke, T. Weber, T. Havermeier, R. E. Grisenti, X. Liu, Y. Morisita, S. Schössler, L. P. H. Schmidt, M. Schöffler, M. Odenweller, N. Neumann, L. Foucar, J. Titze, B. Ulrich, F. Sturm, C. Stuck, R. Wallauer, S. Voss, I. Lauter, H. K. Kim, M. Rudloff, H. Fukuzawa, G. Prümper, N. Saito, K. Ueda, A. Czasch, O. Jagutzki, H. Schmidt-Böcking, S. K. Semenov, N. A. Cherepkov, and R. Dörner, J. Phys. B **41**, 101002 (2008).

[25] J. Zobeley, R. Santra, and L. S. Cederbaum, J. Chem. Phys. **115**, 5076 (2001).

[26] V. Averbukh, I. B. Müller, and L. S. Cederbaum, Phys. Rev. Lett. **93**, 263002 (2004).

[27] T. Jahnke, A. Czasch, M. Schöffler, S. Schössler, M. Käsz, J. Titze, K. Kreidi, R. E. Grisenti, A. Staudte, O. Jagutzki, L. P. H. Schmidt, T. Weber, H. Schmidt-Böcking, K. Ueda, and R. Dörner, Phys. Rev. Lett. **99**, 153401 (2007).

[28] S. Marburger, O. Kugeler, U. Hergenhahn, and T. Möller, Phys. Rev. Lett. **90**, 203401 (2003).

[29] T. Jahnke, A. Czasch, M. S. Schöffler, S. Schössler, A. Knapp, M. Käsz, J. Titze, C. Wimmer, K. Kreidi, R. E. Grisenti, A. Staudte, O. Jagutzki, U. Hergenhahn, H. Schmidt-Böcking, and R. Dörner, Phys. Rev. Lett. **93**, 163401 (2004).

[30] G. Öhrwall, M. Tchaplyguine, M. Lundwall, R. Feifel, H. Bergersen, T. Rander, A. Lindblad, J. Schulz, S. Peredkov, S. Barth, S. Marburger, U. Hergenhahn, S. Svensson, and O. Björneholm, Phys. Rev. Lett. **93**, 173401 (2004).

[31] T. Aoto, K. Ito, Y. Hikosaka, E. Shigemasa, F. Penent, and P. Lablanquie, Phys. Rev. Lett. **97**, 243401 (2006).

[32] A. Szabo and N. S. Ostlund, Modern Quantum Chemistry (Dover publications, INC., Mineola, New York, 1996).

[33] L. S. Cederbaum, in Encyclopedia of Computational Chemistry, edited by P. von R. Schleyer, P. R. Schreiner, N. L. Allinger, T. Clark, J. Gasteiger, P. Kollman, and H. F. S. III (Wiley, New York, 1998).

[34] J. Schirmer and A. Barth, Z. Phys. A **317**, 267 (1984).

[35] A. Tarantelli and L. S. Cederbaum, Phys. Rev. A **46**, 81 (1992).

[36] L. S. Cederbaum and W. Domcke, Adv. Chem. Phys. **36**, 205 (1977).

[37] J. Schirmer, L. S. Cederbaum, and O. Walter, Phys. Rev. A **28**, 1237 (1983).

[38] J. Schirmer, A. B. Trofimov, and G. Stelter, J. Chem. Phys. **109**, 4734 (1998).

[39] J. J. Sakurai, Modern Quantum Mechanics (Addison-Wesley, Reading, MA, 1994).

[40] R. Santra and L. S. Cederbaum, J. Chem. Phys. **115**, 6853 (2001).

[41] R. Santra and L. S. Cederbaum, J. Chem. Phys. **117**, 5511 (2002).

[42] V. Averbukh and L. S. Cederbaum, J. Chem. Phys. **123**, 204107 (2005).

[43] Kolorenč, V. Averbukh, K. Gokhberg, and L. S. Cederbaum, J. Chem. Phys. **129**, 244102 (2008).

[44] All basis sets used in this work were obtained from the Extensible Computational Chemistry Environment Basis Set Database, as developed and distributed by the Molecular Science Computing Facility, Environmental and Molecular Sciences Laboratory which is part of the Pacific Northwest Laboratory, P.O. Box 999, Richland, Washington 99352, USA, and funded by the U.S. Department of Energy. The Pacific Northwest Laboratory is a multi-program laboratory operated by Battelle Memorial Institute for the U.S. Department of Energy under contract DE-AC06-76RLO 1830. Contact Karen Schuchardt for further information, see http://www.emsl.pnl.gov/forms/basisform.html.

[45] MOLPRO, version 2006.1, a package of ab initio programs, H.-J. Werner, P. J. Knowles, R. Lindh, F. R. Manby, M. Schütz, P. Celani, T. Korona, G. Rauhut, R. D. Amos, A. Bernhardsson, A. Berning, D. L. Cooper, M. J. O. Deegan, A. J. Dobbyn, F. Eckert, C. Hampel and G. Hetzer, A. W. Lloyd, S. J. McNicholas, W. Meyer and M. E. Mura, A. Nicklass, P. Palmieri, R. Pitzer, U. Schumann, H. Stoll, A. J. Stone, R. Tarroni and T. Thorsteinsson, see http://www.molpro.net.

[46] A. Tarantelli and L. S. Cederbaum, Phys. Rev. A **39**, 1639 (1989).

[47] A. Tarantelli and L. S. Cederbaum, Phys. Rev. A **39**, 1656 (1989).

[48] J. Schirmer, Phys. Rev. A **43**, 4647 (1991).

[49] G. Angonoa, O. Walter, and J. Schirmer, J. Chem. Phys. **87**, 6789 (1987).

[50] F. Tarantelli, Chem. Phys. **329**, 11 (2006).

[51] L. J. Saethre, T. D. Thomas, and L. Ungier, J. Electron Spectrosc. Relat. Phenom. **33**, 381 (1984).

[52] J. Zobeley, L. S. Cederbaum, and F. Tarantelli, J. Phys. Chem. A **103**, 11145 (1999).

[53] H.-J. Werner, Mol. Phys. **89**, 645 (1996).

[54] B. Winter, R. Weber, W. Widdra, M. Dittmar, M. Faubel, and I. V. Hertel, J. Phys. Chem. A **108**, 2625 (2004).

[55] H. Siegbahn, L. Asplund, and P. Kelfve, Chem. Phys. Lett. **35**, 330 (1975).

[56] H. Ågren, S. Svensson, and U. I. Wahlgren, Chem. Phys. Lett. **35**, 336 (1975).

[57] V. Carravetta and H. Ågren, Phys. Rev. A **35**, 1022 (1987).

[58] F. Tarantelli, A. Tarantelli, A. Sgamellotti, J. Schirmer, and L. S. Cederbaum, J. Chem. Phys. **83**, 4683 (1985).

[59] A. Inoyatov, D. V. Filosofov, V. M. Gorozhankin, A. Kovalík, N. A. Lebedev, A. V. Lubashevskiy, A. F. Novgorodov, L. L. Perevoshchikov, T. Vylov, and E. A. Yakushev, J. Electron Spectrosc. Relat. Phenom. **154**, 79 (2007).

[60] S. Scheit, V. Averbukh, H.-D. Meyer, N. Moiseyev, R. Santra, T. Sommerfeld, J. Zobeley, and L. S. Cederbaum, J. Chem. Phys. **121**, 8393 (2004).

[61] T. van Mourik, A. K. Wilson, and T. H. D. Jr, Mol. Phys. **96**, 529 (1999).

[62] S. M. Cybulski and R. R. Toczylowski, J. Chem. Phys. **111**, 10520 (1999).

[63] R. A. Aziz, W. J. Meath, and A. R. Allnatt, Chem. Phys. **78**, 295 (1983).

[64] A. Wüest and F. Merkt, J. Chem. Phys. **118**, 8807 (2003).

[65] P. V. Demekhin, S. Scheit, S. D. Stoychev, and L. S. Cederbaum, Phys. Rev. A **78**, 043421 (2008).

[66] K. Kreidi, T. Jahnke, T. Weber, T. Havermeier, X. Liu, Y. Morisita, S. Schössler, L. P. H. Schmidt, M. Schöffler, M. Odenweller, N. Neumann, L. Foucar, J. Titze, B. Ulrich, F. Sturm, C. Stuck, R.Wallauer, S. Voss, I. Lauter, H. K. Kim, M. Rudloff, H. Fukuzawa, G. Prümper, N. Saito, K. Ueda, A. Czasch, O. Jagutzki, H. Schmidt-Böcking, S. Stoychev, P. V. Demekhin, and R. Dörner, Phys. Rev. A **78**, 043422 (2008).

[67] N. Saito, Y. Morishita, I. H. Suzuki, S. D. Stoychev, A. I. Kuleff, L. S. Cederbaum, X.-J. Liu, H. Fukuzawa, G. Prümper, and K. Ueda, Chem. Phys. Lett. **441**, 16 (2007).

[68] S. D. Stoychev, A. I. Kuleff, F. Tarantelli, and L. S. Cederbaum, J. Chem. Phys. **128**, 014307 (2008).

[69] J. Viefhaus, A. N. Grum-Grzhimailo, N. M. Kabachnik, and U. Becker, J. Electron Spectrosc. Relat. Phenom. **141**, 121 (2004).

[70] T. A. Carlson and M. O. Krause, Phys. Rev. Lett. **11**, 390 (1965).

[71] T. van Mourik, A. K. Wilson, , and T. H. D. Jr, Mol. Phys. **96**, 529 (1999).

[72] P. Slavíček, R. Kalus, P. Paška, I. Odvárková, P. Hobza, and A. Malijevský, J. Chem. Phys. **119**, 2102 (2003).

[73] S. M. Cybulski and R. R. Toczyłowski, J. Chem. Phys. **111**, 10520 (1999).

[74] N. Kurita and H. Sekino, Int. J. Quantum Chem. **91**, 355 (2003).

[75] R. A. Aziz, J. Chem. Phys. **99**, 4518 (1993).

[76] P. R. Herman, P. E. LaRocque, and B. P. Stoicheff, J. Chem. Phys. **89**, 4535 (1988).

[77] M. O. Krause, J. Phys. Chem. Ref. Data **8**, 307 (1979).

[78] K. Ueda, X.-J. Liu, G. Prümper, H. Fukuzawa, Y. Morishita, and N. Saito, J. Electron Spectrosc. Relat. Phenom. **115**, 113 (2007).

[79] F. Combet-Farnoux, P. Lablanquie, J. Mazeau, and A. Huetz, J. Phys. B **33**, 1597 (2000).

[80] G. Herzberg, in Molecular spectra and molecular structure. I. Spectra of Diatomic Molecules (Van Nostrand Reinhold, New York, 1950).

[81] C. Cachoncinlle, J. M. Pouvesle, G. Durant, and F. Spiegelmann, J. Chem. Phys. **96**, 6085 (1992).

[82] A. V. Zaitsevskii and A. I. Dement'ev, Optics Commun. **86**, 461 (1991).

[83] M. Daskalopoulou and S. D. Peyerimhoff, Mol. Phys. **79**, 985 (1993).

[84] E. J. McGuire, Phys. Rev. A **11**, 1880 (1975).

[85] H. Langhoff, Optics Commun. **68**, 31 (1988).

[86] M. Gisselbrecht, A. Lindgren, M. Tchaplyguine, F. Burmeister, G. Öhrwall, M. Lundwall, M. Lundin, R. R. T. Marinho, A. N. de Brito, S. Svensson, O. Björneholm, and S. L. Sorensen, J. Chem. Phys. **123**, 194301 (2005).

[87] L. Poisson, K. D. Raffael, M.-A. Gaveau, B. Soep, J.-M. Mestdagh, J. Caillat, R. Taïeb, and A. Maquet, Phys. Rev. Lett. **99**, 103401 (2007).

[88] L. S. Cederbaum, W. Domcke, J. Schirmer, and W. von Niessen, Adv. Chem. Phys. **65**, 115 (1986).

[89] K. Ueda, Private communication (unpublished).

[90] P. V. Demekhin, Y.-C. Chiang, S. D. Stoychev, P. Kolorenč, S. Scheit, A. I. Kuleff, F. Tarantelli, and L. S. Cederbaum, J. Chem. Phys. **131**, 104303 (2009).

[91] K. Ueda, H. Fukuzawa, X.-J. Liu, K. Sakai, G. Prmper, Y. Morishita, N. Saito, I. Suzuki, K. Nagaya, H. Iwayama, M. Yao, K. Kreidi, M. Schffler, T. Jahnke, S. Schssler, R. Drner, T. Weber, J. Harries, and Y. Tamenori, J. Electron Spectrosc. Relat. Phenom. **166**, 3 (2008).

[92] P. O'Neill, D. L. Stevens, and E. F. Garman, J. Synchrotron Radiat. **9**, 329 (2002).

[93] S. Purkayastha, J. R. Milligan, and W. A. Bernhard, J. Phys. Chem. B **109**, 16967 (2005).

[94] B. Boudaïffa, P. Cloutier, D. Hunting, M. A. Huels, and L. Sanche, Science **287**, 1658 (2000).

[95] F. Martin, P. D. Burrow, Z. Cai, P. Cloutier, D. Hunting, and L. Sanche, Phys. Rev. Lett. **93**, 068101 (2004).

[96] D. L. Nelson and M. M. Cox, Lehninger Principles of Biochemistry (W. H. Freeman, ADDRESS, 2004).

[97] S. J. Grabowski, Hydrogen Bonding – New Insights (Springer, Berlin, 2006).

[98] G. A. Jeffrey, An Introduction to Hydrogen Bonding (Oxford University Press, New York, 1997).

[99] N. Goldman, C. Leforestier, and R. J. Saykally, J. Phys. Chem. A **108**, 787 (2004).

[100] D. Feller, J. Chem. Phys. **96**, 6104 (1992).

[101] J. G. C. M. van Duijneveldt-van de Rijdt and F. B. van Duijneveldt, J. Chem. Phys. **97**, 5019 (1992).

[102] K. Kim and K. D. Jordan, J. Phys. Chem. **98**, 10089 (1994).

[103] O. Vendrell, S. D. Stoychev, and L. S. Cederbaum, Chem. Phys. Chem. **11**, 1006 (2010).

[104] L. S. Cederbaum, W. Domcke, J. Schirmer, and W. von Niessen, Adv. Chem. Phys. **65**, 115 (1986).

[105] R. Cambi, G. Ciullo, A. Sgamellotti, C. E. Brion, J. P. D. Cook, I. E. McCarthy, and E. Weigold, Chem. Phys. **91**, 373 (1984).

[106] L. S. Cederbaum, G. Hohlneicher, and W. V. Niessen, Mol. Phys. **26**, 1405 (1973).

[107] A. B. Trofimov, G. Stelter, and J. Schirmer, J. Chem. Phys. **117**, 6402 (2002).

[108] S. D. Stoychev, A. I. Kuleff, F. Tarantelli, and L. S. Cederbaum, J. Chem. Phys. **129**, 074307 (2008).

[109] S. D. Stoychev, A. I. Kuleff, and L. S. Cederbaum, J. Am. Chem. Soc. **133**, 6817 (2011).

[110] K. Kim and K. D. Jordan, J. Phys. Chem. **98**, 10089 (1994).

[111] S. D. Stoychev, A. I. Kuleff, and L. S. Cederbaum, J. Chem. Phys. **133**, 154307 (2010).

[112] N. Sisourat, N. V. Kryzhevoi, P. Kolorenč, S. Scheit, T. Jahnke, and L. S. Cederbaum, Nature Physics **6**, 508 (2010).

[113] N. V. Kryzhevoi and L. S. Cederbaum, Angew. Chem. Int. Ed. DOI: 10.1002/anie.201004446 (2010).

a) Ich erkläre hiermit an Eides statt, daß ich die vorgelegte Dissertation selbst verfaßt und mich dabei keiner anderen als der von mir ausdrücklich bezeichneten Quellen und Hilfen bedient habe.

b) Ich erkläre hiermit an Eides statt, daß ich an keiner anderen Stelle ein Prüfungsverfahren beantragt beziehungsweise die Dissertation in dieser oder anderer Form bereits anderweitig als Prüfungsarbeit verwendet oder einer anderen Fakultät als Dissertation vorgelegt habe.

Spas Stoychev